

MAR 21 1979

Item 830-H-15

NAS 1.60: 1395

**NASA Technical Paper 1395**

**Measured and Predicted Shock Shapes  
and Aerodynamic Coefficients for  
Blunted Cones at Incidence in  
Helium at Mach 20.3**

**COMPLETED  
ORIGINAL**

**Robert L. Calloway and Nancy H. White**

**MARCH 1979**

**NASA**

(23)

**NASA Technical Paper 1395**

**Measured and Predicted Shock Shapes  
and Aerodynamic Coefficients for  
Blunted Cones at Incidence in  
Helium at Mach 20.3**

**Robert L. Calloway and Nancy H. White**  
*Langley Research Center*  
*Hampton, Virginia*



1979

## SUMMARY

Experimental values of shock shapes ( $\alpha = 0^\circ$  and  $10^\circ$ ) and static aerodynamic coefficients ( $\alpha = -4^\circ$  to  $12^\circ$ ) for cone half-angles of  $30^\circ$ ,  $45^\circ$ ,  $60^\circ$ , and  $70^\circ$  and nose bluntness ratios of 0, 0.25, and 0.50 are presented. Shock shapes were also measured at  $0^\circ$  angle of attack by using a flat-faced cylinder ( $90^\circ$  cone) and a hemispherically blunted cylinder (sphere). All tests were conducted in helium ( $\gamma = 5/3$ ) at a free-stream Mach number of 20.3 and a unit free-stream Reynolds number of  $22.4 \times 10^6$  per meter. Comparisons between measured values and predicted values were made by using several numerical and simple engineering methods.

Most of the numerical methods adequately predicted shock shapes and static aerodynamic coefficients for the cases to which they were applied. In general, the viscous solution of Kumar and Graves (AIAA Paper No. 77-172), which can also be used to calculate the flow field at various angles of attack, provided the best agreement with measured shock shapes where applicable. Barnwell's method (NASA TN D-6283) is inviscid, but it provided excellent agreement with measured shock shapes at various angles of attack on large half-angle blunt-nosed cones where viscous effects are negligible. Measured static aerodynamic coefficients for the  $60^\circ$  and  $70^\circ$  cones showed no effects of nose bluntness ratios, which indicates that entry probes using such geometries may be designed to meet other criteria such as heating or packaging constraints.

## INTRODUCTION

Because of its high drag, efficient heat dissipation, and relatively large volume for payload, the large half-angle spherically blunted cone is an attractive candidate for planetary entry probes. This simple shape served as the aeroshell configuration for the Viking Mars lander and the Venusian probe and will also be utilized for Jovian probes (refs. 1 to 3). Ground-based experimental facilities cannot duplicate planetary entry flight conditions, but they are needed to provide a data base for validation of numerical techniques which can predict these conditions. Also, an experimental data base is needed for inputs to empirical techniques or correlation procedures (ref. 4). A number of experimental studies have been performed for sharp and spherically blunted cones (e.g., refs. 5 to 9), but little data exist for shock shapes and static aerodynamic coefficients for a complete range of entry-type geometries and angles of attack at high Mach numbers. Due to this lack of data, a comprehensive validation of numerical flow-field solutions has not been possible.

The purpose of this report is to present a portion of the results from a study which is designed to establish a hypersonic data base for large half-angle spherically blunted cones over a range of ratios of specific heats and Mach numbers. Also, the intent is to provide comparisons with several existing numerical techniques where possible. Experimental results presented herein are for sharp and spherically blunted cones having cone half-angles of  $30^\circ$ ,  $45^\circ$ ,  $60^\circ$ , and  $70^\circ$ .

and nose bluntness ratios of 0, 0.25, and 0.50. These configurations were tested over a range of angles of attack in the 22-inch aerodynamics leg of the Langley hypersonic helium tunnel facility at a Mach number of 20.3. Measurements include shock shapes at  $\alpha = 0^\circ$  and  $10^\circ$  and static aerodynamic coefficients for  $\alpha = -4^\circ$  to  $12^\circ$  in  $2^\circ$  increments. Shock shapes at  $0^\circ$  angle of attack for a  $90^\circ$  cone and a sphere were obtained by using a flat-faced cylinder model and a hemispherically blunted cylinder model. Comparisons between measured values and predicted values are made by using several numerical and simple engineering methods.

#### SYMBOLS

$C_A$	axial-force coefficient, $\frac{\text{Axial force}}{q_\infty S}$
$C_{A,\text{corr}}$	axial-force coefficient corrected for base pressure, $C_A - \frac{p_\infty - p_b}{q_\infty} \frac{s_b}{s}$
$C_m$	pitching-moment coefficient, $\frac{\text{Pitching moment}}{q_\infty Sd}$
$C_N$	normal-force coefficient, $\frac{\text{Normal force}}{q_\infty S}$
$C_p,\text{max}$	Newtonian pressure coefficient
$d$	model base diameter, cm
$l$	model length, cm
$M_l$	local Mach number
$M_\infty$	free-stream Mach number
$p_b$	base pressure, kPa
$p_t$	stagnation pressure, kPa
$p_\infty$	free-stream static pressure, kPa
$q_\infty$	free-stream dynamic pressure, kPa
$r_b$	model base radius, cm
$r_n$	model nose radius, cm
$r_n/r_b$	nose bluntness ratio
$R_\infty, d$	free-stream Reynolds number based on $d$

$S$	model base area, $\text{cm}^2$
$S_b$	area over which $p_b$ is assumed to act, $\text{cm}^2$
$T_t$	stagnation temperature, K
$V_\infty$	free-stream velocity, m/sec
$x, r$	cylindrical coordinates (fig. 1(a))
$\alpha$	angle of attack, deg
$\gamma$	ratio of specific heats
$\delta^*$	boundary-layer displacement thickness, cm
$\Delta$	distance between model surface and shock wave, measured parallel to model axis, cm (fig. 1(a))
$\theta$	cone half-angle, deg
$\theta_{\text{det}}$	minimum cone half-angle for shock detachment, deg

#### FACILITY AND TEST CONDITIONS

Shock shapes and static aerodynamic coefficients were obtained from flow visualization and force and moment tests conducted in the 22-inch aerodynamics leg of the Langley hypersonic helium tunnel facility. Operation of this facility and details of the flow characteristics are presented in reference 10. Check calibrations using the contoured nozzle have indicated no change in the flow conditions from those reported in reference 10. All tests were conducted at the following flow conditions:

$$M_\infty = 20.3$$

$$P_t = 7000 \text{ kPa}$$

$$T_t = 289 \text{ K}$$

$$R_{\infty, d} = 0.57 \times 10^6 \text{ (cones)}$$

$$R_{\infty, d} = 0.43 \times 10^6 \text{ (cylinders)}$$

#### MODELS

Figure 1(a) provides a general planform view and the dimensions of the 12 cone models tested. These models were constructed from aluminum and have base diameters of approximately 5.08 cm. Cone half-angles of  $30^\circ$ ,  $45^\circ$ ,  $60^\circ$ , and  $70^\circ$  were examined and the nose bluntness ratios (0, 0.25, and 0.50) were varied for each cone half-angle. A flat-faced cylinder and a hemispherically

blunted cylinder, having base diameters of approximately 3.81 cm (fig. 1(b)), were tested to provide shock shapes for a  $90^\circ$  cone and a sphere at  $\alpha = 0^\circ$ . A photograph of the cone models tested is shown in figure 2. The tapered cylindrical section extending behind the model forebody was designed to house the strain-gage balance.

#### TEST METHODS

Quantitative shock-shape measurements in the plane of symmetry for  $\alpha = 0^\circ$  and  $10^\circ$  were obtained by using the electron-beam fluorescence technique described in reference 11. Photographs of the models in the illuminated flow field were taken with a camera positioned with its optical axis normal to the plane of symmetry. The angle of attack was set with a cathetometer before each run. Calculations were made to determine the error introduced by using the conical field-of-view photographs for measuring shock shapes as opposed to a parallel-light, schlieren-type system. For the camera location (fig. 3) and for measurements less than 3.81 cm from the optical axis, this error was no more than 0.3 percent. The shock shapes were read manually from photographs similar to the one shown in figure 4 for  $\theta = 30^\circ$ ,  $r_n/r_b = 0.50$ , and  $\alpha = 10^\circ$ . The error in these measurements is estimated to be 2 percent of  $r_b$ . Since the electron-beam illuminated flow in helium produces pink, purple, and blue colors, enlarged color photographs were used for the measurements to improve the contrast compared with the black and white photograph shown in figure 4. Shock-shape measurements  $\Delta$  were made parallel to the model axis (see fig. 1(a)) and are presented in table I. For values of  $r/r_b$  greater than 1.0,  $\Delta$  was measured from an imaginary extension of the plane defined by the base of the model.

Force and moment tests were performed with the models mounted on a sting-supported, five-component, strain-gage balance (no rolling-moment component). The straight sting was attached to the angle-of-attack mechanism and data were obtained for  $2^\circ$  increments from  $-4^\circ$  to  $12^\circ$ . The angle of attack was set optically by using a point light source adjacent to the test section and a small lens-prism mounted on the rearward extension of the model. The image of the source was reflected by the prism and focused by the lens onto photoelectric cells aligned at calibrated intervals. As the reflected and focused light swept past each cell an electrical relay was energized and caused a high-speed digital recorder to sample and record the outputs of the strain-gage balance onto magnetic tape. The accuracy of the angle of attack is estimated to be  $\pm 0.1^\circ$ . All tests were conducted at a sideslip angle of  $0^\circ$ . Model base pressures were measured at one location (see fig. 3), and the axial-force coefficients are presented both with a base pressure correction  $C_{A,corr}$  and without a base pressure correction  $C_A$ .

The reference area for the models was the base area  $S$  and the reference length was the base diameter  $d$ . All pitching-moment data were reduced about the actual nose of each model. The estimated uncertainties in the measured static aerodynamic coefficients based on  $\pm 0.5$  percent of the balance design loads are as follows:

$$\begin{aligned}\Delta C_N & \dots \dots \pm 0.010 \\ \Delta C_A & \dots \dots \pm 0.005 \\ \Delta C_m & \dots \dots \pm 0.005\end{aligned}$$

Table II presents the measured static aerodynamic coefficients, including the axial-force coefficient with the correction for base pressure.

#### PREDICTION METHODS

In terms of the Mach number between the shock wave and the body  $M_l$ , several flow combinations will occur for  $\alpha = 0^\circ$  and for the range of cone half-angles and nose bluntness ratios tested. For the sharp cone with  $\theta < \theta_{det}$  (fig. 5(a)), the shock wave is attached and the local Mach number is supersonic. If  $\theta > \theta_{det}$  there will be subsonic flow over the entire body with the sonic line (locus of points for which  $M_l = 1$ ) extending from the shock wave to the base of the body, as shown in figure 5(b). When the cone is spherically blunted and  $\theta \ll \theta_{det}$  (fig. 5(c)), there is subsonic flow over the nose region and supersonic flow over the conical region. The sonic line extends from the shock wave to near the sphere-cone junction of the body. If  $\theta > \theta_{det}$  (fig. 5(d)), subsonic flow occurs over the entire body (regardless of the nose bluntness) and the flow conditions are similar to those of figure 5(b). The most complicated flow condition occurs when there is subsonic flow at the nose, but  $\theta$  is not small enough to allow the flow to become completely supersonic aft of the sphere-cone junction and not large enough to produce total subsonic flow in the shock layer (fig. 5(e)). The sonic line can assume several shapes for values of  $\theta$  in this range, including the one shown in figure 5(e). In helium at  $M_\infty = 20.3$ , reference 12 shows that  $\theta_{det}$  is approximately  $50.6^\circ$ . For angles of attack other than  $0^\circ$ , several local flow combinations (including cross flow) occur over the body, depending on the combination of cone half-angle, nose bluntness, and angle of attack.

A number of numerical methods were used to predict shock shapes and pressure coefficients for the configurations studied. These methods were used primarily because of their accessibility and because they covered the range of flow conditions being studied. No attempt was made to compare the numerical methods in terms of computer time required versus accuracy of results. In addition to using integrated pressure coefficients to determine predicted static aerodynamic coefficients, Newtonian values from reference 13 were also obtained for comparison. The following table lists the numerical methods used and indicates the local flow conditions (as previously described) to which they were applied:

Method	Reference	$\alpha$ capability	All supersonic	All subsonic	Subsonic nose, supersonic cone	Subsonic nose, mixed on cone
Method of lines	14	x	x			
Kumar and Graves <sup>a</sup>	15	x			x	x
Lomax and Inouye	16				x	
Zoby and Graves	17				x	
3-D Blunt Body	18	x			x	
Sutton	19			x	x	x
Barnwell	20	x		x		
South	21			x		
Gnoffo	22			x		

<sup>a</sup>Solution includes the effects of viscosity.

Although several of the preceding methods are described in reference 23, a brief description of each is presented in this paper for quick referral and to note any differences in their application.

#### Method of Lines

The method of lines (refs. 14 and 24) is a computational technique developed by E. B. Klunker, Jerry C. South, and Ruby M. Davis to determine the inviscid flow field about sharp-nosed conical configurations at incidence in a supersonic flow. The method, which makes use of the self-similarity property of conical flow, is applied to the nonlinear inviscid steady-flow equations. All but one of the independent variables in the partial differential equations are discretized so that a coupled system of approximate, simultaneous, ordinary differential-difference equations is obtained. Initial values of these differential-difference equations are determined from the shock relations after the shock shape is estimated or otherwise specified. The system of equations is integrated numerically from the shock wave toward the body, and an iterative process is utilized for adjusting the shock shape to satisfy the boundary condition of flow tangency on the body.

#### Method of Kumar and Graves

The method of Kumar and Graves (ref. 15) is used to compute hypersonic viscous flow over spherically blunted cones of large half-angle at small angles of attack in the plane of symmetry of the flow field. Time-dependent, viscous shock-layer equations in body-oriented coordinates are used to describe the flow field. The shock wave is treated as a discontinuity, across which the Rankine-Hugoniot relations are used to compute the flow conditions behind the shock. A time-marching, second-order-accurate, finite-difference method is used to solve the equations for a perfect gas. A fourth-order damping method is used to control the transient oscillations in the flow quantities. An analytical expression is given to determine the pressure in planes other than the symmetry plane. The results presented herein from this method were generated by Ajay Kumar, research associate with Old Dominion Research Foundation, Norfolk, Virginia.

#### Method of Lomax and Inouye

The method of Lomax and Inouye (refs. 16, 25, and 26) is used to calculate the inviscid flow field around blunt-nosed bodies at supersonic speeds. The equations of motion are solved numerically for plane or axisymmetric bodies at zero angle of attack and for a perfect gas or a real gas in thermodynamic equilibrium. An inverse finite-difference procedure is used for the subsonic-transonic region and the solution is iterated until the desired body shape is obtained. A solution is obtained that extends sufficiently far into the supersonic region to provide initial conditions for a continuing analysis by the method of characteristics.

### Method of Zoby and Graves

This method (ref. 17) provides a rapid (in regard to computer time) approximate means for predicting perfect-gas, inviscid, supersonic, and hypersonic flow conditions about spheres, ellipsoids, paraboloids, and hyperboloids which may have conical afterbodies. An approximation is made to the normal momentum equation which allows an independent evaluation of the pressure throughout the shock layer. An iterative technique scales the shock to the specified body in the subsonic and low supersonic region of the flow field. In the downstream supersonic region, the shock shape is computed by a marching procedure for successive points. The shock wave is first assumed and then iterated upon until the specified body is obtained.

### 3-D Blunt Body Method

This method, which is similar to the one described in reference 18, is a time-dependent, finite-difference technique from which the three-dimensional, inviscid flow field about smooth bodies, both axisymmetric and nonaxisymmetric, can be computed. Steady-flow solutions are obtained by starting with an initial guess and allowing computations to proceed until no changes with time are observed.

### Sutton's Method

A detailed description of Sutton's method for a fully coupled solution of the radiative flow field about an ablating entry body is given in reference 19. For this method, the flow field is separated into an inner viscous layer and an outer inviscid layer. Both laminar and turbulent boundary layers can be considered, and the inviscid flow field is solved by using a second-order time-asymptotic procedure. Thermochemical equilibrium properties are determined for a given gas from the elemental mass fraction and two state properties (pressure and enthalpy). Although several program options are available, the results presented herein correspond to an inviscid flow-field solution for a perfect gas. The results from this method were generated by Kenneth Sutton of the Langley Research Center.

### Barnwell's Method

Barnwell's method (refs. 20 and 27) is a two-step, time-dependent procedure of second-order accuracy for computing the inviscid adiabatic flow at supersonic and hypersonic speeds about plane and axisymmetric bodies with sharp corners and about smooth nonaxisymmetric bodies. A finite-difference scheme is used at the surface of the body and between the shock and the surface. The program may be used for a perfect gas or for thermochemical-equilibrium airflow and is formulated so that input for  $\gamma$  may be given one value in the free stream and another value in the post-shock region. This input capability for  $\gamma$  provides real-gas phenomena approximations with perfect-gas models. Steady-flow results are approached asymptotically after many time steps.

### South's Method

This method (ref. 21) provides rapid, approximate calculations for axisymmetric supersonic inviscid flow of a perfect gas past blunt bodies with sonic corners. Numerical solutions are obtained for the system of differential equations derived from the one-strip method of integral relations. This method can also be applied to sharp-nosed bodies by assuming a small nose bluntness that approaches the sharp case.

### Gnoffo's Method

This method (ref. 22) is a modification of a two-strip method of integral relations. The results presented herein from this method were generated by Peter A. Gnoffo of the Langley Research Center.

## RESULTS AND DISCUSSION

In the figures containing measured and predicted shock shapes, the symbol size is approximately 2 percent of the model base radius (the estimated error in measuring these values). The symbols which indicate the values of the measured static aerodynamic coefficients are sized according to the balance uncertainties.

### Shock Shapes for 0° Angle of Attack

Sharp cones with attached shocks.- Measured and predicted shock shapes for  $\theta = 30^\circ$  and  $45^\circ$  (figs. 6(a) and (b)) show the straight shock wave that is obtained when the local Mach number is supersonic. The inviscid methods of references 12 and 14 underpredict the slope of the shock by about  $1^\circ$  for both cone half-angles. An undocumented, laminar, similar-boundary-layer solution written by Ralph D. Watson of the Langley Research Center was used to calculate the displacement thicknesses for these two cases. The predicted values accounting for the boundary-layer displacement thicknesses were in excellent agreement (within 2 percent) with the measured shock shapes (figs. 6(a) and (b)).

Sharp cones with detached shocks.- For  $\theta = 60^\circ$  and  $70^\circ$  (figs. 6(c) and (d)), the shock wave is detached and the local Mach number is subsonic. The method of reference 21 was used to predict the shock shapes for the sharp cones by inputting a nose bluntness ratio of 0.01. Except in the stagnation region, good agreement (within 5 percent) with the measured shock shapes from the present investigation was obtained for both cone half-angles.

Other experimental data were available for comparison with the  $\theta = 70^\circ$  case (fig. 6(d)). In the stagnation region, the measured values from reference 5 differ from those of the present investigation by as much as 10 percent. Measured values from the results of reference 7 agree within 4 percent with the results of the present investigation. (The results from ref. 7 in fig. 6(d) were read from original schlieren negatives by the present authors.)

Blunted cones with subsonic nose regions and supersonic conical regions.-

Measured and predicted shock shapes for the spherically blunted cones are presented in figure 7. For  $\theta = 30^\circ$  and  $r_n/r_b = 0.25$  and  $0.50$  (figs. 7(a) and (b)), the local flow is subsonic in the nose region and supersonic in the conical region as indicated by the predicted (ref. 19) sonic line. Excellent agreement between measured and predicted values is observed in the upstream region for  $x/r_b < 0.6$  (fig. 7(a)). Only the viscous solution of reference 15 continues to agree with the measurements in the downstream region, which indicates that viscous effects occurring in the region aft of the spherical nose affect the shock shape.

The comparison for  $\theta = 30^\circ$  and  $r_n/r_b = 0.50$  (fig. 7(b)) is essentially a resolution of the nose region from the 0.25 nose bluntness case, since all the prediction techniques are scaled by  $r_n$ . The viscous solution of reference 15 underpredicts the measured values just aft of the sphere-cone junction and then approaches the measurements again toward the rear of the body. The underprediction in the sphere-cone junction region is possibly due to the differencing technique used in this area where the slope of the body surface is discontinuous. The inviscid method of reference 19 provides excellent agreement with measured values, but at the very rear of the body the predictions of this method begin to approach predictions by the other three inviscid methods as the comparisons become similar to those for the 0.25 nose bluntness case of figure 7(a).

Blunted cones with sonic lines aft of the spherical nose.- Subsonic and supersonic flow occurs in the local flow field downstream of the spherical nose for the  $45^\circ$  cone (figs. 7(c) and (d)). For both nose bluntness ratios, the predicted (refs. 15 and 19) and measured shock shapes are in excellent agreement in the nose region, but the inviscid method of reference 19 underpredicts the shock location in the downstream region, as was observed previously for  $\theta = 30^\circ$  (figs. 7(a) and (b)).

As shown by the sonic lines (predicted by ref. 20) in figures 7(e), (f), (g), and (h), the entire local flow field is subsonic for  $\theta = 60^\circ$  and  $70^\circ$  and  $r_n/r_b = 0.25$  and  $0.50$ . For  $\theta = 60^\circ$  and  $r_n/r_b = 0.25$  (fig. 7(e)), only the method of reference 20 provides excellent agreement with the measured shock locations over the entire body. The other methods (refs. 19, 21, and 22) slightly underpredict the measured values in the nose and corner regions. All four methods show good to excellent agreement with measurement for  $\theta = 60^\circ$  and  $r_n/r_b = 0.50$  (fig. 7(f)), except for the methods of references 19 and 21 which underpredict the measurements in the nose region by approximately 10 percent. In figure 7(g) for  $\theta = 70^\circ$  and  $r_n/r_b = 0.25$ , the method of reference 20 provides good agreement in the nose region with the agreement improving farther downstream. The method of reference 19 underpredicts the stagnation-point standoff distance by about 6 percent but shows excellent agreement downstream also. Both integral methods (refs. 21 and 22) tend to underpredict the entire shock shape (by as much as 10 percent in the stagnation region and at the corner), and the one-strip method of reference 21 provides the closer prediction of the measured values. For  $\theta = 70^\circ$  and  $r_n/r_b = 0.50$  (fig. 7(h)), the shock shape is underpredicted by all four methods, except in the corner region, where references 19 and 20 provide good agreement.

Shock shapes measured using a flat-faced cylinder to represent a 90° cone at 0° angle of attack are compared with the experimental data of reference 5 and three predictions in figure 8. There is excellent agreement between the measured values in the stagnation region, but they differ by approximately 11 percent in the corner region of the flow field. The method of reference 20 provides good agreement (within 5 percent) with values measured in the present investigation; however, these measured values are underpredicted by the methods of references 21 and 22 by as much as 15 percent.

The excellent agreement between measured and predicted shock shapes for the sphere shown in figure 9 is expected since all the predictions have been shown to provide excellent agreement in nose regions for  $\theta < \theta_{det}$ . The underprediction by the method of reference 17 is probably due to approximations made to the normal momentum equation in that method. The results of figure 9 are similar to those presented in reference 23 from tests conducted in the Langley 6-inch expansion tube for a free-stream Mach number of 6.02 in helium.

#### Shock Shapes for 10° Angle of Attack

Sharp cones with attached shocks.- Results from reference 14 are compared with measurements for the 30° cone at 10° angle of attack in figure 10(a). The straight shock waves on both the windward and leeward sides indicate that the local flow field is completely supersonic. As observed for  $\alpha = 0^\circ$  (fig. 6(a)), reference 14 underpredicts the measured shock shapes. The underprediction is worse on the leeward side where viscous effects are more pronounced.

For the 45° cone at 10° angle of attack (fig. 10(b)), the local flow field on the windward side becomes subsonic since the effective cone half-angle exceeds  $\theta_{det}$ . By running the program of reference 14 (which is applicable only for  $M_1 > 1$ ) for small increments of angle of attack, the predicted local flow first went subsonic on the windward side at approximately 4.2° angle of attack. On the leeward side, the local flow is supersonic and the shock shape is underpredicted by reference 14, as was the case for the 30° cone.

Sharp cones with detached shocks.- Because the numerical methods used in this study were not applicable for sharp cones with detached shocks at 10° angle of attack, only the experimental values are shown in figures 11(a) and (b).

Blunted cones with subsonic nose regions and supersonic conical regions.- Predicted shock shapes from references 15 and 18 are compared with measured values for  $\theta = 30^\circ$  and  $r_n/r_b = 0.25$  and  $0.50$  (figs. 12(a) and (b)). The two methods agree with one another and with measured values in the nose region for both nose bluntness ratios. The viscous solution of reference 15 is in excellent agreement (within 2 percent) with measurement in the downstream region for  $r_n/r_b = 0.25$ , whereas values from reference 18 underpredict the measurements by as much as 10 percent at  $r/r_b = 1.0$ . For  $r_n/r_b = 0.50$  (fig. 12(b)), measurement and prediction are in good agreement in the nose region and along the windward side; however, both numerical methods underpredict the measured shock shapes along the leeward side. This underprediction by the viscous solution of reference 15 is similar to the results shown in figure 7(b) for the same sphere-cone at  $\alpha = 0^\circ$ .

Blunted cones with sonic lines aft of the spherical nose. - Except in the most downstream region (figs. 12(c) and (d)), the viscous method of reference 15 provided excellent agreement with measured values for  $\theta = 45^\circ$  and  $r_n/r_b = 0.25$  and 0.50.

For  $\theta = 60^\circ$  and  $r_n/r_b = 0.25$  and 0.50 (figs. 12(e) and (f)), the shock shapes predicted by reference 20 are in excellent agreement with the measurements. This method also provides excellent agreement with measured values for  $\theta = 70^\circ$  and both nose bluntness ratios (figs. 12(g) and (h)), except in the stagnation region for  $r_n/r_b = 0.50$  (fig. 12(h)), where the measured values are underpredicted.

#### Measured and Predicted Static Aerodynamic Coefficients

Measured values of aerodynamic coefficients from reference 6 and predicted values based on Newtonian theory (ref. 13) and the method of lines (ref. 14) are compared with values measured in this investigation for the  $30^\circ$  sharp cone (fig. 13(a)). Excellent agreement between the present normal-force and pitching-moment coefficients and those of reference 6 are observed, but the difference in measured axial-force coefficients is approximately 4 percent. Both prediction methods provide excellent agreement with measured values except for the prediction of the axial-force coefficient by the method of reference 13.

For the  $45^\circ$  sharp cone (fig. 13(b)), the method of reference 13 predicts the normal-force and pitching-moment coefficients but, as shown for the  $30^\circ$  sharp cone, underpredicts the axial-force coefficient. The predicted values from reference 14 show excellent agreement with measured values for all three coefficients up to an angle of attack of approximately  $4^\circ$ , which is the maximum angle of attack for local supersonic flow on the windward side.

Measured values from reference 6 as well as predicted values from references 13 and 21 are presented for the  $60^\circ$  sharp cone in figure 13(c). The axial-force and normal-force coefficients from reference 6 are in good agreement with data from this investigation; however, the difference in pitching-moment coefficients between reference 6 and the present results is approximately 35 percent for  $\alpha = 10^\circ$ . Newtonian theory (ref. 13) overpredicts both  $C_N$  and  $C_m$  and underpredicts  $C_A$  by approximately 5 percent at  $\alpha = 0^\circ$ . Excellent agreement is observed between measured  $C_A$  at  $\alpha = 0^\circ$  and the value predicted by the method of reference 21. There is excellent agreement between measurement and prediction for the sharp  $70^\circ$  cone (fig. 13(d)). The only exception is the axial-force coefficient, which the method of reference 13 overpredicts by approximately 4 percent.

Comparisons between measured and predicted (refs. 13, 15, and 19) static aerodynamic coefficients for  $\theta = 30^\circ$  and  $r_n/r_b = 0.25$  (fig. 14(a)) are in excellent agreement except for the overprediction of  $C_A$  by the method of reference 15 for angles of attack in excess of  $6^\circ$ . The divergent character of the predicted  $C_A$  for this case is caused by unrealistically high pressure coefficients which are obtained when the cross-flow velocity derivative on the leeward

side becomes large (unbounded) as the angle of attack is increased. For a nose bluntness of 0.50 and  $\theta = 30^\circ$  (fig. 14(b)), there is excellent agreement between measurement and prediction except for the axial-force coefficient. Newtonian theory (ref. 13) overpredicts the measured values by as much as 14 percent at  $\alpha = 0^\circ$ . The method of reference 15 tends to follow the proper trends but over-predicts  $C_A$  by more than 10 percent for the higher angles of attack. At  $\alpha = 0^\circ$  the prediction by reference 19 is excellent.

Again, for  $\theta = 45^\circ$  and  $r_n/r_b = 0.25$  and 0.50 (figs. 14(c) and (d)), there is excellent agreement between measured and predicted normal-force and pitching-moment coefficients, but there is some disagreement for the axial-force coefficient. For  $r_n/r_b = 0.25$  (fig. 14(c)), the method of reference 15 and the point calculated by the method of reference 19 are in excellent agreement with the axial-force coefficients for  $-4^\circ \leq \alpha \leq 4^\circ$ , and Newtonian values under-predict  $C_A$  by about 8 percent in this area. For  $r_n/r_b = 0.50$  (fig. 14(d)), the value predicted by the method of reference 19 and the Newtonian predictions (ref. 13) are in excellent agreement with measured axial-force coefficients for  $-4^\circ < \alpha < 8^\circ$ . The method of reference 15 shows good agreement for  $-4^\circ \leq \alpha \leq 4^\circ$ .

Similar comparisons are shown in figures 14(e) and (f) for  $\theta = 60^\circ$  and  $r_n/r_b = 0.25$  and 0.50. The predictions of references 13 and 20 show fair agreement with measured normal-force coefficients over the range of  $\alpha$  tested and measured pitching-moment coefficients for  $-4^\circ < \alpha < 6^\circ$ , but poor agreement (not better than 10 percent) with measured pitching-moment coefficients for  $\alpha \geq 8^\circ$ . Except for the values predicted by reference 13, there is good to excellent agreement with measured axial-force coefficients by all the prediction methods.

Similar comparisons are also shown for  $\theta = 70^\circ$  and  $r_n/r_b = 0.25$  and 0.50 (figs. 14(g) and (h)). In general, there is excellent agreement between prediction and measurement; however,  $C_m$  is underpredicted by the method of reference 20, and  $C_A$  is overpredicted by the method of reference 13.

#### The Effects of Nose Bluntness on Static Aerodynamic Coefficients

The static aerodynamic coefficients that were obtained experimentally for  $\theta = 30^\circ$  and all three nose bluntness ratios are presented in figure 15. The pitching-moment coefficient is relatively sensitive to nose bluntness, increasing nose bluntness producing less nose-down pitch (less positive static stability). The normal-force and axial-force coefficients are relatively insensitive to the increase in the nose bluntness ratio from 0 to 0.25, but a nose bluntness ratio of 0.50 is shown to increase the axial-force coefficient and decrease the normal-force coefficient at the higher angles of attack.

For the cones with  $\theta = 45^\circ$ ,  $60^\circ$ , and  $70^\circ$  (figs. 16, 17, and 18, respectively), only the axial-force coefficient for  $\theta = 45^\circ$  at small angles of attack is sensitive to the change in nose bluntness, increasing bluntness resulting in decreasing axial-force coefficient. These results indicate that the nose bluntness of proposed planetary probes employing large cone half-angles can be based on other design requirements such as heating or packaging constraints.

## CONCLUDING REMARKS

Shock shapes for sharp and spherically blunted cones having cone half-angles of  $30^\circ$ ,  $45^\circ$ ,  $60^\circ$ , and  $70^\circ$  and nose bluntness ratios of 0, 0.25, and 0.50 were obtained for  $\alpha = 0^\circ$  and  $10^\circ$  in Mach 20.3 helium flow. Static aerodynamic coefficients from  $\alpha = -4^\circ$  to  $12^\circ$  were also measured for the family of cone models. The measured results were compared with predicted values obtained from several numerical solution methods and simple engineering methods.

For sharp cones with attached shock waves, the method of lines (NASA TR R-374) generally underpredicted the measured shock shapes for both angles of attack. Calculating the boundary-layer displacement thickness and adding that to the original body to get an equivalent shape resulted in excellent agreement between measured and predicted values. For spherically blunted cones with subsonic nose regions, and either supersonic or mixed subsonic and supersonic flow over the cone, all predictions of the shock shapes in the nose regions were excellent. In the downstream regions, the viscous solutions of Kumar and Graves (AIAA Paper No. 77-172) showed significantly better agreement with measured values than the other (inviscid) numerical methods. For the spherically blunted cones with sonic corners, Barnwell's method (NASA TN D-6283) provided good agreement with measured shock shapes for both nose bluntness ratios for  $\alpha = 0^\circ$  and  $10^\circ$ .

Newtonian predictions (NASA TR R-127) showed excellent agreement with measured normal-force and pitching-moment coefficients for all nose bluntness ratios and all cone half-angles except  $60^\circ$ . Axial-force Newtonian predictions did not agree with measured results. Static aerodynamic coefficients predicted by the method of lines are in excellent agreement with measured values for the region of applicability (sharp cones with local Mach number in excess of unity). The viscous solution of Kumar and Graves showed excellent agreement with both normal-force and pitching-moment coefficients over the range of angles of attack for  $\theta = 30^\circ$  and  $45^\circ$ , and  $r_n/r_b = 0.25$  and  $0.50$ ; however, this method tended to become divergent and began to overpredict measured axial-force coefficients for increased nose bluntness, cone half-angle, and angle of attack. Barnwell's method followed the proper trends for all static aerodynamic coefficients but showed generally fair to poor agreement with measured values except for its prediction of axial-force coefficients for  $\theta = 60^\circ$  and  $70^\circ$  and  $r_n/r_b = 0.25$  and  $0.50$ . Predictions of the axial-force coefficients by those methods which were limited to  $\alpha = 0^\circ$  were good to excellent in all cases.

The effects of nose bluntness on the static aerodynamic coefficients for the  $60^\circ$  and  $70^\circ$  cones were essentially negligible. These findings indicate that the selection of the nose bluntness for proposed planetary probes employing large cone half-angles can be based on other design requirements such as heating or packaging constraints. The experimental data base should now be extended to include other Mach numbers and ratios of specific heats, so that existing numerical techniques might be completely evaluated. Also, heat transfer tests are needed as part of the data base to provide evaluation for the viscous solutions which are now available.

Langley Research Center  
National Aeronautics and Space Administration  
Hampton, VA 23665  
January 19, 1979

## REFERENCES

1. Moss, James N.; Zoby, E. Vincent; and Sutton, Kenneth: A Study of the Aero-thermal Environment for the Pioneer Venus Multiprobe Mission. AIAA Paper No. 77-766, June 1977.
2. Sutton, Kenneth: Radiative Heating About Outer Planet Entry Probes. J. Spacecr. & Rockets, vol. 13, no. 5, May 1976, pp. 294-300.
3. Sutton, K.; Jones, J. J.; and Powell, R. W.: Effect of Probe Configuration on Radiative Heating During Jupiter Entry. Thermophysics of Spacecraft and Outer Planet Entry Probes, Allie M. Smith, ed., American Inst. Aeronaut. & Astronaut., c.1977, pp. 355-375.
4. Olstad, Walter B.: Developing a Technology Base in Planetary Entry Aero-thermodynamics. Space Activity - Impact on Science and Technology, P. Contensou and W. F. Hilton, eds., Pergamon Press, Inc., c.1976, pp. 257-291.
5. Stewart, David A.; and Inouye, Mamoru: Shock Shapes and Pressure Distributions for Large-Angle Pointed Cones in Helium at Mach Numbers of 8 and 20. NASA TN D-5343, 1969.
6. Maddalon, Dal V.: Aerodynamic Characteristics of the Sharp Right Circular Cone at Mach 20.3 and Angles of Attack to  $110^\circ$  in Helium. NASA TN D-3201, 1966.
7. Jones, Robert A.; and Hunt, James L.: Measured Pressure Distributions on Large-Angle Cones in Hypersonic Flows of Tetrafluoromethane, Air, and Helium. NASA TN D-7429, 1973.
8. Miller, Charles G., III: Shock Shapes on Blunt Bodies in Hypersonic-Hypervelocity Helium, Air, and CO<sub>2</sub> Flows, and Calibration Results in Langley 6-Inch Expansion Tube. NASA TN D-7800, 1975.
9. Cleary, Joseph W.; and Duller, Charles E.: Effects of Angle of Attack and Bluntness on the Hypersonic Flow Over a  $15^\circ$  Semiapex Cone in Helium. NASA TN D-5903, 1970.
10. Arrington, James P.; Joiner, Roy C., Jr.; and Henderson, Arthur, Jr.: Longitudinal Characteristics of Several Configurations at Hypersonic Mach Numbers in Conical and Contoured Nozzles. NASA TN D-2489, 1964.
11. Woods, William C.; and Arrington, James P.: Electron-Beam Flow Visualization - Applications in the Definition of Configuration Aero-thermal Characteristics. AIAA Paper No. 72-1016, Sept. 1972.
12. Mueller, James N.: Equations, Tables and Figures for Use in the Analysis of Helium Flow at Supersonic and Hypersonic Speeds. NACA TN 4063, 1957.

13. Wells, William R.; and Armstrong, William O.: Tables of Aerodynamic Coefficients Obtained From Developed Newtonian Expressions for Complete and Partial Conic and Spheric Bodies at Combined Angles of Attack and Sideslip With Some Comparisons With Hypersonic Experimental Data. NASA TR R-127, 1962.
14. Klunker, E. B.; South, Jerry C., Jr.; and Davis, Ruby M.: Calculation of Nonlinear Conical Flows by the Method of Lines. NASA TR R-374, 1971.
15. Kumar, Ajay; and Graves, R. A., Jr.: Numerical Solution of the Viscous Hypersonic Flow Past Blunted Cones at Angle of Attack. AIAA Paper No. 77-172, Jan. 1977.
16. Lomax, Harvard; and Inouye, Mamoru: Numerical Analysis of Flow Properties About Blunt Bodies Moving at Supersonic Speeds in an Equilibrium Gas. NASA TR R-204, 1964.
17. Zoby, Ernest V.; and Graves, Randolph A., Jr.: A Computer Program for Calculating the Perfect Gas Inviscid Flow Field About Blunt Axisymmetric Bodies at an Angle of Attack of  $0^\circ$ . NASA TM X-2843, 1973.
18. Moretti, Giro; and Bleich, Gary: Three-Dimensional Flow Around Blunt Bodies. AIAA J., vol. 5, no. 9, Sept. 1967, pp. 1557-1562.
19. Sutton, Kenneth: Characteristics of Coupled Nongray Radiating Gas Flows With Ablation Product Effects About Blunt Bodies During Planetary Entries. Ph. D. Thesis, North Carolina State Univ. at Raleigh, 1973. (Available as NASA TM X-72078.)
20. Barnwell, Richard W.: A Time-Dependent Method for Calculating Supersonic Angle-of-Attack Flow About Axisymmetric Blunt Bodies With Sharp Shoulders and Smooth Nonaxisymmetric Blunt Bodies. NASA TN D-6283, 1971.
21. South, Jerry C., Jr.: Calculation of Axisymmetric Supersonic Flow Past Blunt Bodies With Sonic Corners, Including a Program Description and Listing. NASA TN D-4563, 1968.
22. Gnoffo, Peter A.: Inviscid, Nonadiabatic Flow Fields Over Blunt, Sonic Corner Bodies for Outer Planet Entry Conditions by a Method of Integral Relations. NASA TP-1133, 1978.
23. Miller, Charles G., III: A Comparison of Measured and Predicted Sphere Shock Shapes in Hypersonic Flows With Density Ratios From 4 to 19. NASA TN D-8076, 1975.
24. Klunker, E. B.; South, Jerry C., Jr.; and Davis, Ruby M.: Computer Program for Calculating Supersonic Flow About Circular, Elliptic, and Bielliptic Cones by the Method of Lines. NASA TM X-2437, 1972.

25. Inouye, Mamoru; and Lomax, Harvard: Comparison of Experimental and Numerical Results for the Flow of a Perfect Gas About Blunt-Nosed Bodies. NASA TN D-1426, 1962.
26. Inouye, Mamoru; Rakich, John V.; and Lomax, Harvard: A Description of Numerical Methods and Computer Programs for Two-Dimensional and Axisymmetric Supersonic Flow Over Blunt-Nosed and Flared Bodies. NASA TN D-2970, 1965.
27. Barnwell, Richard W.; and Davis, Ruby M.: A Computer Program for Calculating Inviscid, Adiabatic Flow About Blunt Bodies Traveling at Supersonic and Hypersonic Speeds at Angle of Attack. NASA TM X-2334, 1971.

TABLE I.- MEASURED SHOCK DETACHMENT DISTANCES

(a)  $\alpha = 0^\circ$ 

$\theta$ , deg	Detachment distances nondimensionalized by base radius $\Delta/r_b$ for $r/r_b$ of -													
	0	0.1	0.2	0.3	0.4	0.5	0.6	0.7	0.8	0.9	1.0	1.1	1.2	1.3
$r_n/r_b = 0$														
30	0	0.042	0.078	0.118	0.156	0.193	0.231	0.260	0.296	0.330	0.366	0.227	0.088	-----
45	0	.035	.067	.104	.138	.171	.209	.240	.276	.311	.349	.282	.215	0.150
60	.125	.171	.218	.259	.298	.335	.366	.395	.420	.444	.459	.409	.358	.302
70	.298	.331	.358	.379	.396	.415	.427	.438	.450	.454	.454	.419	.371	.317
90	.608	.608	.601	.594	.587	.580	.567	.546	.526	.505	.471	.444	.416	.369
Sphere	.204	.208	.210	.216	.225	.241	.272	.307	.369	.470	.827	.742	.650	.559
$r_n/r_b = 0.25$														
30	0.056	0.061	0.105	0.190	0.238	0.259	0.268	0.285	0.301	0.324	0.372	0.234	0.098	-----
45	.054	.056	.089	.120	.145	.170	.208	.239	.278	.305	.344	.276	.210	0.139
60	.163	.175	.219	.258	.299	.339	.362	.398	.421	.443	.461	.413	.364	.315
70	.328	.340	.365	.387	.410	.422	.438	.453	.459	.461	.465	.430	.387	.334
$r_n/r_b = 0.50$														
30	0.108	0.108	0.122	0.147	0.189	0.293	0.376	0.448	0.494	0.517	0.537	0.373	0.207	0.031
45	.109	.109	.117	.137	.183	.222	.248	.272	.294	.317	.349	.276	.204	.133
60	.194	.198	.215	.249	.287	.319	.350	.375	.399	.422	.435	.395	.350	.298
70	.347	.361	.381	.407	.425	.438	.458	.466	.476	.480	.480	.440	.393	.339

TABLE I.- Continued

(b)  $\alpha = 10^\circ$ ; windward side

$\theta$ , deg	Detachment distances nondimensionalized by base radius $\Delta/r_b$ for $r/r_b$ of -													
	0	0.1	0.2	0.3	0.4	0.5	0.6	0.7	0.8	0.9	1.0	1.1	1.2	1.3
$r_n/r_b = 0$														
30	0	0.053	0.096	0.143	0.181	0.225	0.262	0.298	0.334	0.375	0.415	0.275	0.147	0.009
45	0	.048	.094	.144	.188	.238	.277	.315	.352	.392	.419	.346	.275	.192
60	.121	.176	.232	.278	.315	.346	.373	.393	.410	.417	.426	.370	.307	.236
70	.280	.313	.342	.365	.390	.407	.411	.417	.415	.405	.395	.345	.276	.202
$r_n/r_b = 0.25$														
30	0.059	0.069	0.094	0.170	0.215	0.245	0.276	0.308	0.347	0.383	0.421	0.282	0.146	0.023
45	.054	.062	.096	.139	.185	.227	.272	.308	.349	.382	.416	.349	.273	.193
60	.156	.173	.221	.267	.302	.333	.356	.375	.390	.396	.404	.346	.279	.200
70	.303	.317	.346	.373	.389	.399	.409	.411	.409	.397	.389	.332	.272	.200
$r_n/r_b = 0.50$														
30	0.109	0.107	0.115	0.134	0.174	0.269	0.330	0.374	0.386	0.407	0.428	0.288	0.151	0.011
45	.111	.111	.120	.146	.190	.239	.283	.322	.359	.390	.425	.351	.272	.194
60	.193	.197	.216	.261	.302	.330	.355	.382	.397	.408	.410	.340	.280	.206
70	.326	.337	.354	.383	.400	.418	.421	.421	.420	.414	.400	.338	.269	.196

TABLE I:- Concluded

(c)  $\alpha = 10^\circ$ ; leeward side

$\theta$ , deg	Detachment distances nondimensionalized by base radius $\Delta/r_b$ for $r/r_b$ of -													
	0	0.1	0.2	0.3	0.4	0.5	0.6	0.7	0.8	0.9	1.0	1.1	1.2	1.3
$r_n/r_b = 0$														
30	0	0.043	0.077	0.109	0.142	0.174	0.204	0.232	0.260	0.289	0.325	0.177	0.028	-----
45	0	.031	.067	.092	.125	.156	.185	.213	.242	.269	.296	.222	.148	0.076
60	.121	.172	.218	.254	.291	.329	.366	.399	.423	.452	.481	.445	.408	.366
70	.280	.315	.349	.380	.407	.430	.453	.472	.488	.503	.514	.482	.447	.407
$r_n/r_b = 0.25$														
30	0.059	0.061	0.111	0.218	0.301	0.375	0.402	0.431	0.437	0.446	0.467	0.314	0.161	0.008
45	.054	.064	.100	.135	.154	.173	.195	.222	.245	.274	.301	.232	.156	.082
60	.156	.165	.208	.248	.285	.319	.356	.383	.413	.442	.465	.429	.394	.357
70	.303	.322	.351	.382	.411	.433	.457	.481	.495	.505	.510	.478	.442	.409
$r_n/r_b = 0.50$														
30	0.109	0.115	0.130	0.160	0.214	0.329	0.432	0.523	0.602	0.665	0.714	0.581	0.447	0.299
45	.111	.115	.126	.155	.206	.252	.289	.311	.326	.338	.350	.266	.198	.111
60	.193	.193	.206	.246	.284	.323	.353	.385	.416	.443	.466	.431	.393	.352
70	.326	.337	.362	.393	.418	.443	.466	.483	.498	.513	.525	.496	.468	.429

TABLE II.- MEASURED STATIC AERODYNAMIC COEFFICIENTS

(a)  $\theta = 30^\circ$ 

$\alpha$ , deg	$C_N$	$C_{A,corr}$	$C_A$	$C_m$
$r_n/r_b = 0$				
-4	-0.1098	0.5446	0.5420	0.0868
-2	-.0603	.5455	.5432	.0487
0	-.0029	.5459	.5441	.0031
2	.0507	.5439	.5417	-.0379
4	.0953	.5433	.5406	-.0750
6	.1517	.5420	.5391	-.1195
8	.2006	.5425	.5396	-.1569
10	.2586	.5393	.5365	-.2026
12	.3080	.5359	.5331	-.2421
$r_n/r_b = 0.25$				
-4	-0.1018	0.5361	0.5342	0.0698
-2	-.0509	.5364	.5345	.0352
0	-.0037	.5403	.5386	.0038
2	.0570	.5380	.5362	-.0368
4	.1104	.5363	.5344	-.0721
6	.1566	.5365	.5345	-.1022
8	.2099	.5360	.5338	-.1379
10	.2581	.5376	.5353	-.1720
12	.3027	.5391	.5365	-.2026
$r_n/r_b = 0.50$				
-4	-0.0898	0.5602	0.5521	0.0564
-2	-.0490	.5550	.5474	.0315
0	.0019	.5540	.5468	-.0009
2	.0472	.5541	.5467	-.0286
4	.0981	.5609	.5531	-.0596
6	.1375	.5611	.5531	-.0817
8	.1734	.5648	.5567	-.1039
10	.2188	.5729	.5644	-.1306
12	.2628	.5801	.5712	-.1567

TABLE II.- Continued

(b)  $\theta = 45^\circ$ 

$\alpha$ , deg	$C_N$	$C_{A,corr}$	$C_A$	$C_B$
$r_n/r_b = 0$				
-4	-0.0649	1.0953	1.0849	0.0454
-2	-.0270	1.1086	1.0990	.0196
0	.0054	1.1043	1.0952	-.0024
2	.0376	1.1030	1.0933	-.0250
4	.0694	1.0951	1.0848	-.0468
6	.0970	1.0796	1.0692	-.0644
8	.1254	1.0611	1.0509	-.0843
10	.1552	1.0396	1.0300	-.1055
12	.1887	1.0119	1.0029	-.1306
$r_n/r_b = 0.25$				
-4	-0.0740	1.0872	1.0764	0.0483
-2	-.0326	1.0918	1.0815	.0218
0	.0005	1.0959	1.0860	.0015
2	.0363	1.0910	1.0807	-.0231
4	.0660	1.0860	1.0752	-.0417
6	.0991	1.0772	1.0666	-.0630
8	.1294	1.0522	1.0422	-.0824
10	.1613	1.0324	1.0232	-.1038
12	.1852	1.0076	.9987	-.1208
$r_n/r_b = 0.50$				
-4	-0.0592	1.0702	1.0631	0.0365
-2	-.0247	1.0728	1.0664	.0167
0	.0057	1.0760	1.0698	-.0023
2	.0313	1.0711	1.0647	-.0165
4	.0741	1.0671	1.0599	-.0432
6	.1035	1.0571	1.0489	-.0627
8	.1302	1.0438	1.0351	-.0781
10	.1625	1.0266	1.0175	-.1006
12	.1927	1.0046	.9955	-.1202

TABLE II.- Continued

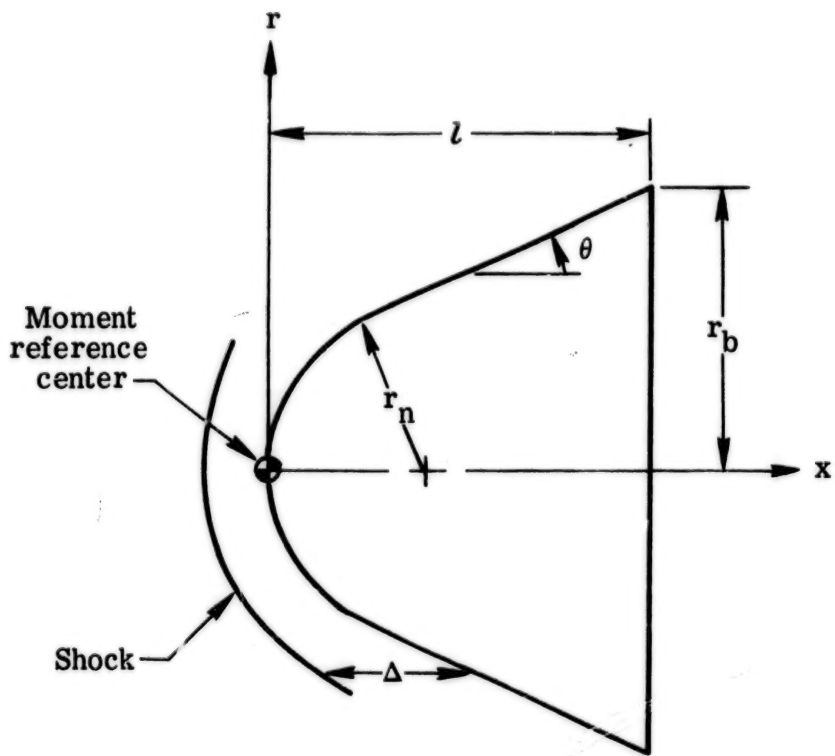
(c)  $\theta = 60^\circ$ 

$\alpha$ , deg	$C_N$	$C_{A,corr}$	$C_A$	$C_m$
$r_n/r_b = 0$				
-4	-0.0093	1.3809	1.3690	0.0101
-2	-.0031	1.3821	1.3708	.0062
0	.0077	1.3857	1.3747	-.0026
2	.0201	1.3902	1.3791	-.0099
4	.0259	1.3836	1.3719	-.0163
6	.0311	1.3757	1.3635	-.0222
8	.0436	1.3594	1.3470	-.0334
10	.0509	1.3463	1.3340	-.0404
12	.0671	1.3233	1.3112	-.0543
$r_n/r_b = 0.25$				
-4	-0.0108	1.3870	1.3756	0.0108
-2	-.0017	1.3921	1.3812	.0036
0	.0050	1.3920	1.3813	-.0023
2	.0115	1.3906	1.3799	-.0078
4	.0197	1.3860	1.3747	-.0148
6	.0277	1.3772	1.3657	-.0213
8	.0373	1.3646	1.3530	-.0294
10	.0512	1.3467	1.3354	-.0406
12	.0632	1.3318	1.3209	-.0507
$r_n/r_b = 0.50$				
-4	-0.0126	1.3773	1.3653	0.0122
-2	-.0061	1.3895	1.3782	.0073
0	.0018	1.3889	1.3782	-.0001
2	.0086	1.3864	1.3758	-.0051
4	.0156	1.3804	1.3693	-.0112
6	.0260	1.3688	1.3573	-.0188
8	.0376	1.3580	1.3463	-.0293
10	.0475	1.3446	1.3331	-.0373
12	.0622	1.3213	1.3101	-.0495

TABLE II.- Concluded

(d)  $\theta = 70^\circ$ 

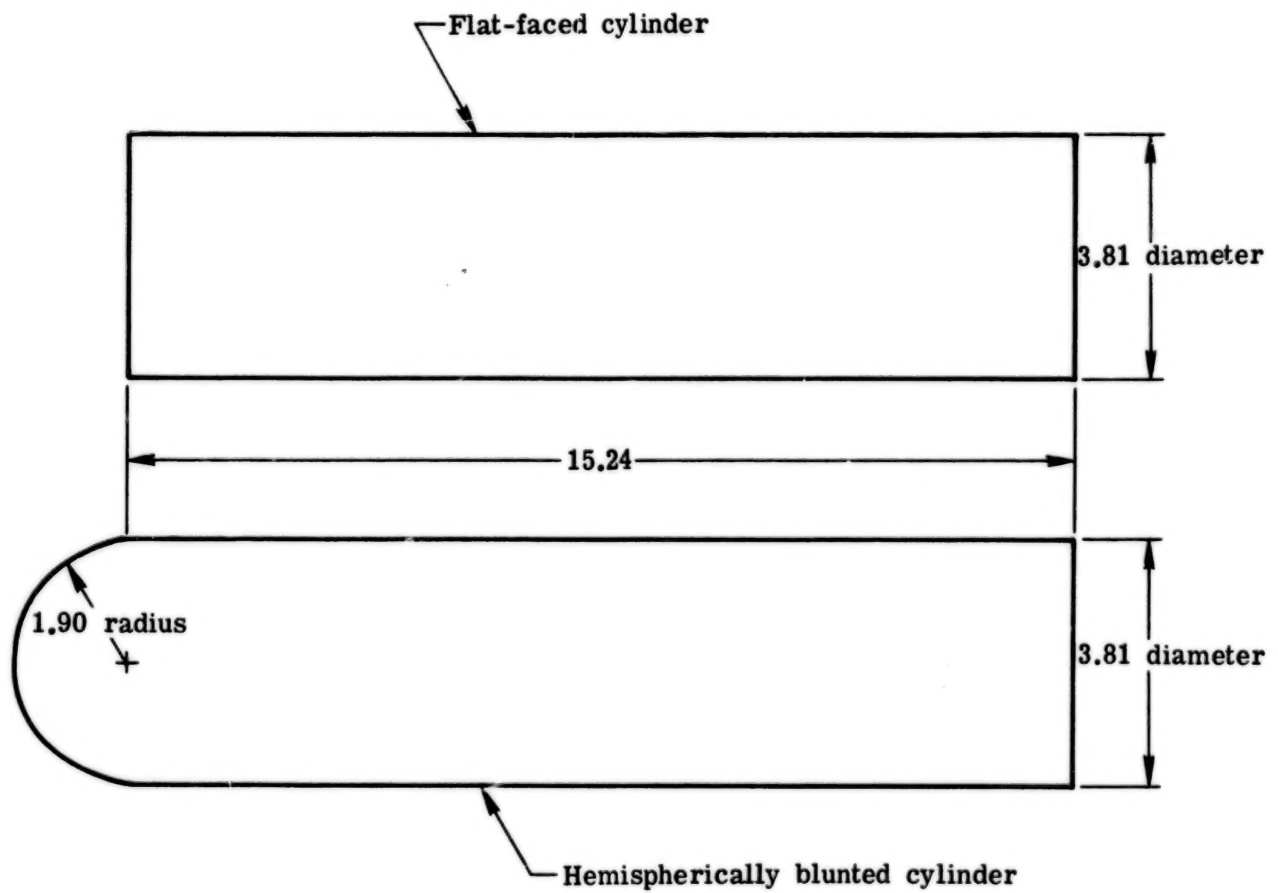
$\alpha$ , deg	$C_N$	$C_{A,corr}$	$C_A$	$C_m$
$r_n/r_b = 0$				
-4	-0.0050	1.4620	1.4491	0.0096
-2	.0004	1.4695	1.4574	.0036
0	.0044	1.4778	1.4664	-.0024
2	.0061	1.4749	1.4635	-.0056
4	.0103	1.4656	1.4537	-.0112
6	.0157	1.4623	1.4500	-.0167
8	.0232	1.4590	1.4465	-.0249
10	.0317	1.4474	1.4352	-.0340
12	.0427	1.4323	1.4205	-.0453
$r_n/r_b = 0.25$				
-4	-0.0062	1.4727	1.4610	0.0117
-2	.0001	1.4787	1.4679	.0044
0	.0027	1.4742	1.4641	.0006
2	.0058	1.4747	1.4647	-.0045
4	.0099	1.4743	1.4636	-.0090
6	.0146	1.4741	1.4628	-.0146
8	.0233	1.4671	1.4557	-.0237
10	.0328	1.4534	1.4423	-.0342
12	.0413	1.4461	1.4354	-.0429
$r_n/r_b = 0.50$				
-4	-0.0042	1.4722	1.4605	0.0087
-2	.0004	1.4782	1.4674	.0026
0	.0035	1.4718	1.4616	-.0016
2	.0076	1.4716	1.4613	-.0070
4	.0118	1.4682	1.4573	-.0118
6	.0167	1.4651	1.4538	-.0174
8	.0244	1.4572	1.4457	-.0256
10	.0339	1.4450	1.4338	-.0354
12	.0442	1.4420	1.4312	-.0461



$\theta$ , deg	$r_n/r_b$	$r_b$ , cm	$l$ , cm
30	0	2.536	4.382
30	.25	2.529	3.759
30	.50	2.530	3.124
45	0	2.543	2.540
45	.25	2.531	2.281
45	.50	2.539	2.022
60	0	2.540	1.466
60	.25	2.531	1.367
60	.50	2.543	1.275
70	0	2.537	.930
70	.25	2.545	.884
70	.50	2.544	.846

(a) Cone models.

Figure 1.- Planform view and dimensions of configurations tested.



(b) Cylindrical models. (All dimensions in cm.)

Figure 1.- Concluded.

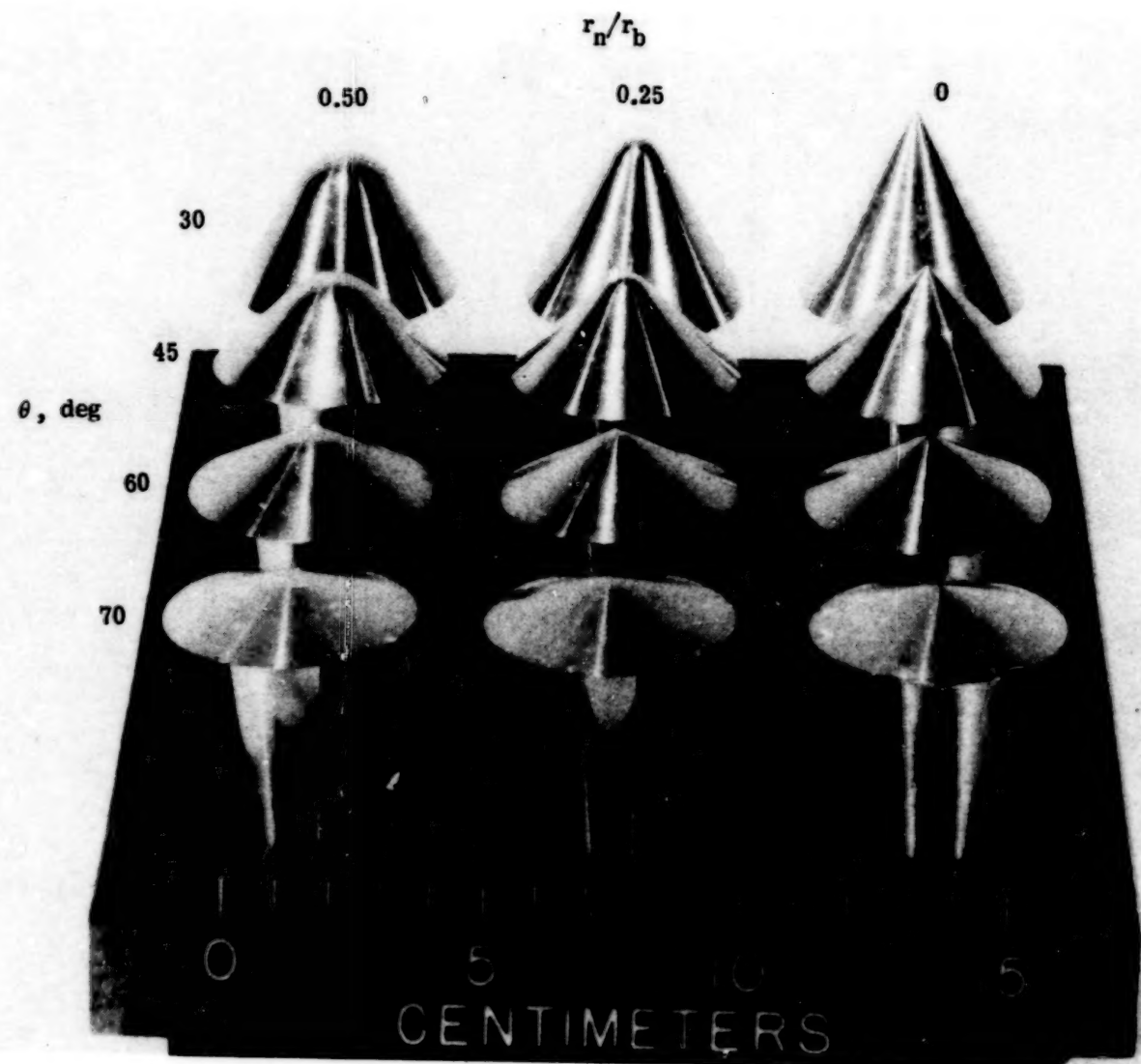


Figure 2.- Photograph of cone models tested.

L-77-3744.1

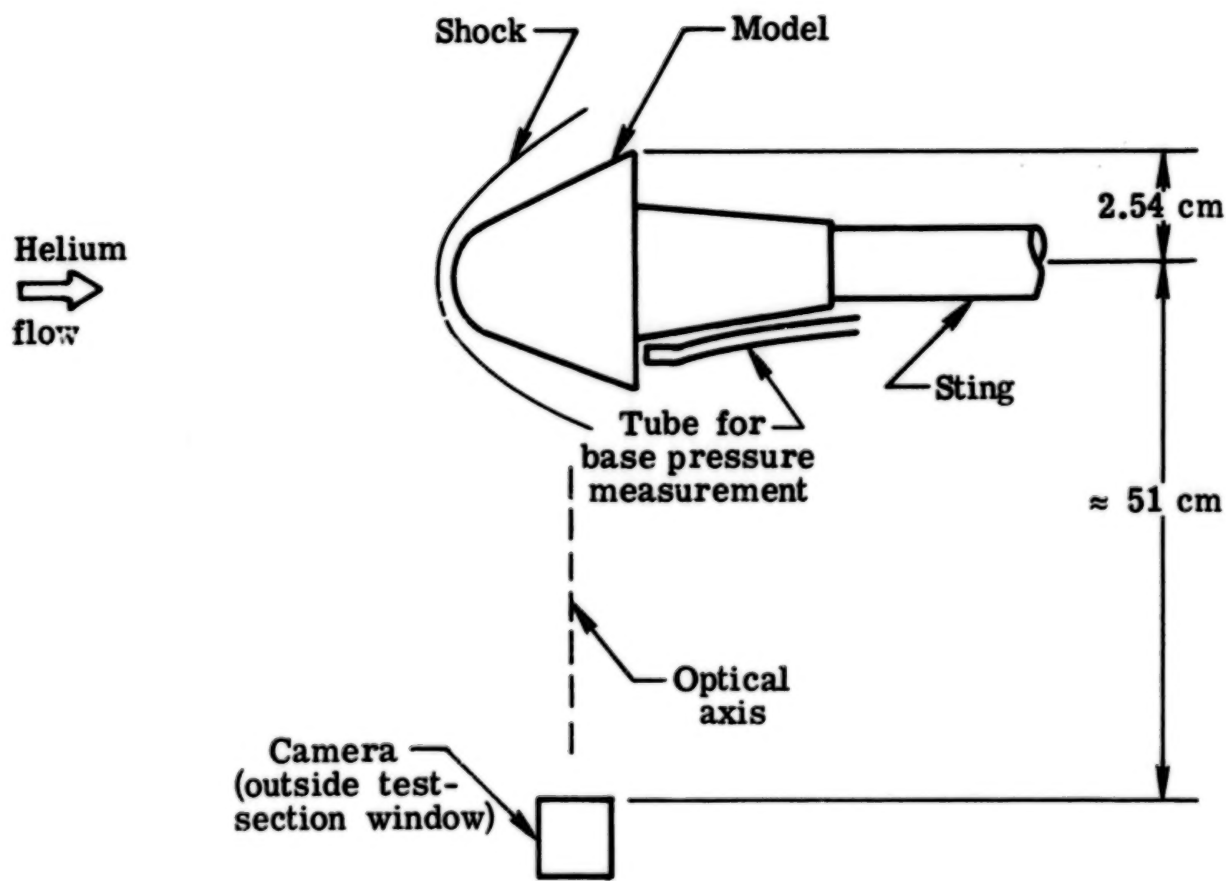


Figure 3.- Sketch of test setup.

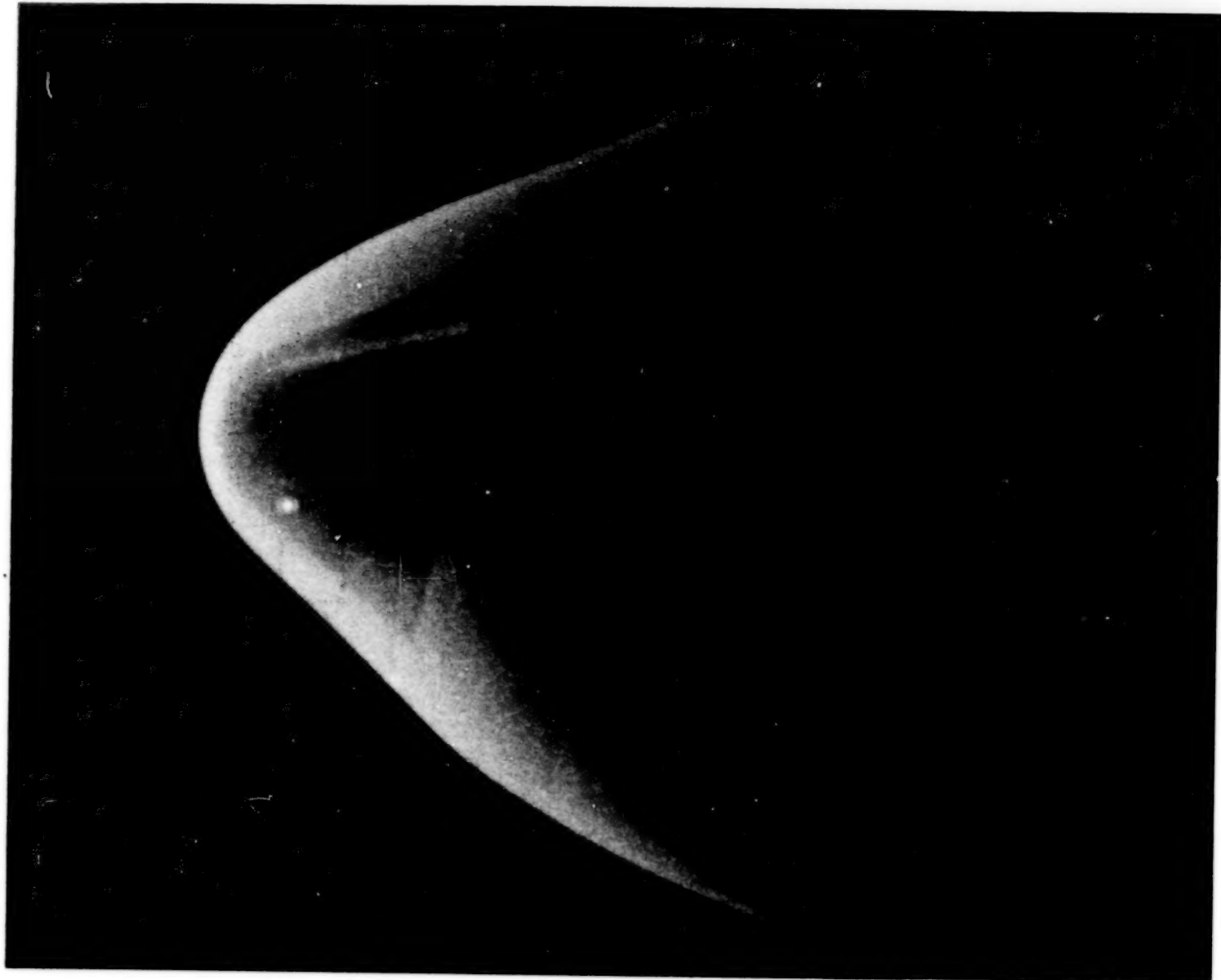


Figure 4.- Example of electron-beam photograph.

L-79-120

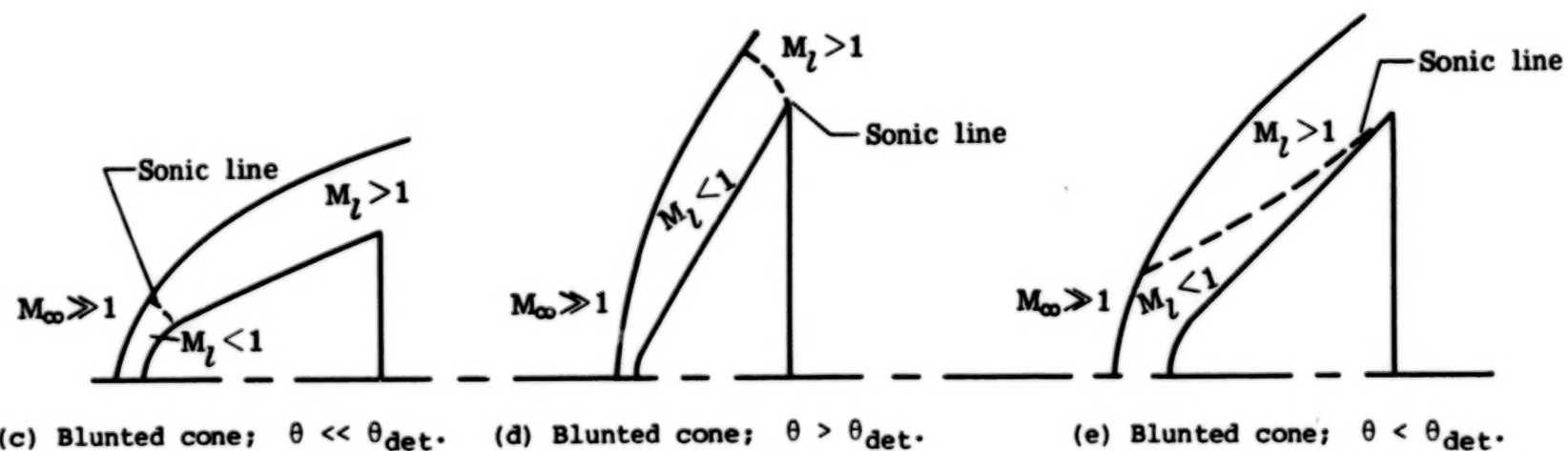
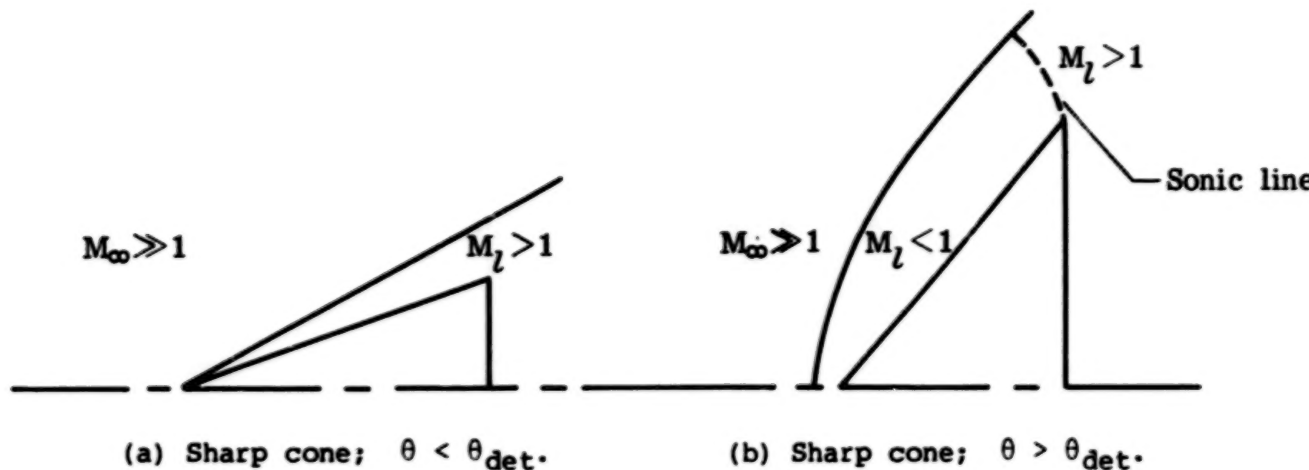
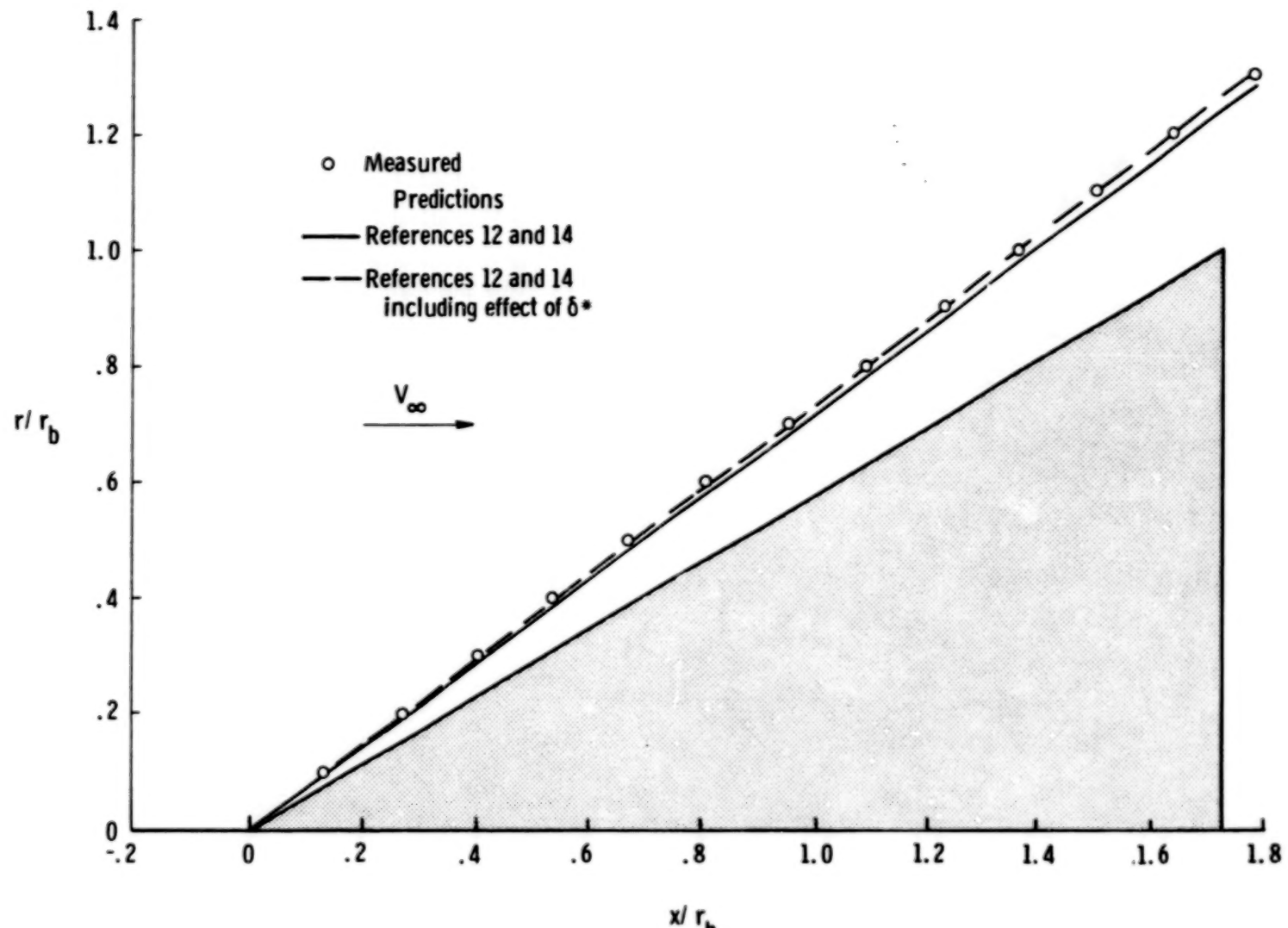
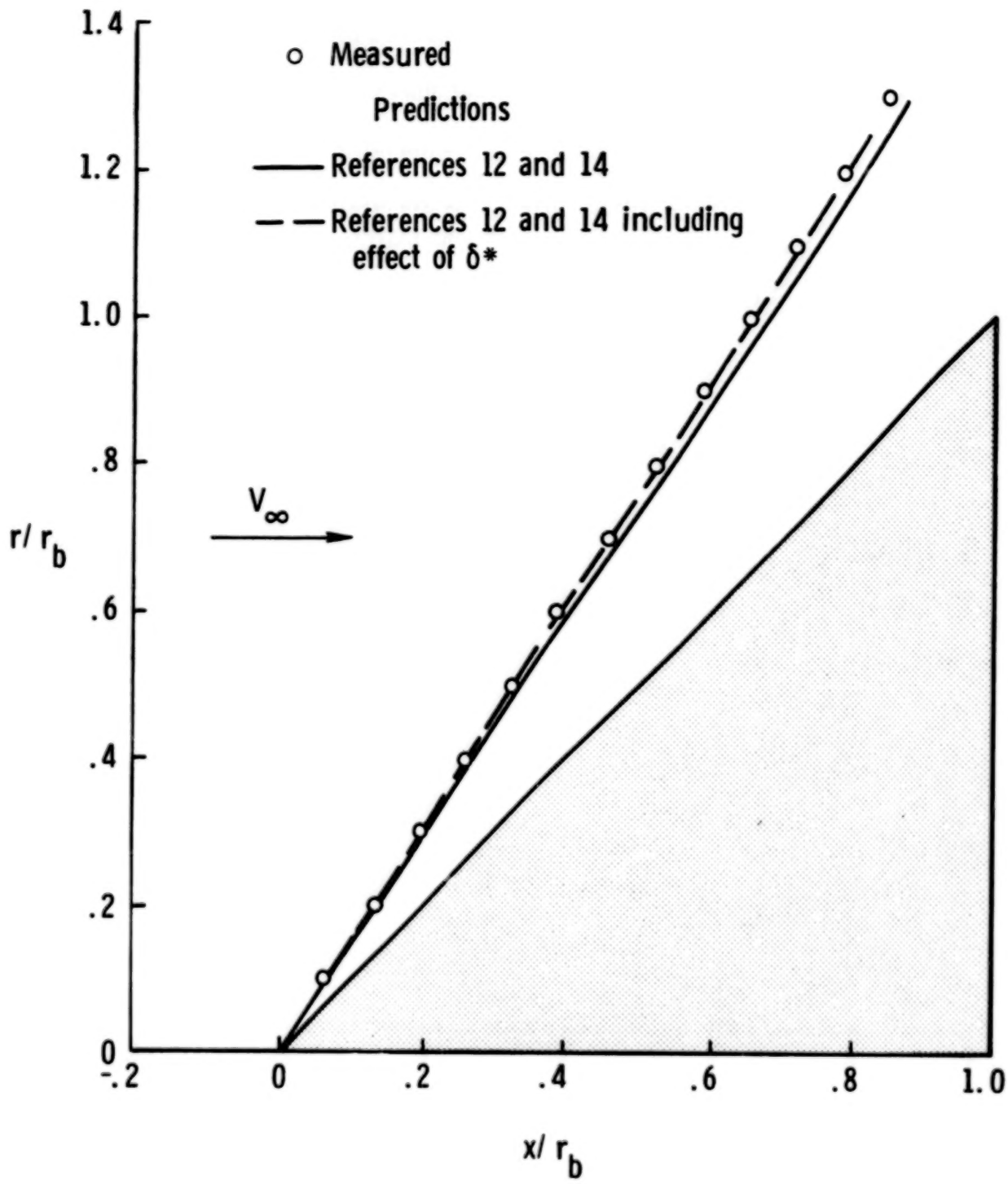


Figure 5.- Examples of local flow combinations for sharp and spherically blunted cones at  $\alpha = 0^\circ$ .



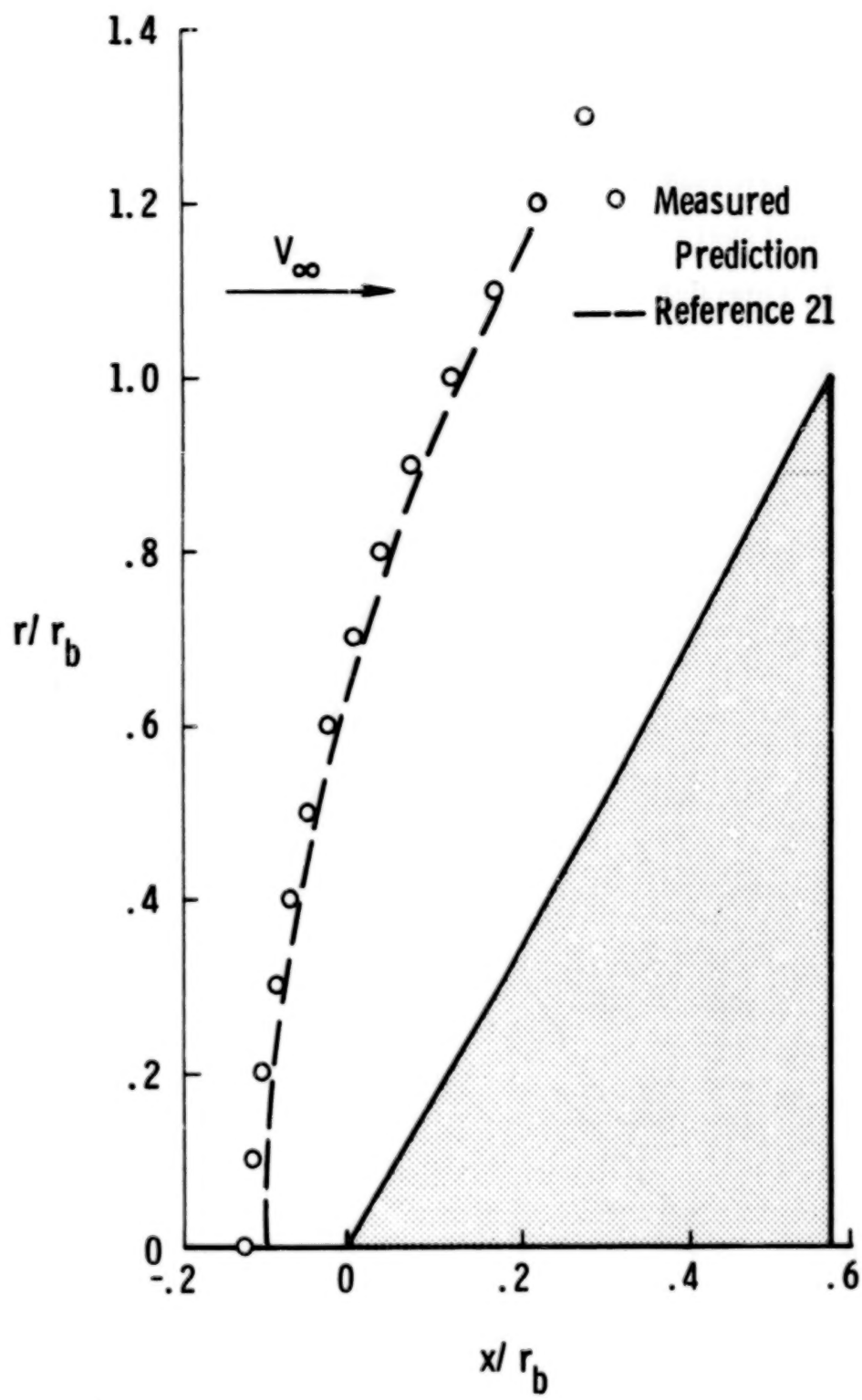
(a)  $\theta = 30^\circ$ .

Figure 6.- Measured and predicted shock shapes for sharp cones at  $\alpha = 0^\circ$ .



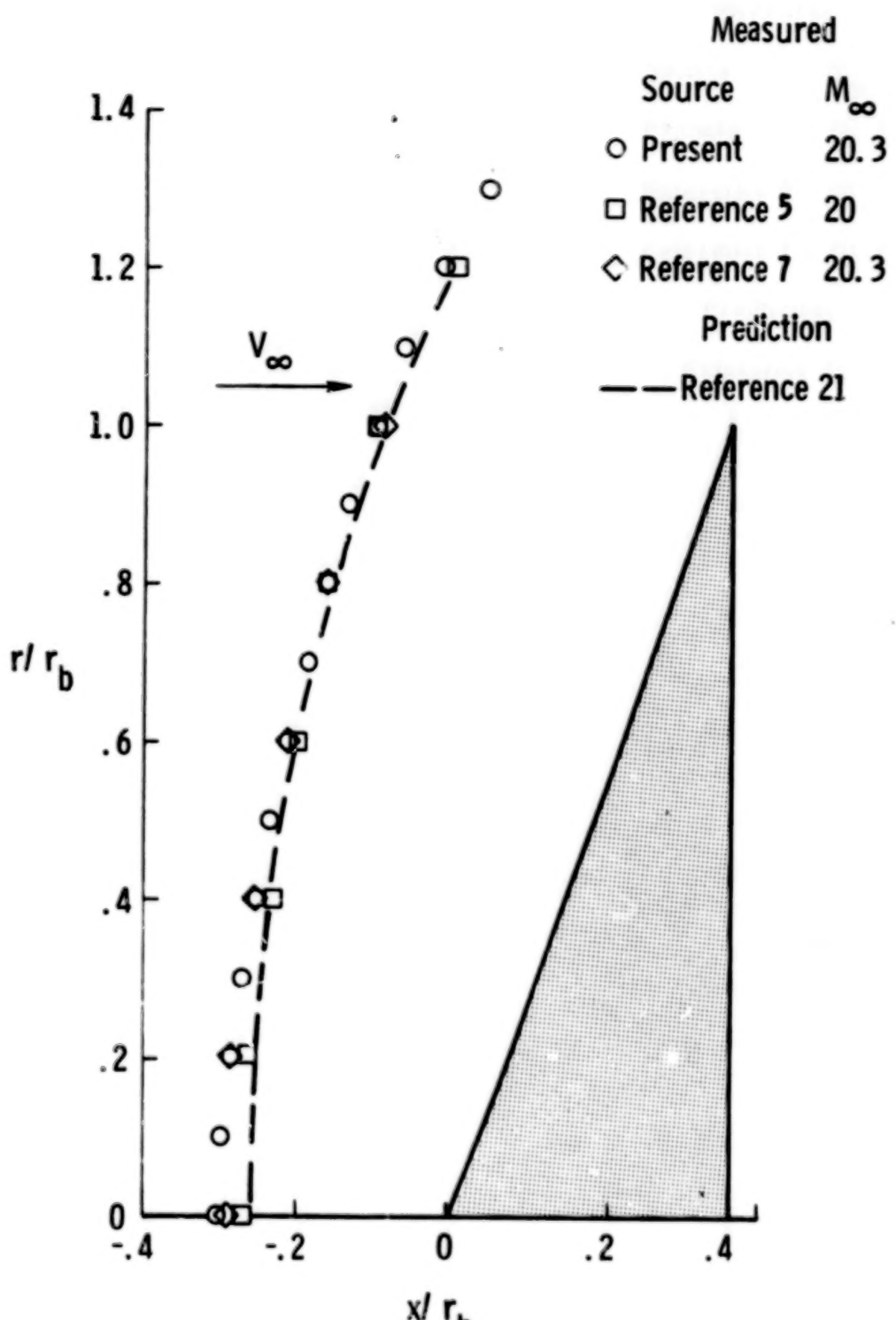
(b)  $\theta = 45^\circ$ .

Figure 6.- Continued.



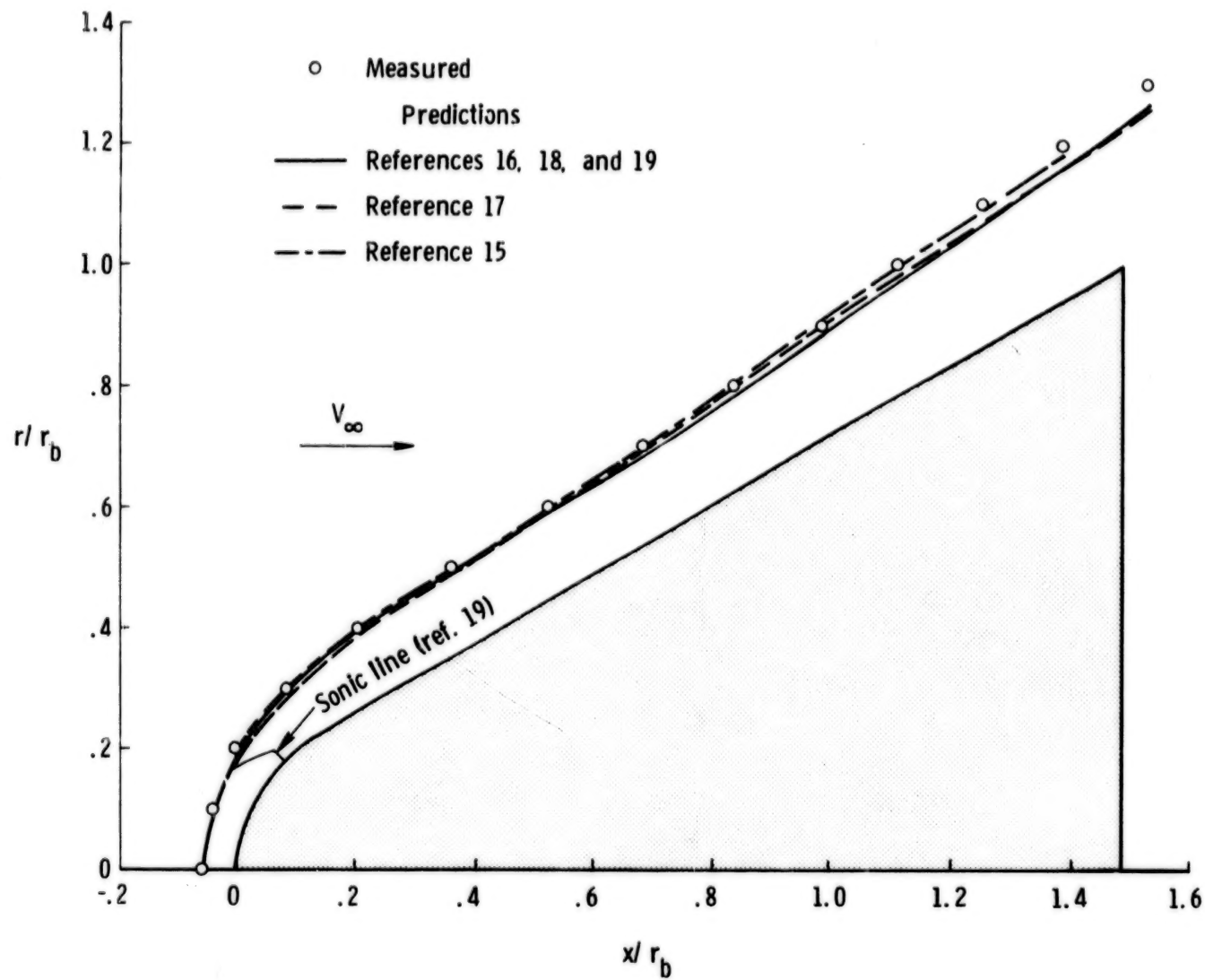
(c)  $\theta = 60^\circ$ .

Figure 6.- Continued.



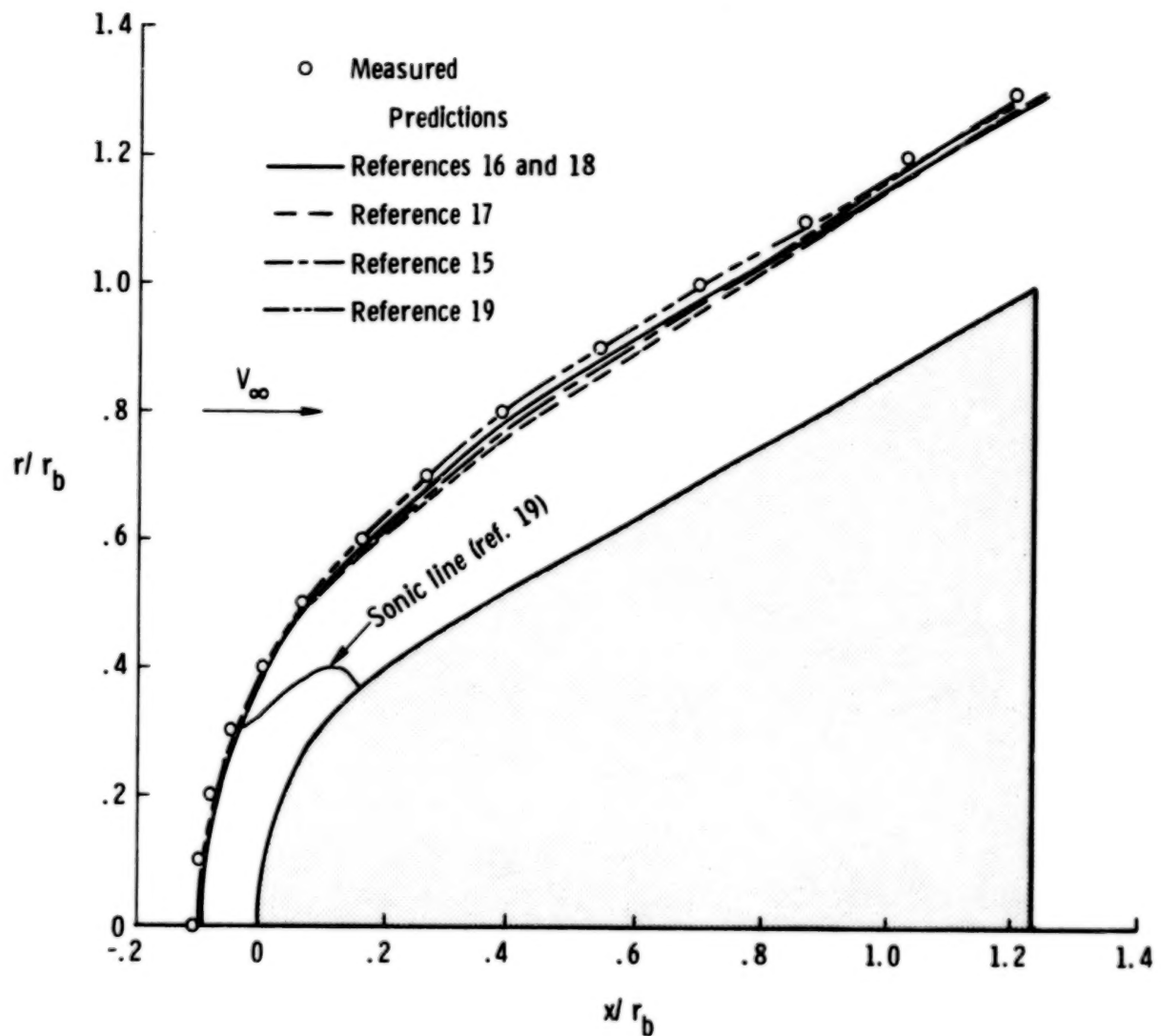
(d)  $\theta = 70^\circ$ .

Figure 6.- Concluded.



(a)  $\theta = 30^\circ$ ;  $r_n/r_b = 0.25$ .

Figure 7.- Measured and predicted shock shapes for spherically blunted cones at  $\alpha = 0^\circ$ .



(b)  $\theta = 30^\circ$ ;  $r_n/r_b = 0.50$ .

Figure 7.- Continued.

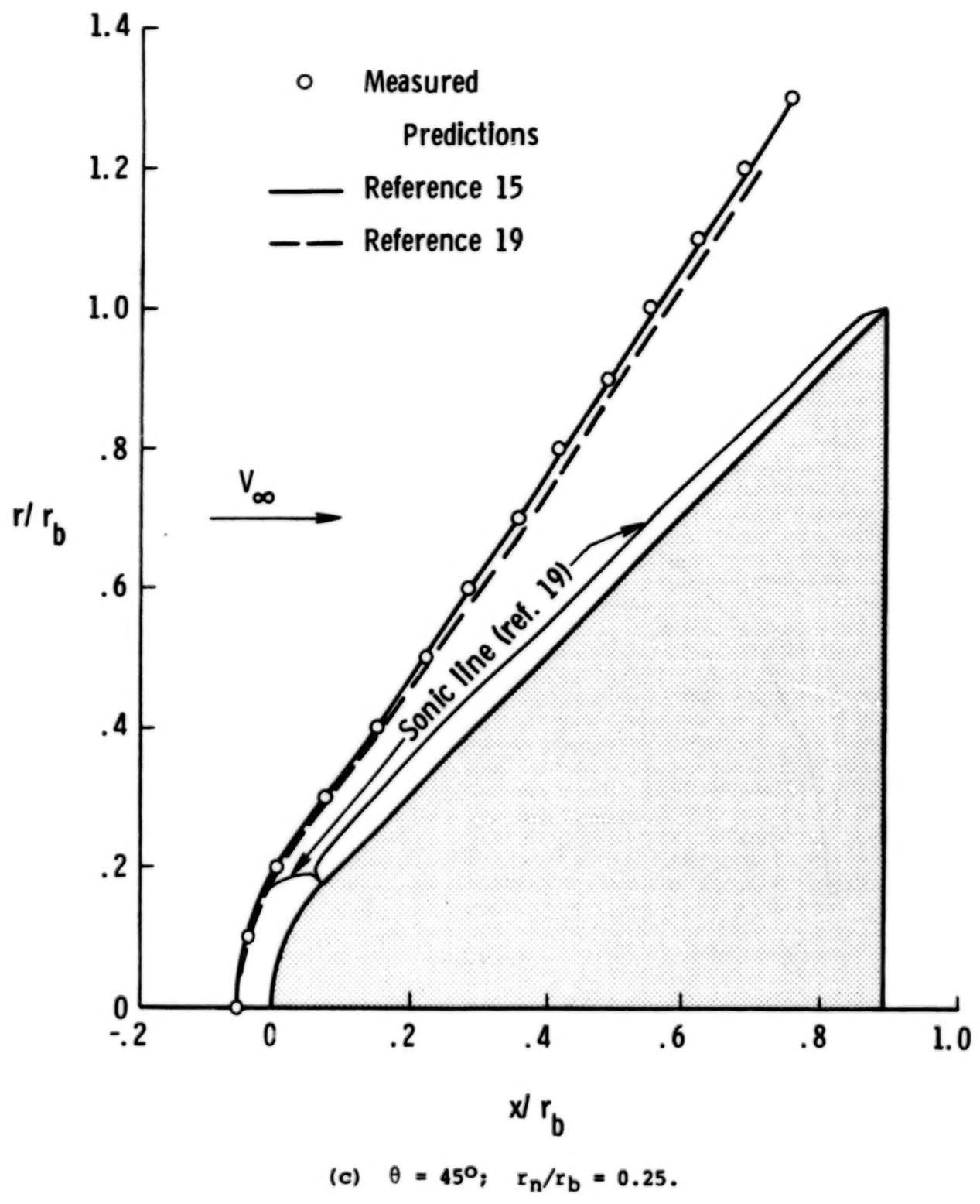
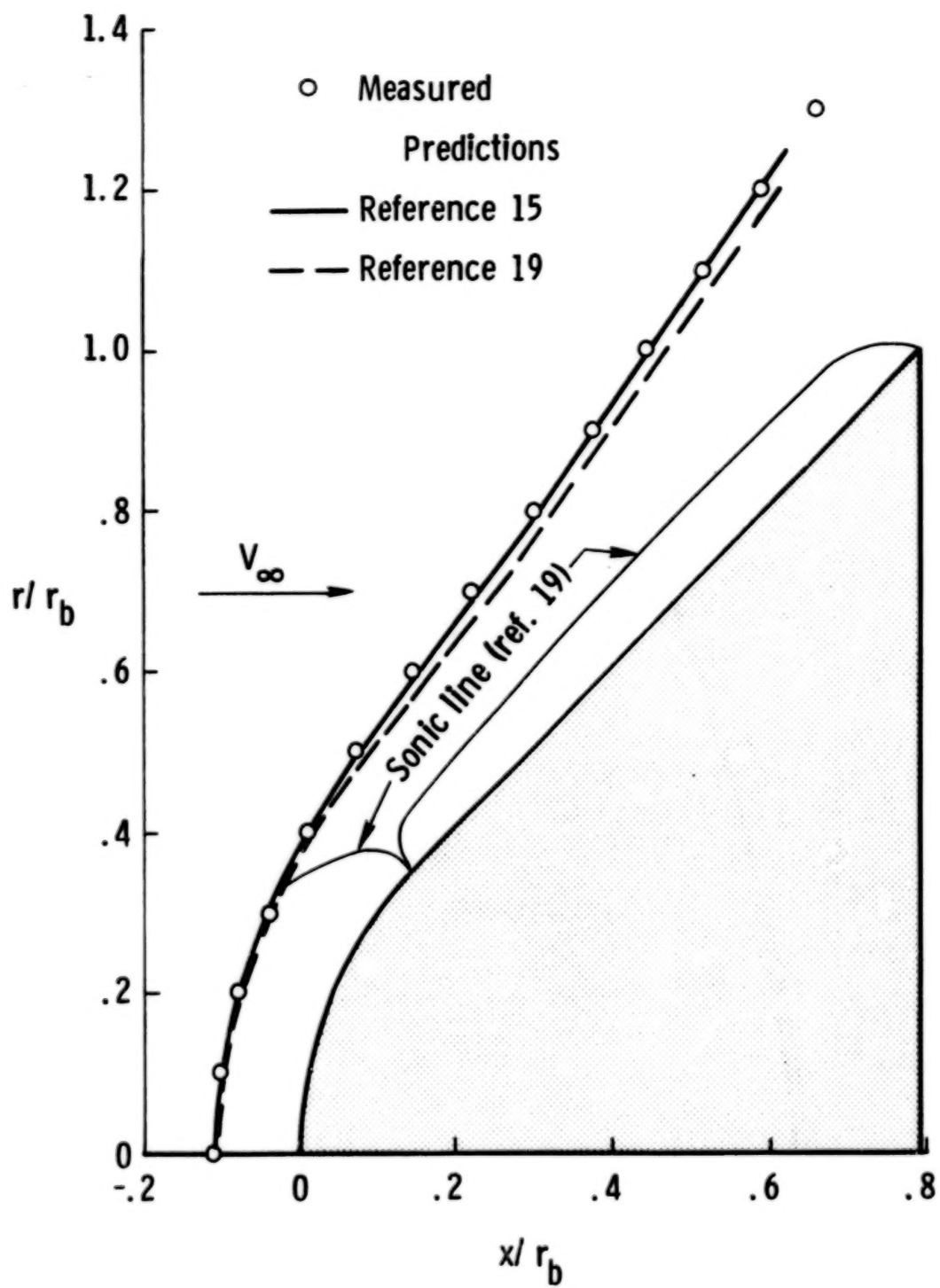
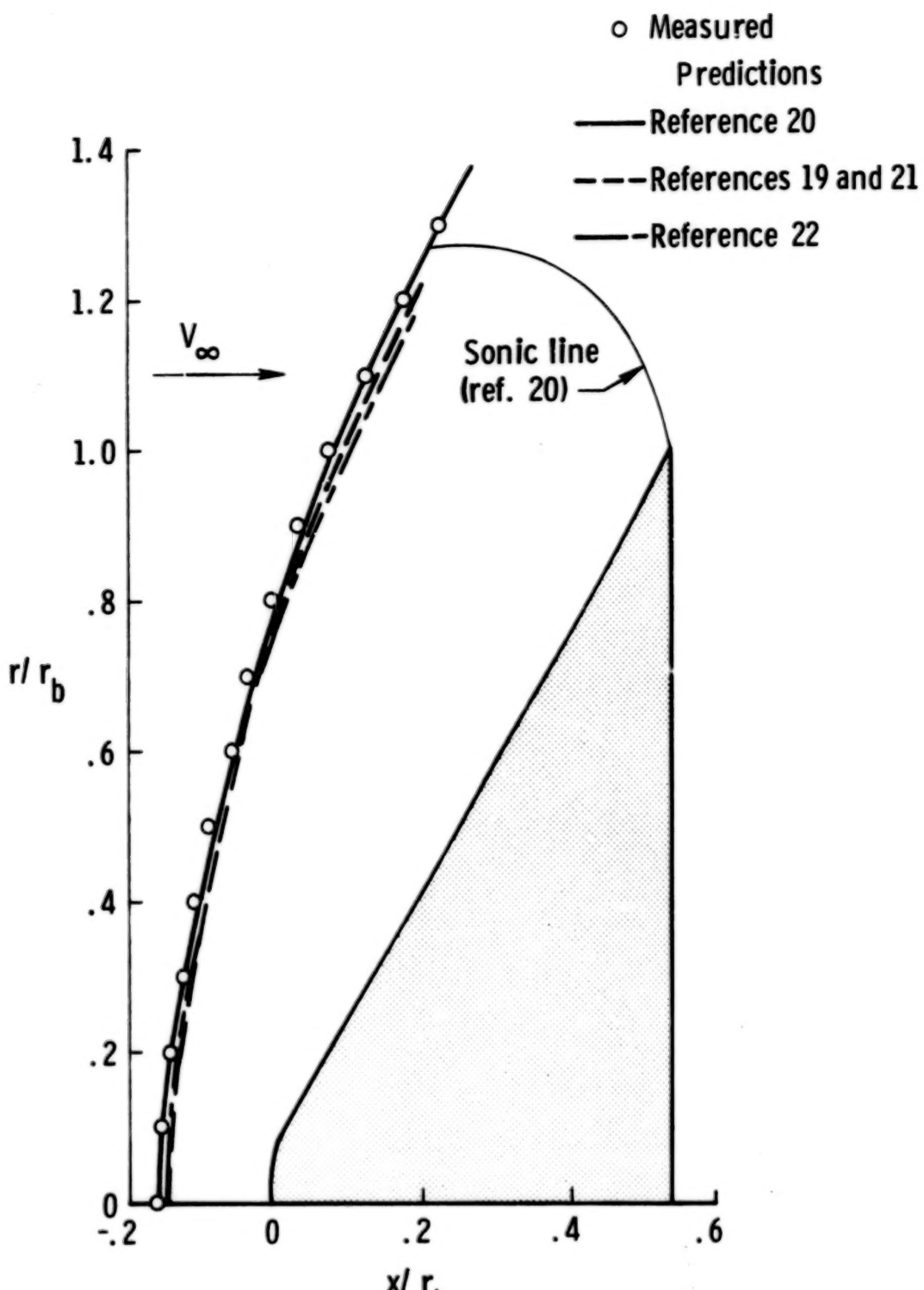


Figure 7.- Continued.



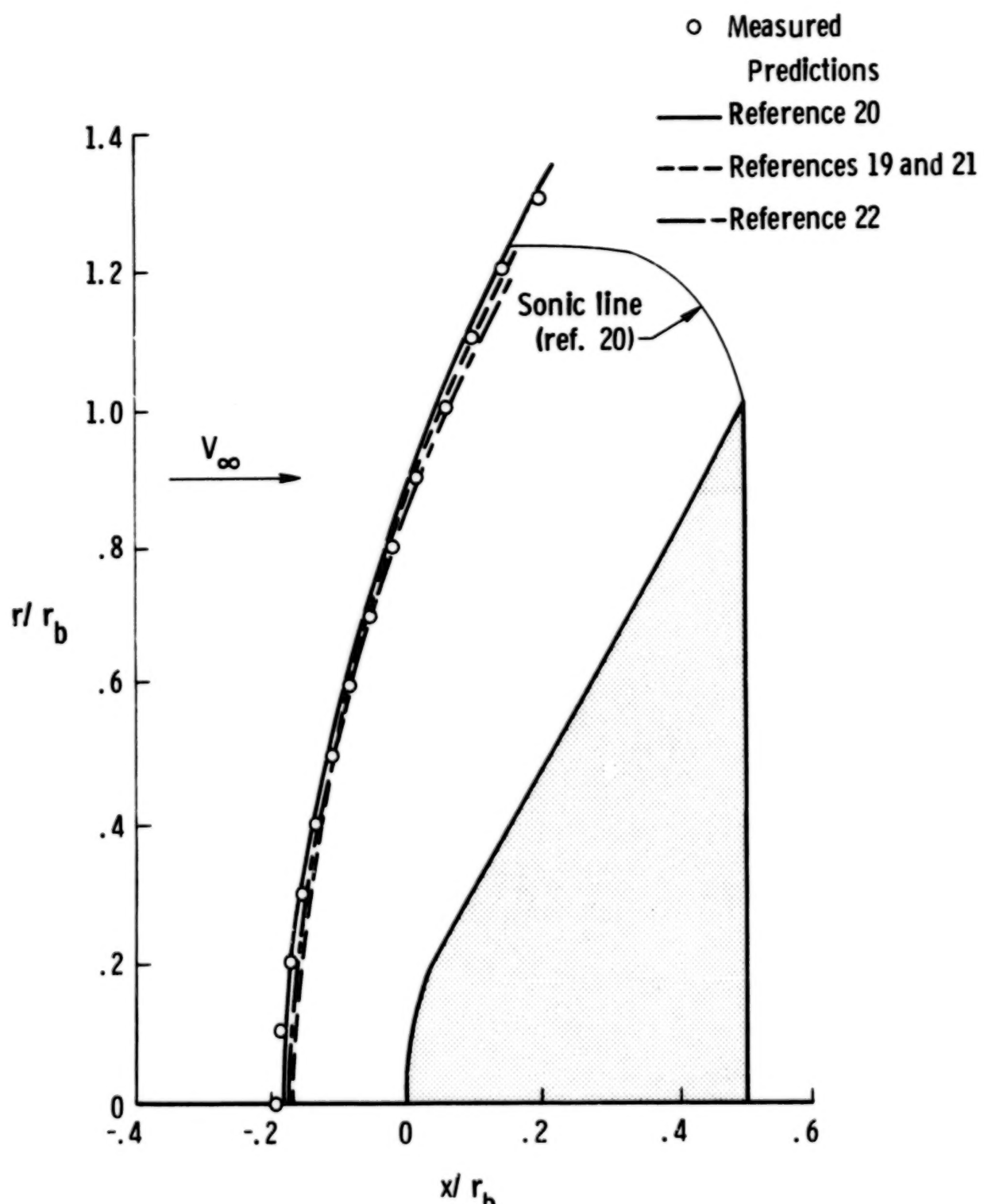
(d)  $\theta = 45^\circ$ ;  $r_n/r_b = 0.50$ .

Figure 7.- Continued.



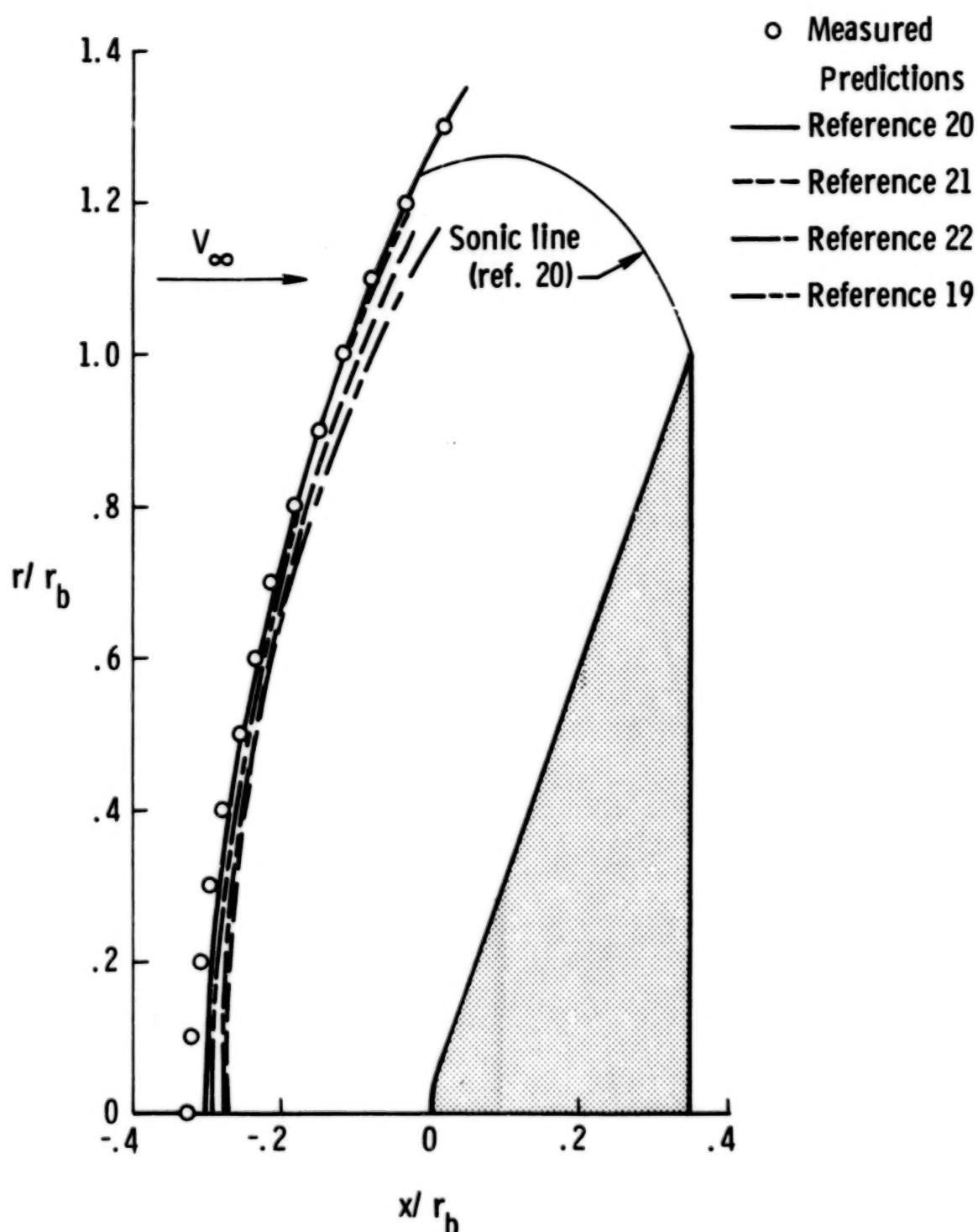
(e)  $\theta = 60^\circ$ ;  $r_n/r_b = 0.25$ .

Figure 7.- Continued.



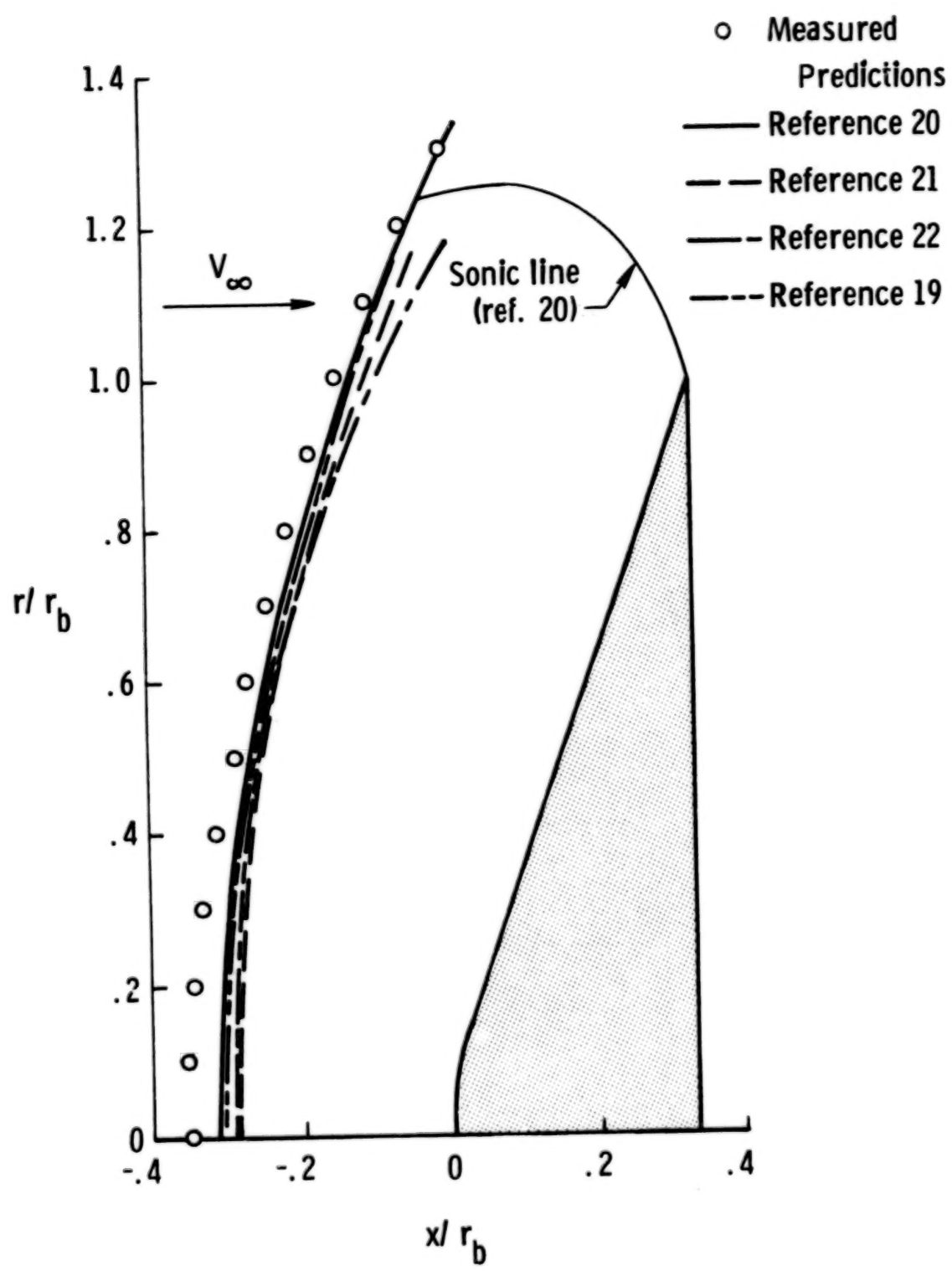
(f)  $\theta = 60^\circ$ ;  $r_n/r_b = 0.50$ .

Figure 7.- Continued.



(g)  $\theta = 70^\circ$ ;  $r_n/r_b = 0.25$ .

Figure 7.- Continued.



(h)  $\theta = 70^\circ$ ;  $r_n/r_b = 0.50$ .

Figure 7.- Concluded.

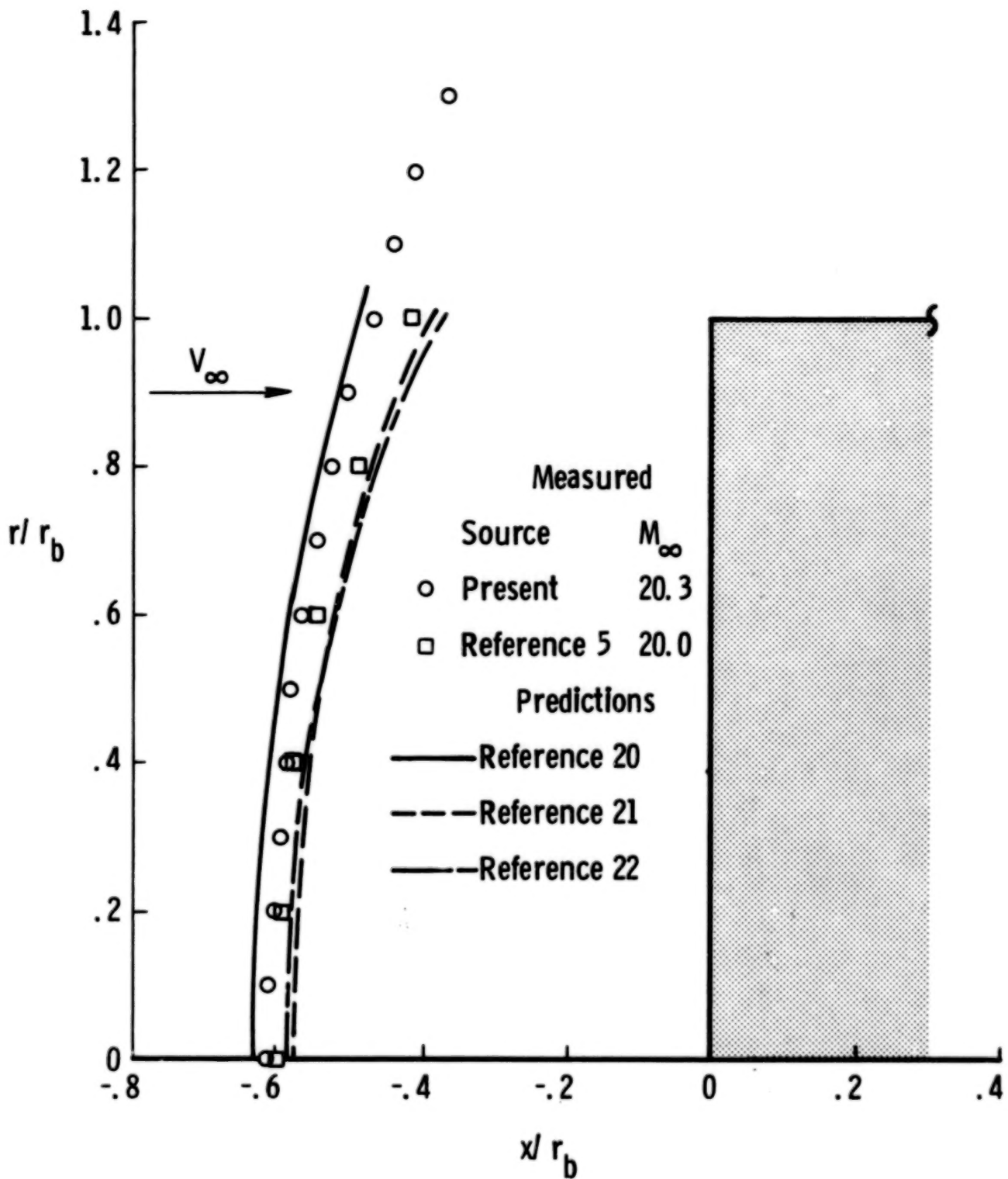


Figure 8.- Measured and predicted shock shapes for a flat-faced cylinder ( $\theta = 90^\circ$ ) at  $\alpha = 0^\circ$ .

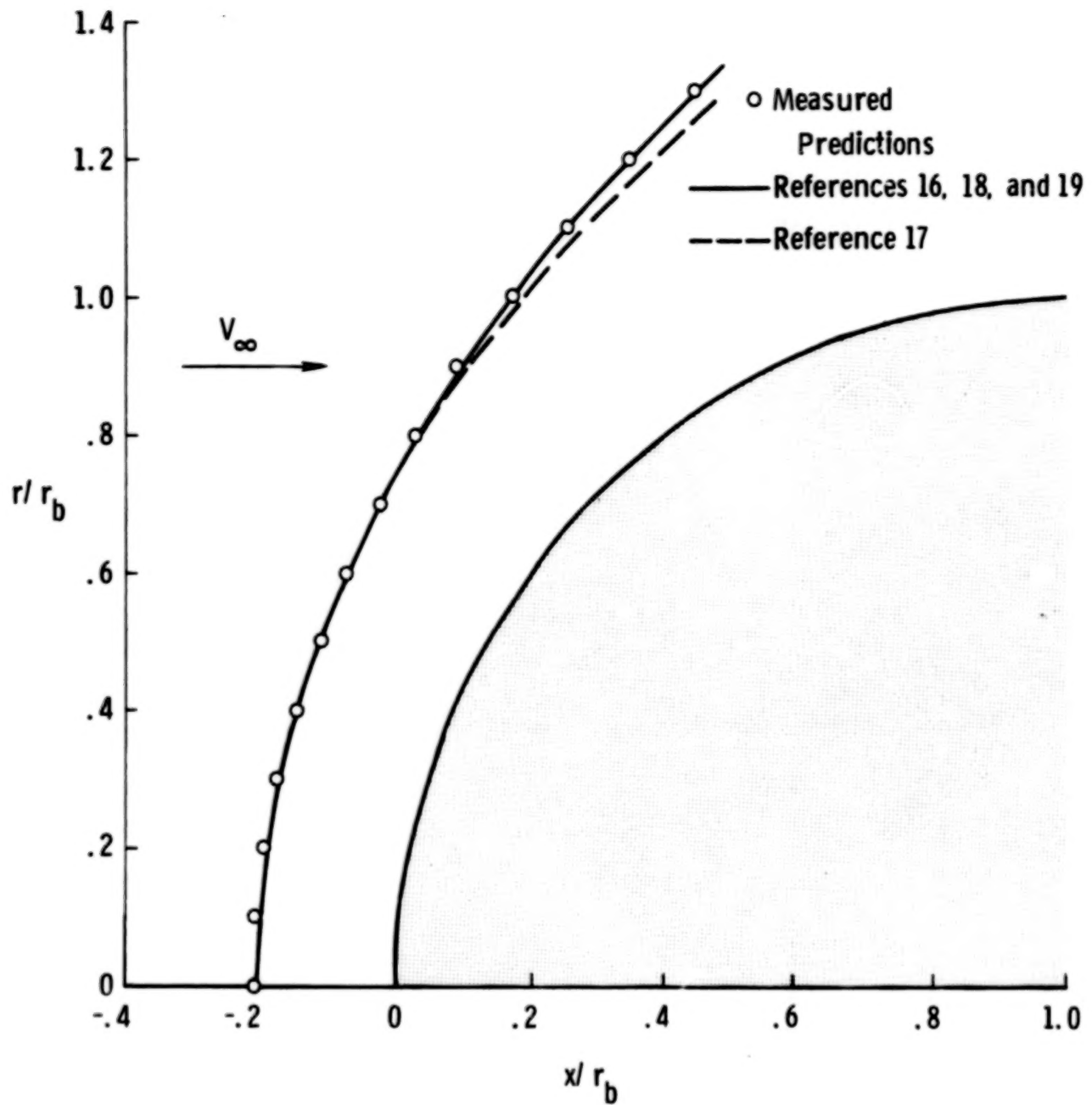
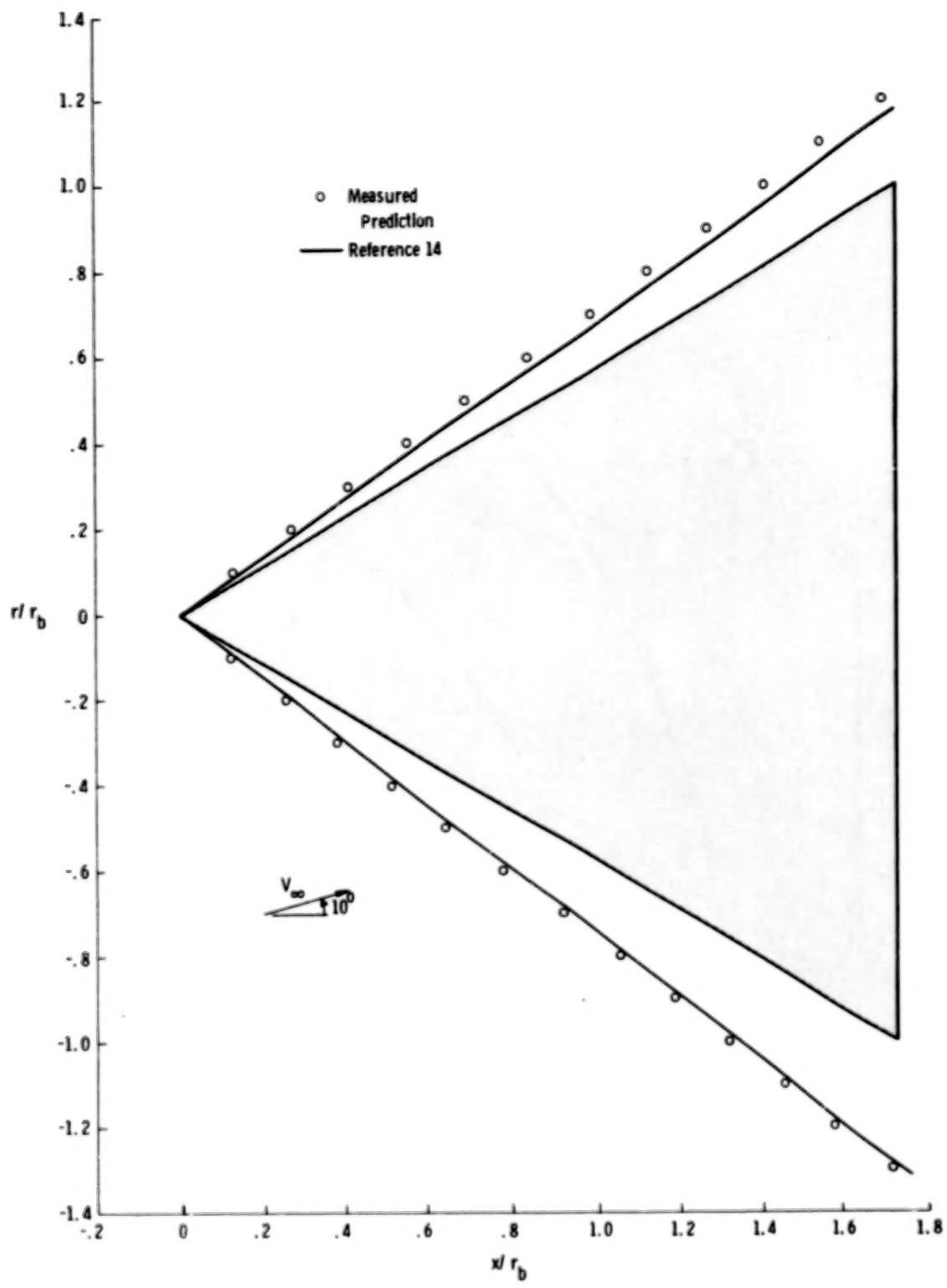
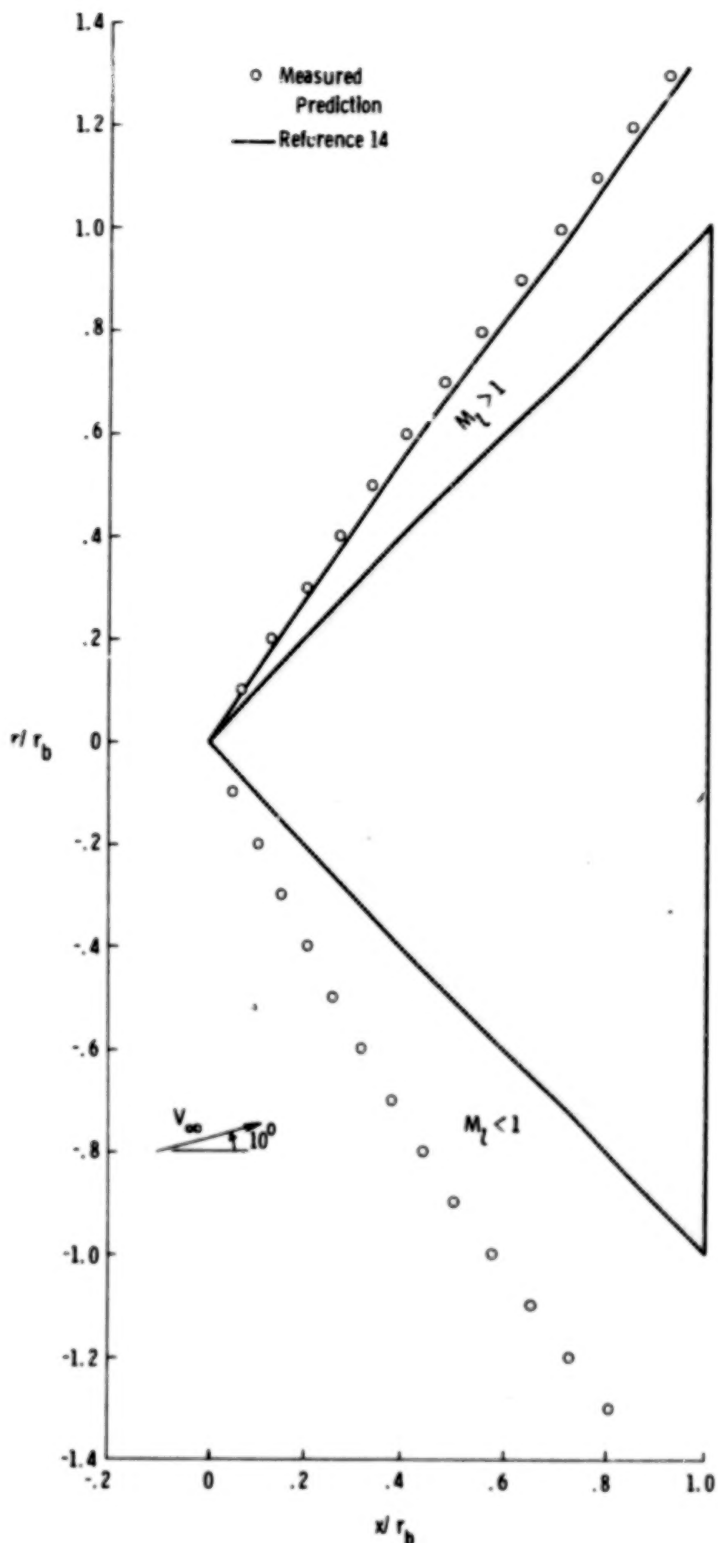


Figure 9.- Measured and predicted shock shapes for a hemispherically blunted cylinder (sphere) at  $\alpha = 0^\circ$ .



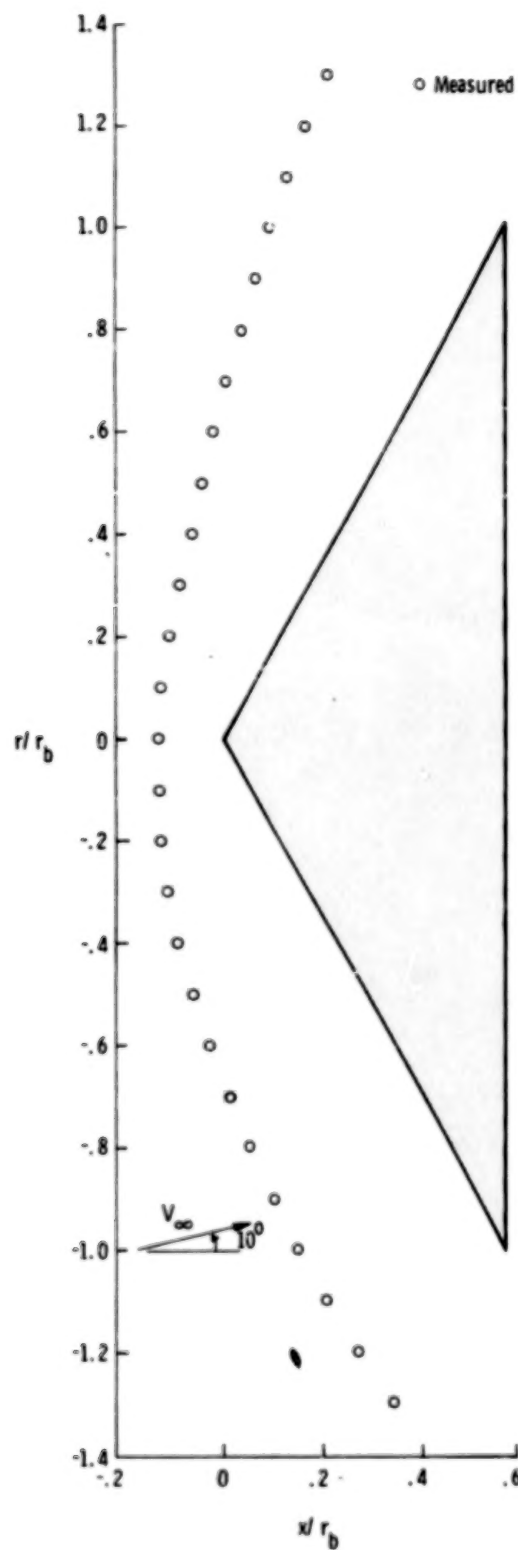
(a)  $\theta = 30^\circ$ .

Figure 10.- Measured and predicted shock shapes for sharp cones at  $\alpha = 10^\circ$ .



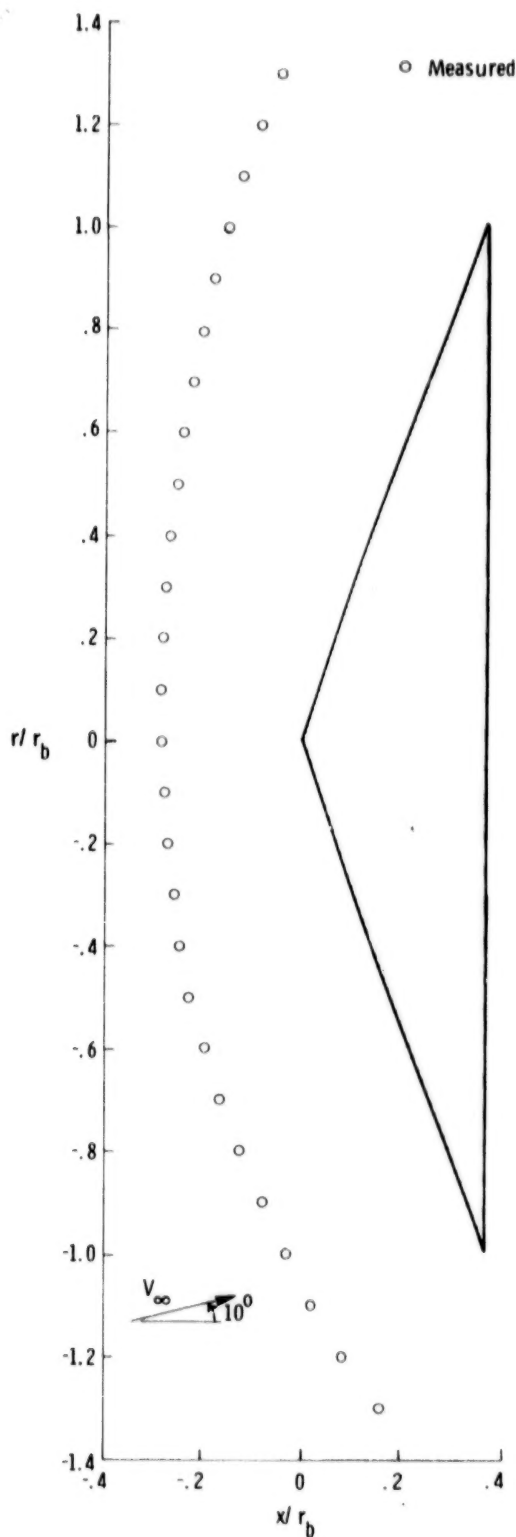
(b)  $\theta = 45^\circ$ .

Figure 10.- Concluded.



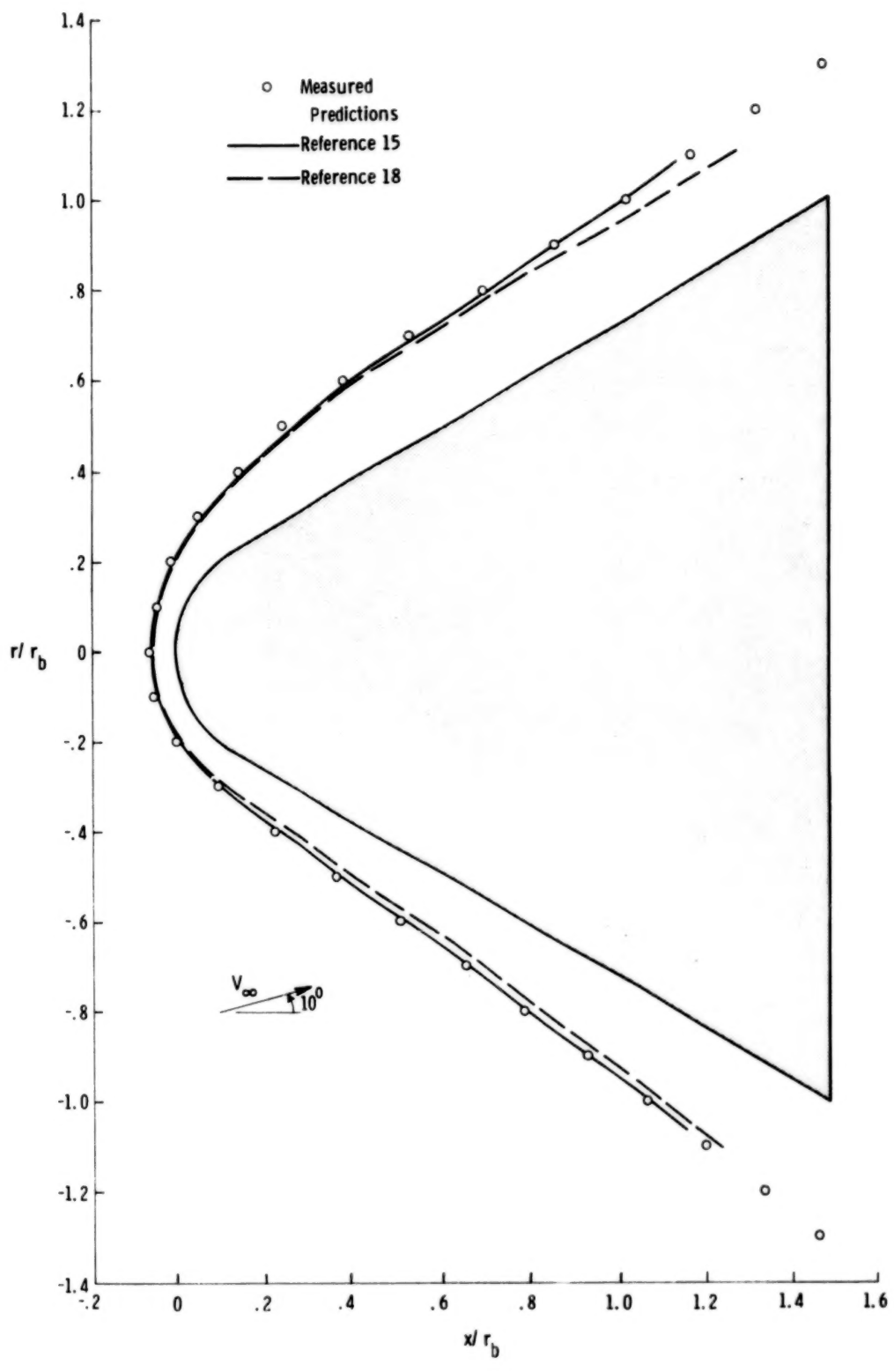
(a)  $\theta = 60^\circ$ .

Figure 11.- Measured shock shapes for sharp cones at  $\alpha = 10^\circ$ .



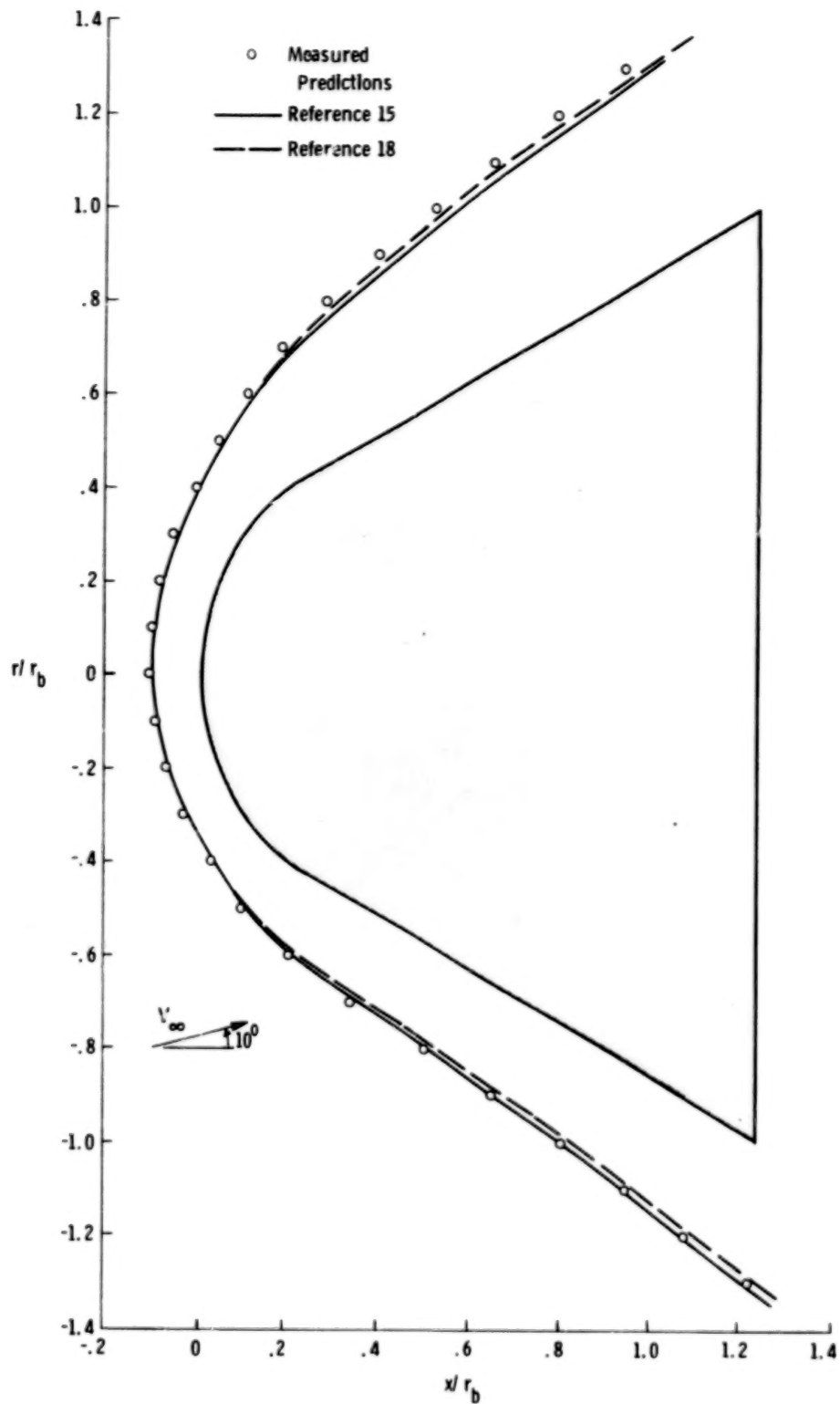
(b)  $\theta = 70^\circ$ .

**Figure 11.- Concluded.**



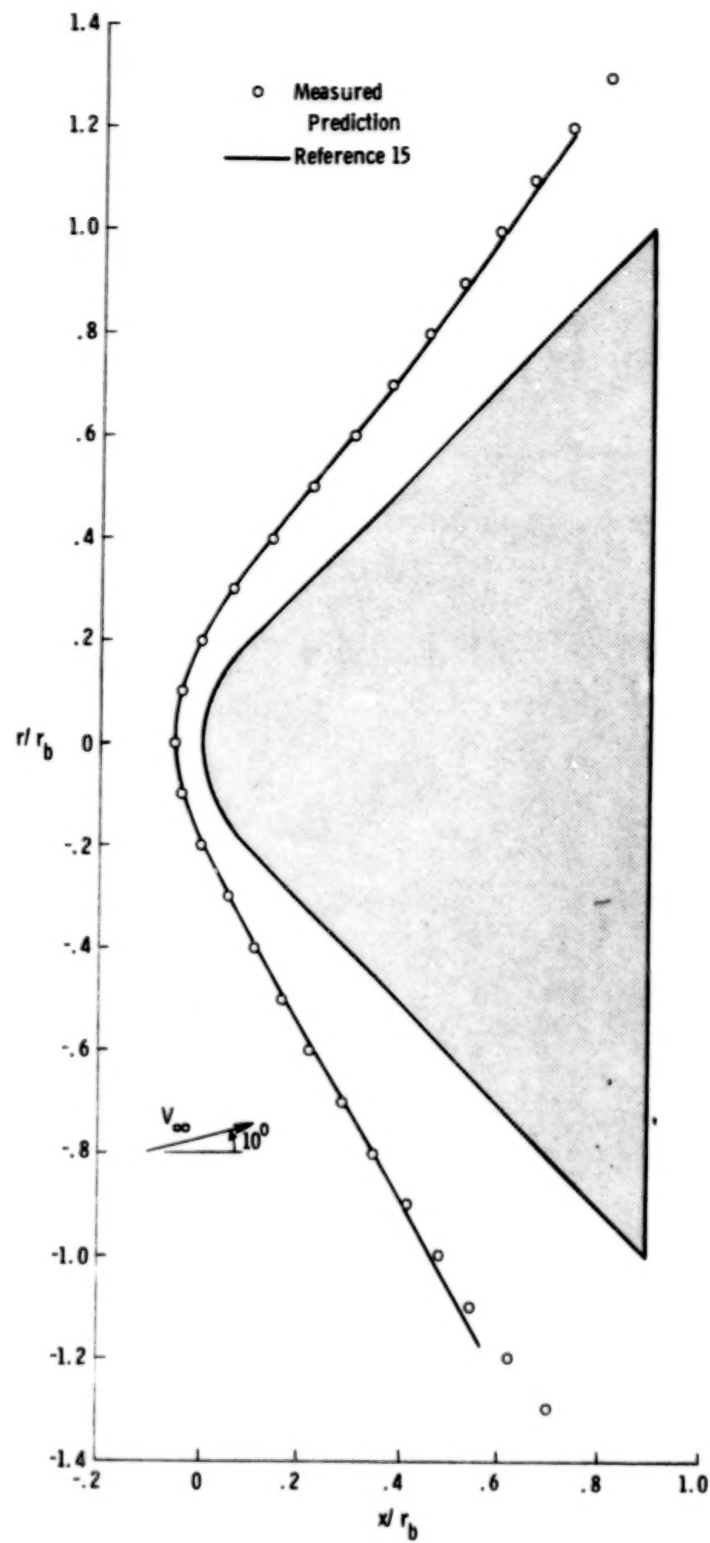
(a)  $\theta = 30^\circ$ ;  $r_n/r_b = 0.25$ .

**Figure 12.-** Measured and predicted shock shapes for spherically blunted cones at  $\alpha = 10^\circ$ .



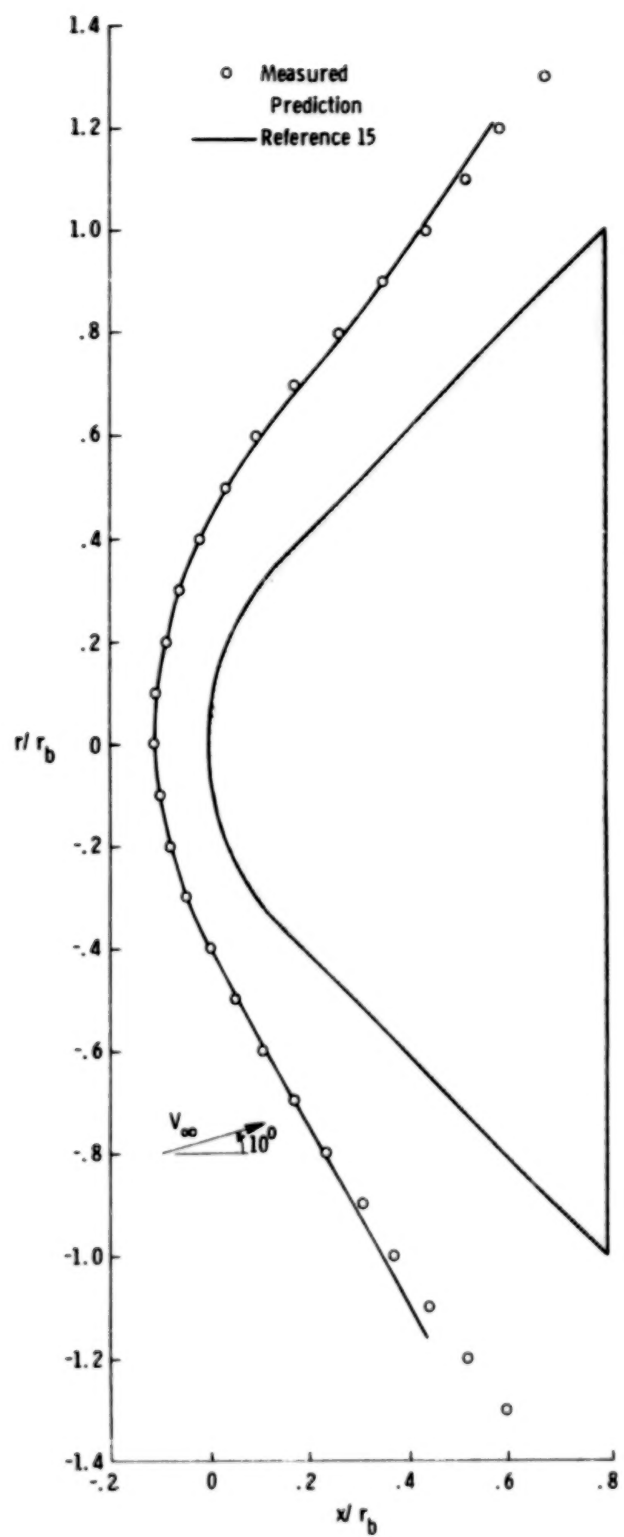
(b)  $\theta = 30^\circ$ ;  $r_n/r_b = 0.50$ .

Figure 12.- Continued.



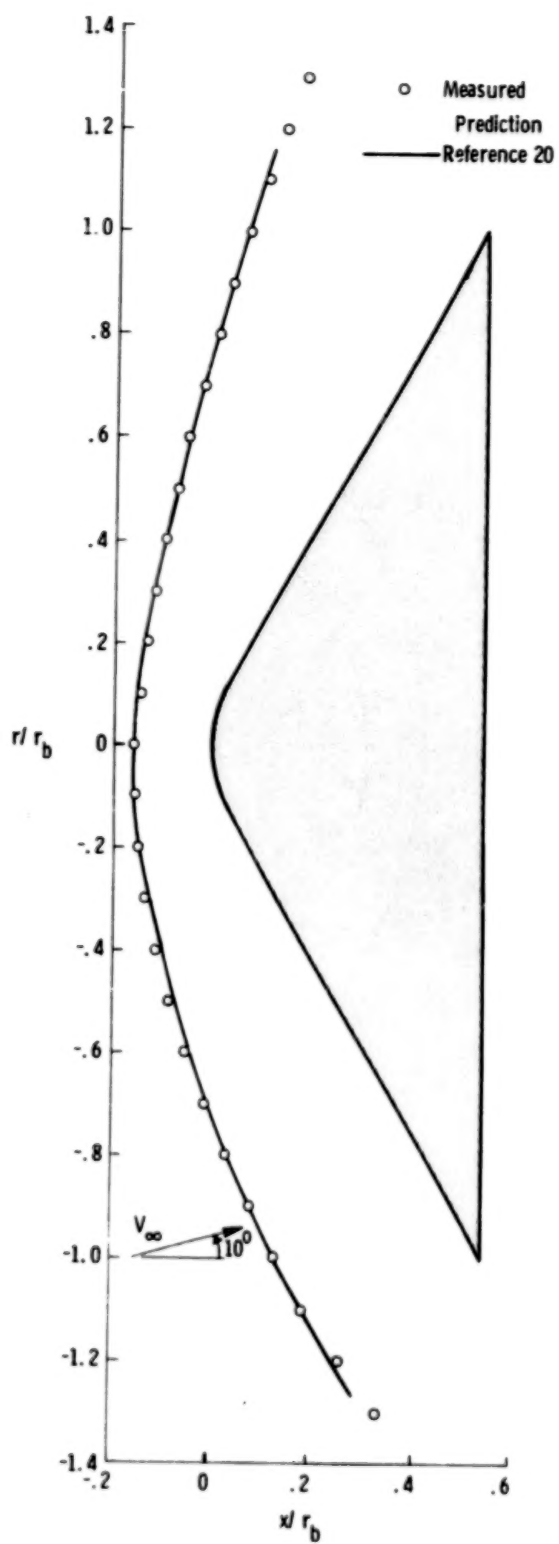
(c)  $\theta = 45^\circ$ ;  $r_n/r_b = 0.25$ .

Figure 12.- Continued.



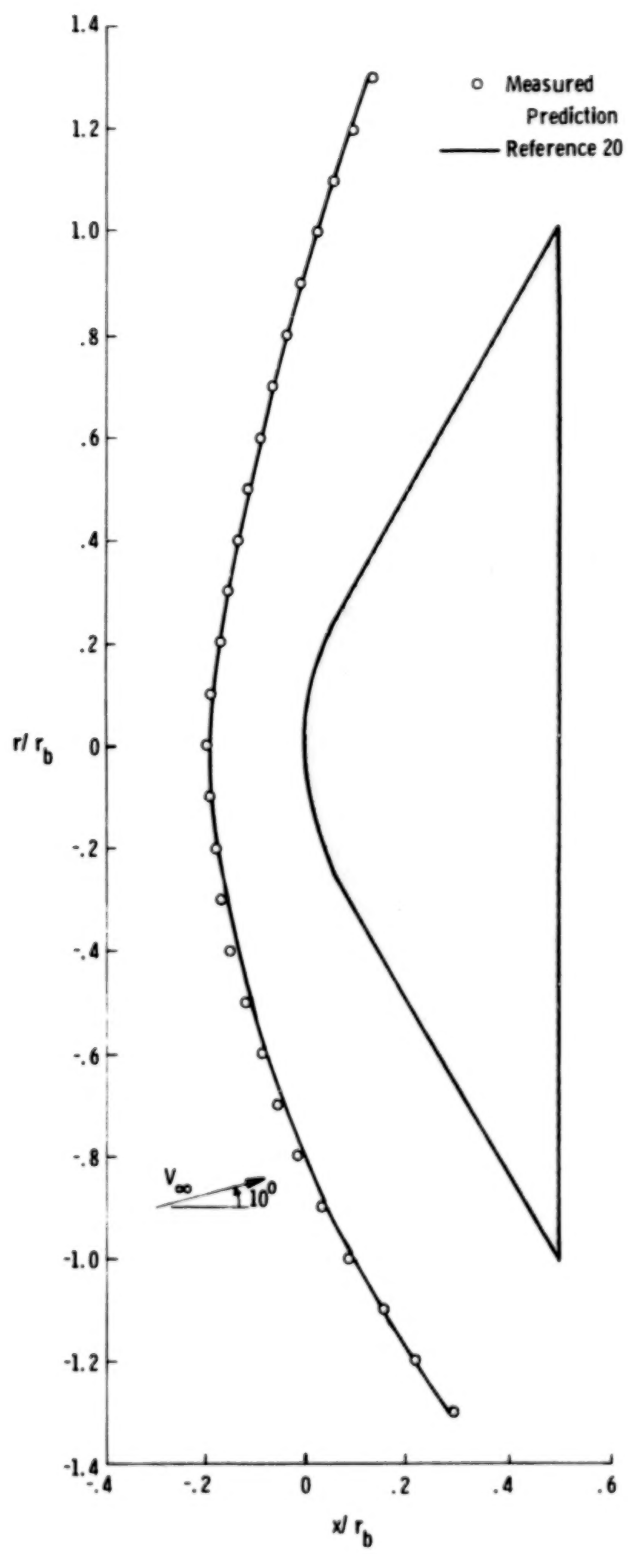
(d)  $\theta = 45^\circ$ ;  $r_n/r_b = 0.50$ .

Figure 12.- Continued.



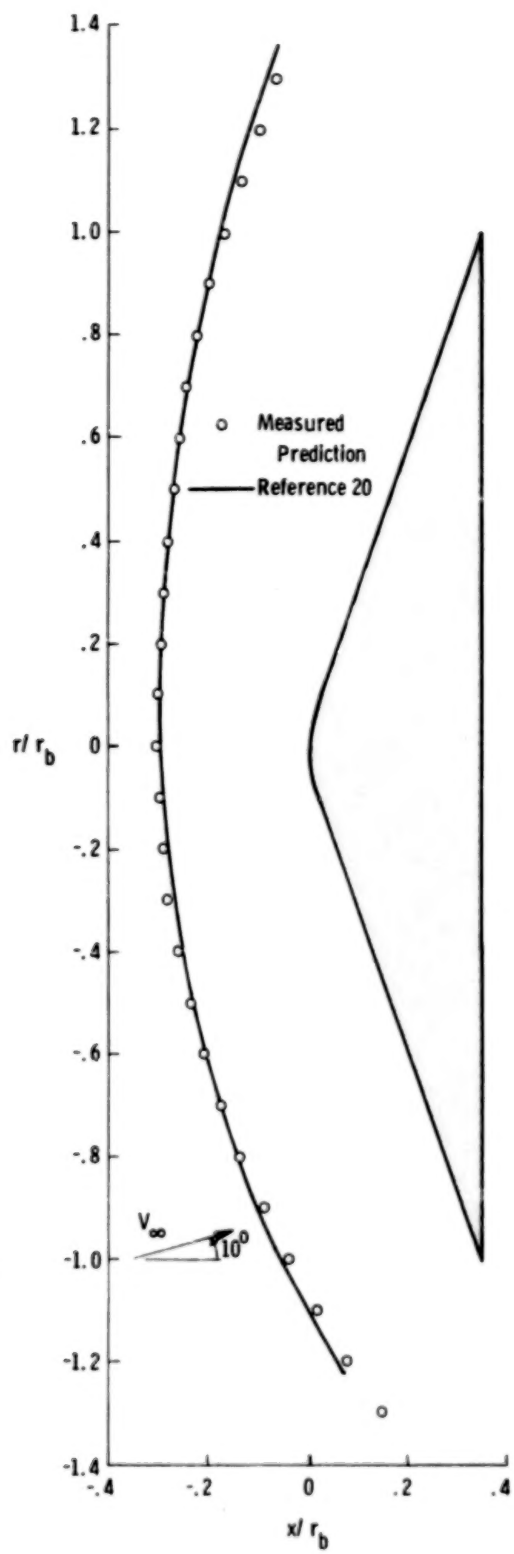
(e)  $\theta = 60^\circ$ ;  $r_n/r_b = 0.25$ .

Figure 12.- Continued.



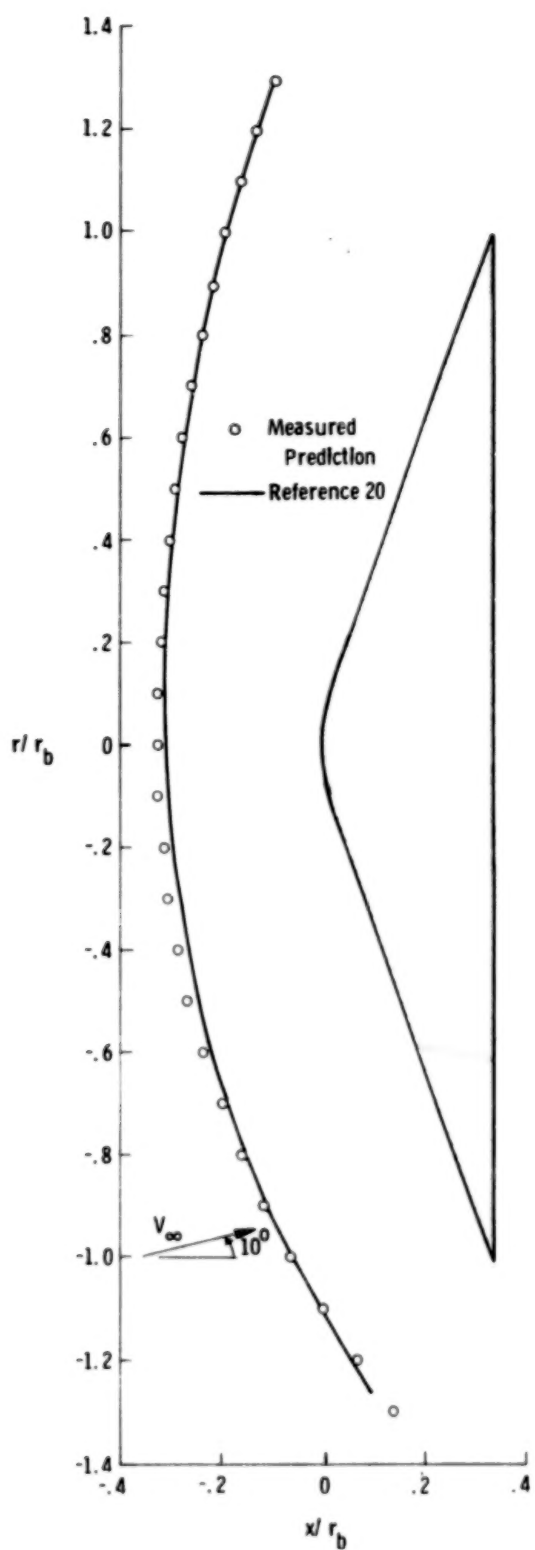
(f)  $\theta = 60^\circ$ ;  $r_n/r_b = 0.50$ .

Figure 12.- Continued.



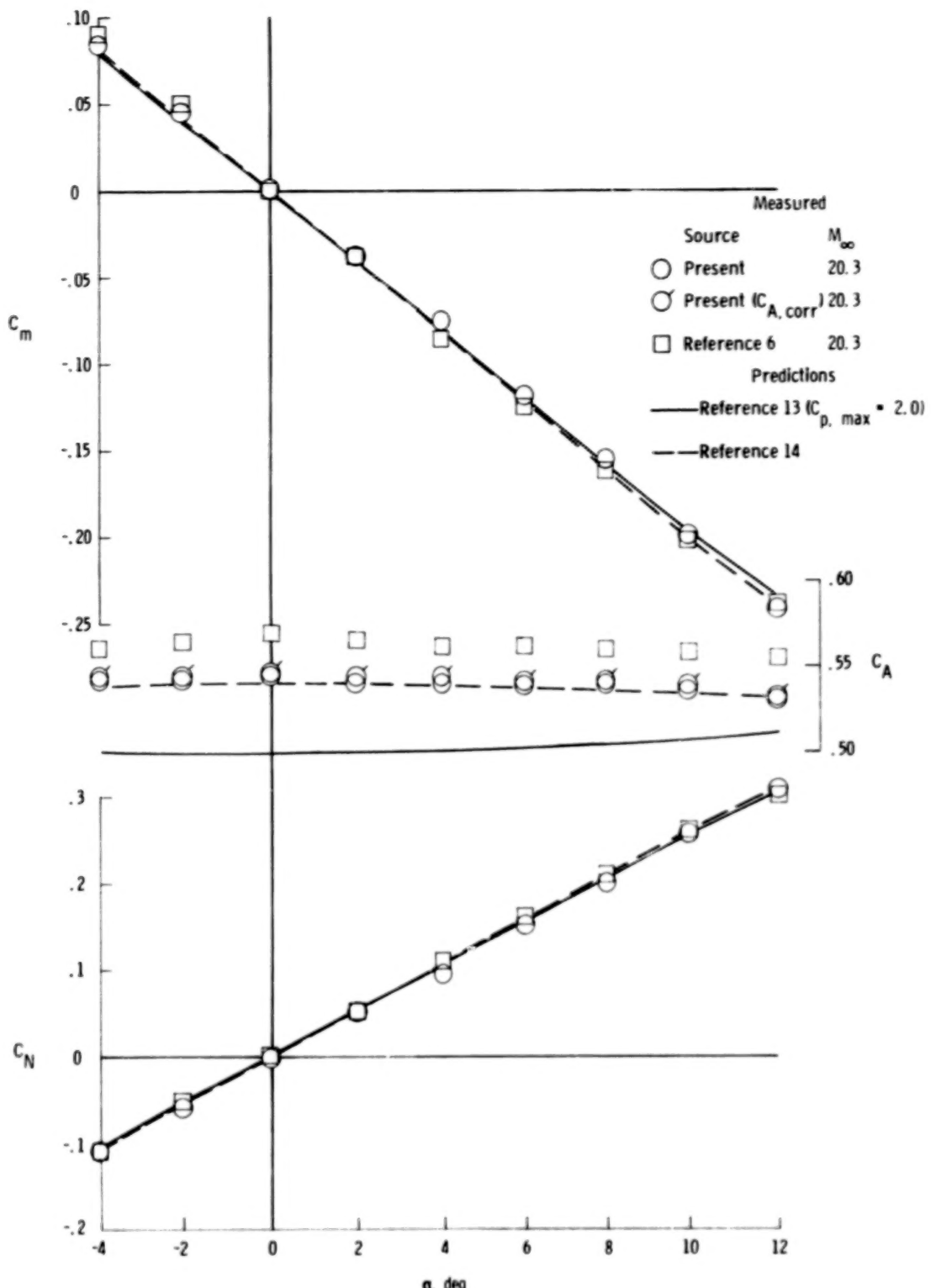
(g)  $\theta = 70^\circ$ ;  $r_n/r_b = 0.25$ .

Figure 12.- Continued.



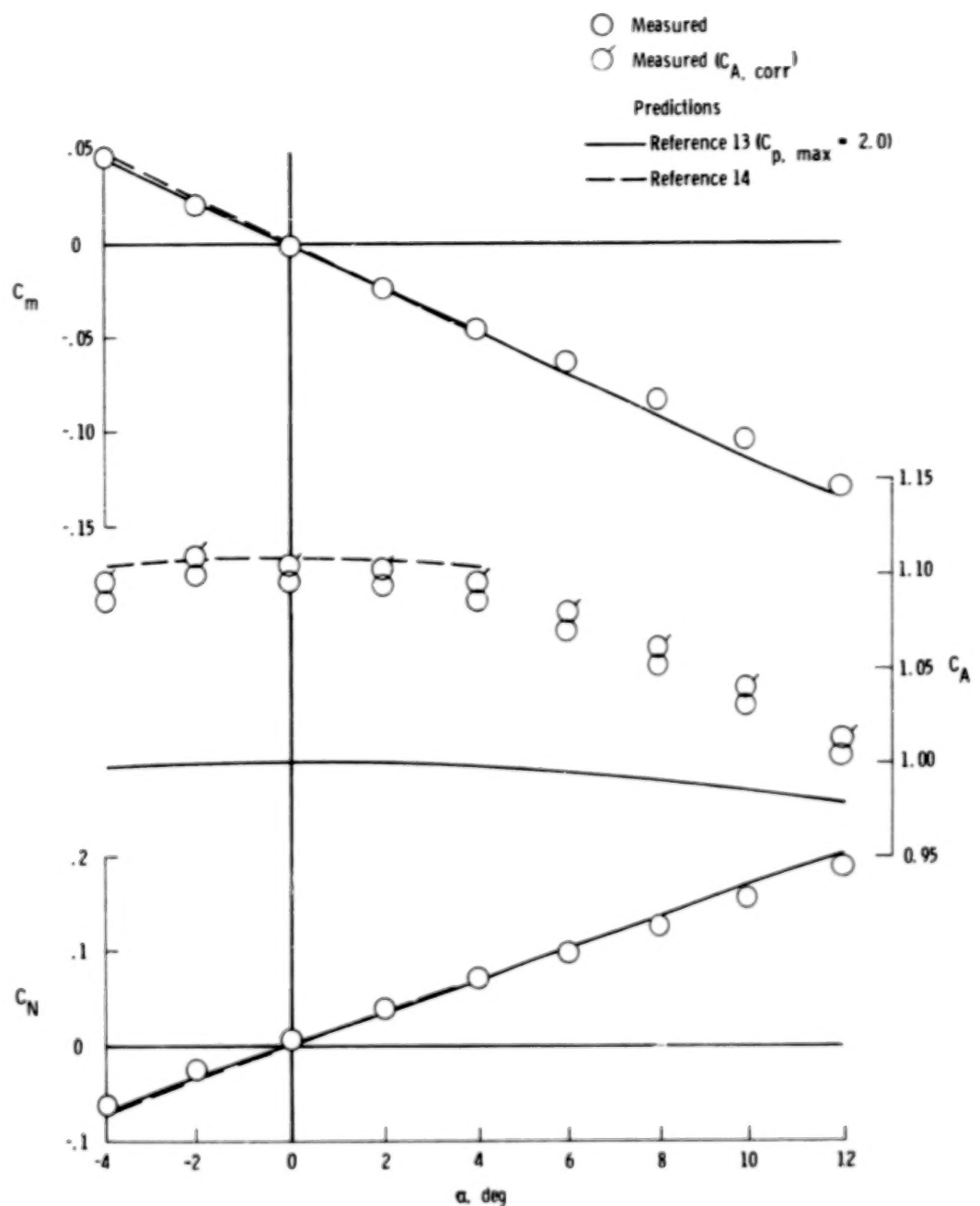
(h)  $\theta = 70^\circ$ ;  $r_n/r_b = 0.50$ .

Figure 12.- Concluded.



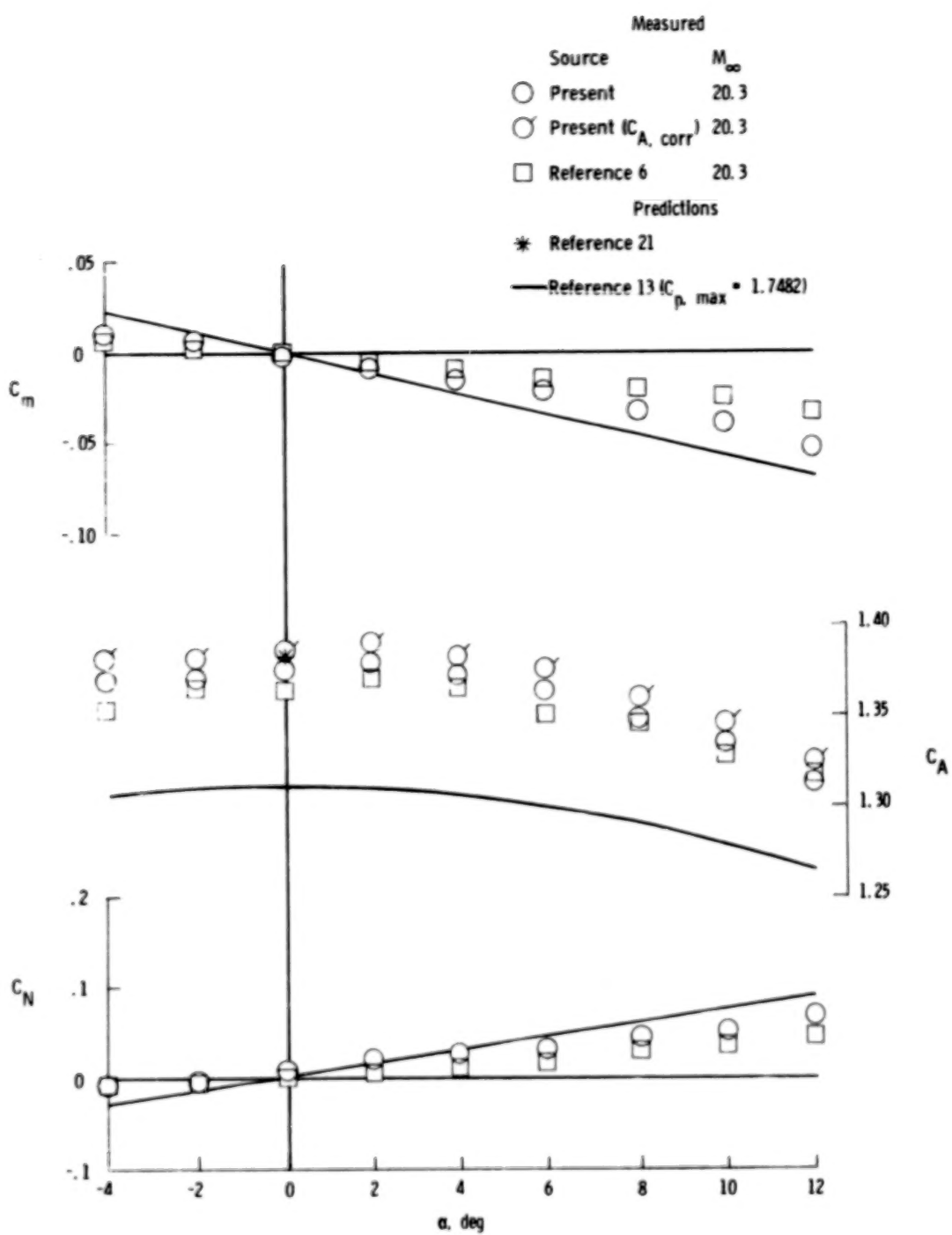
(a)  $\theta = 30^\circ$ .

Figure 13.- Measured and predicted static aerodynamic coefficients for sharp cones.



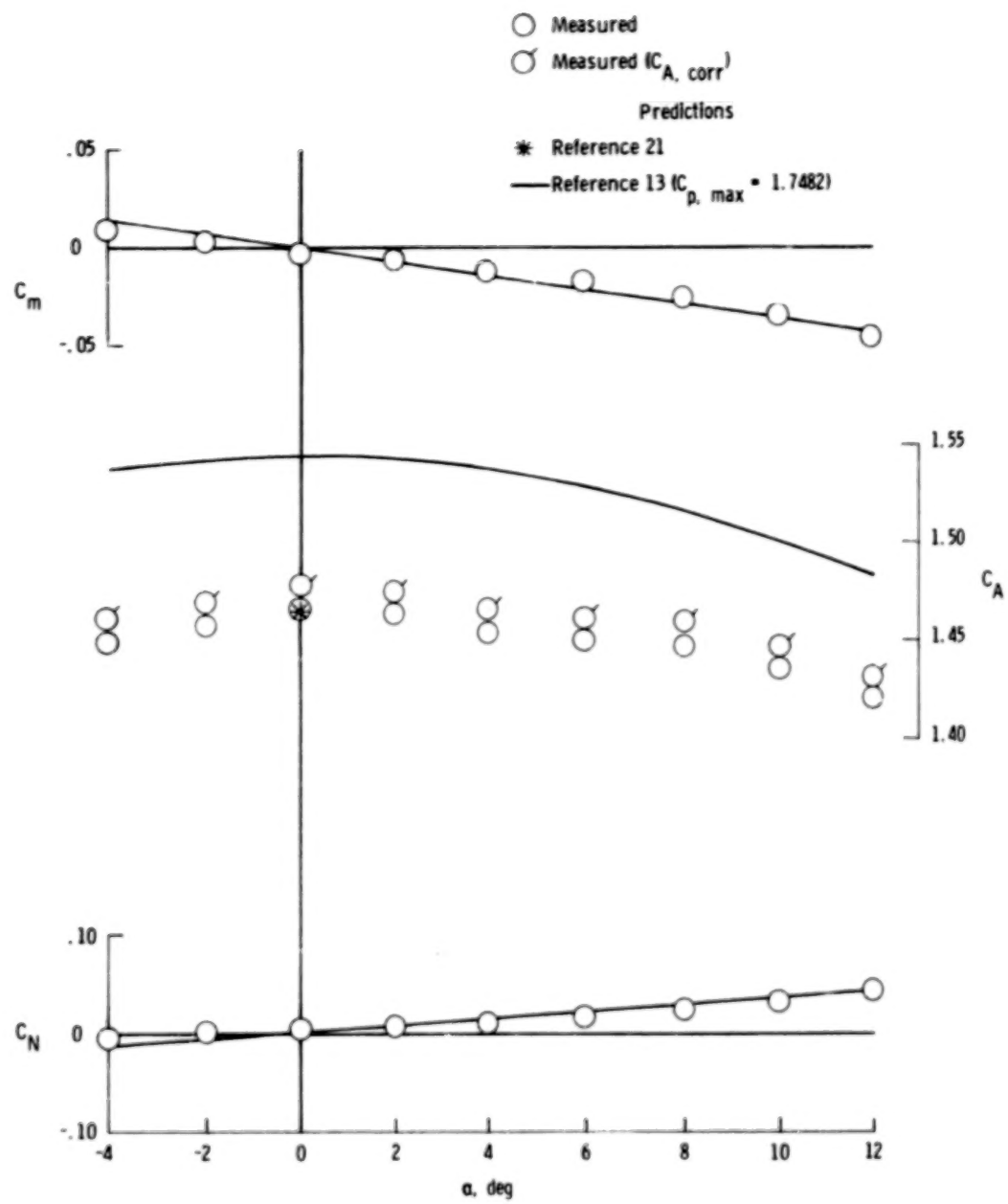
(b)  $\theta = 45^\circ$ .

Figure 13.- Continued.



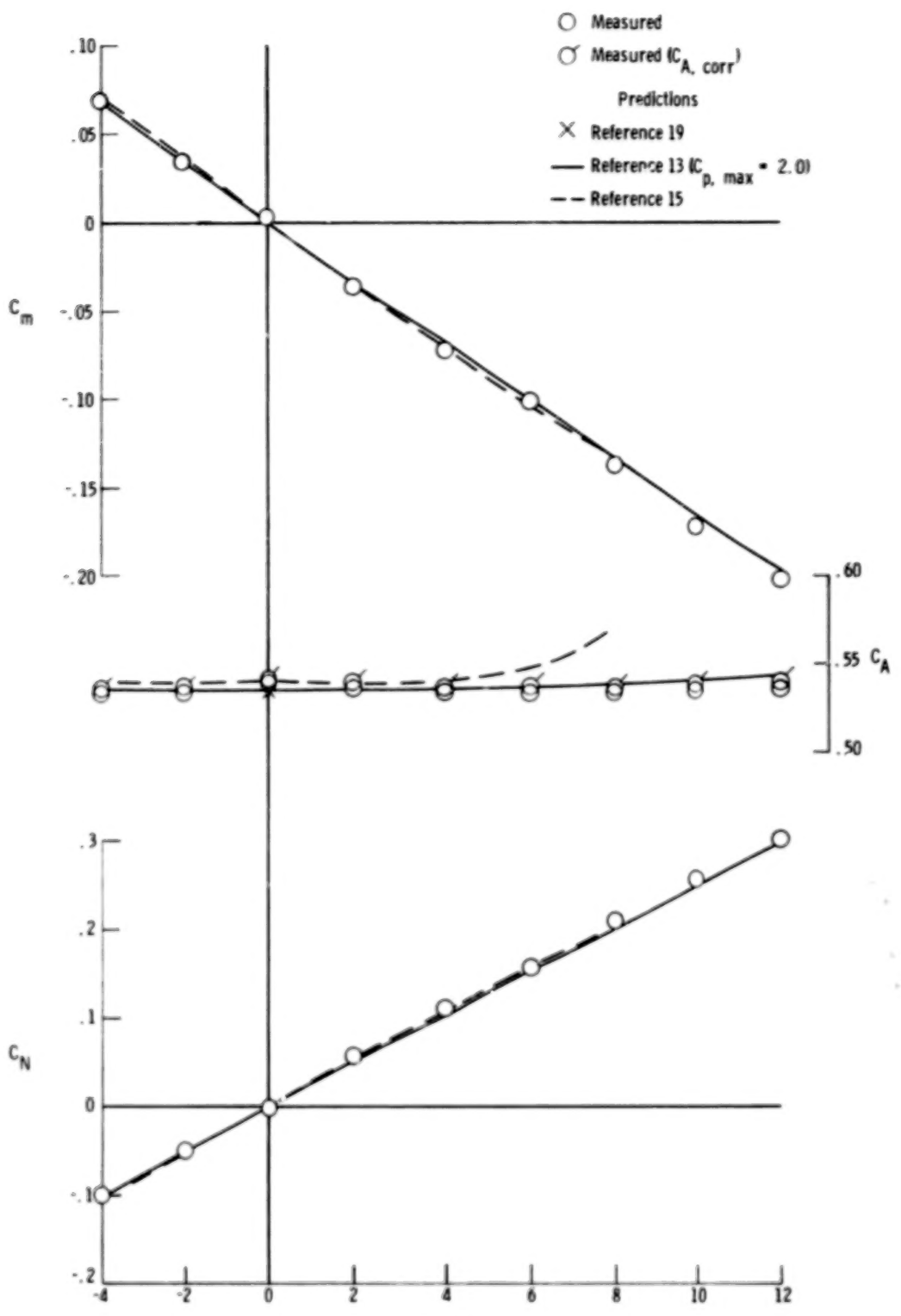
(c)  $\theta = 60^\circ$ .

Figure 13.- Continued.



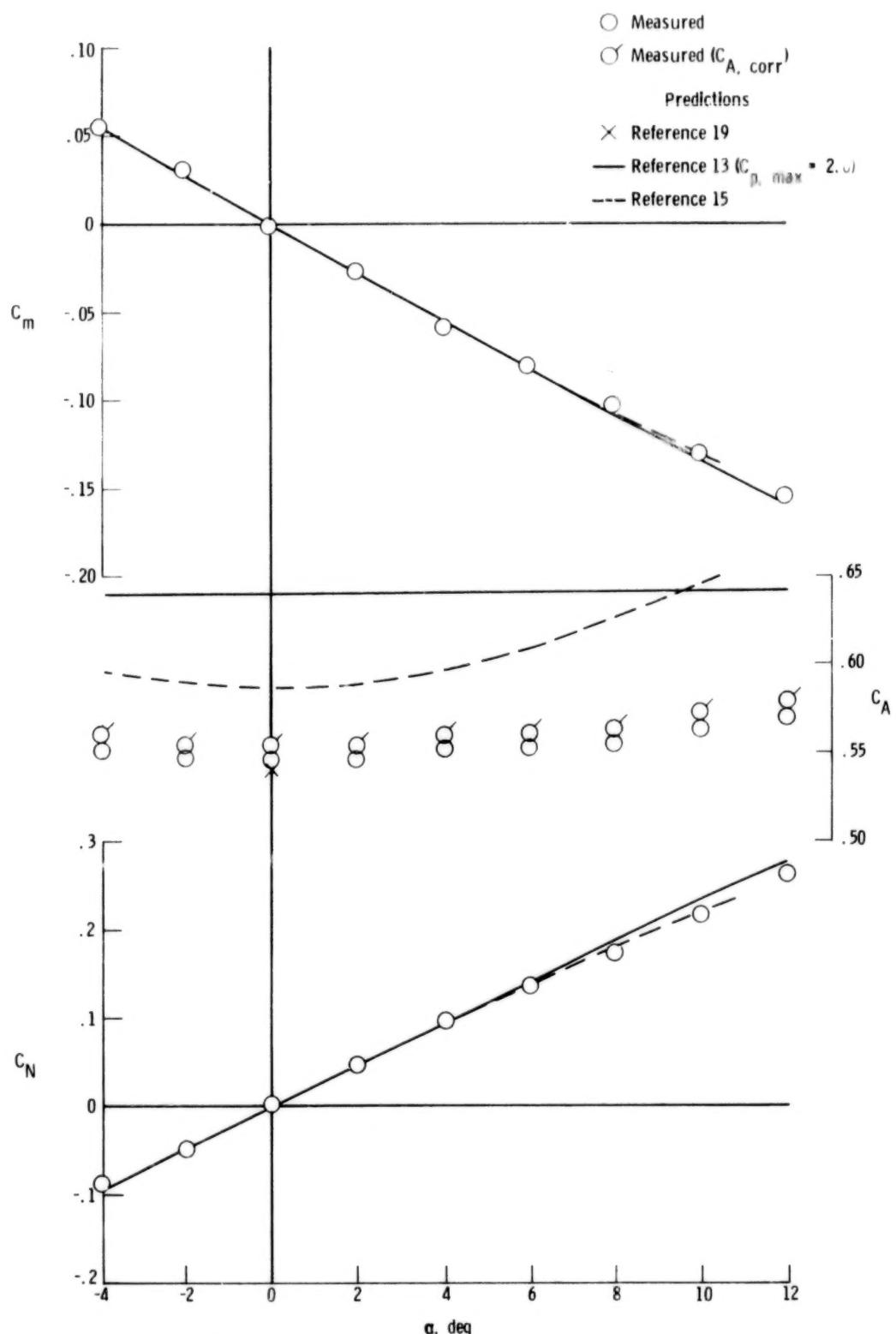
(d)  $\theta = 70^\circ$ .

Figure 13.- Concluded.



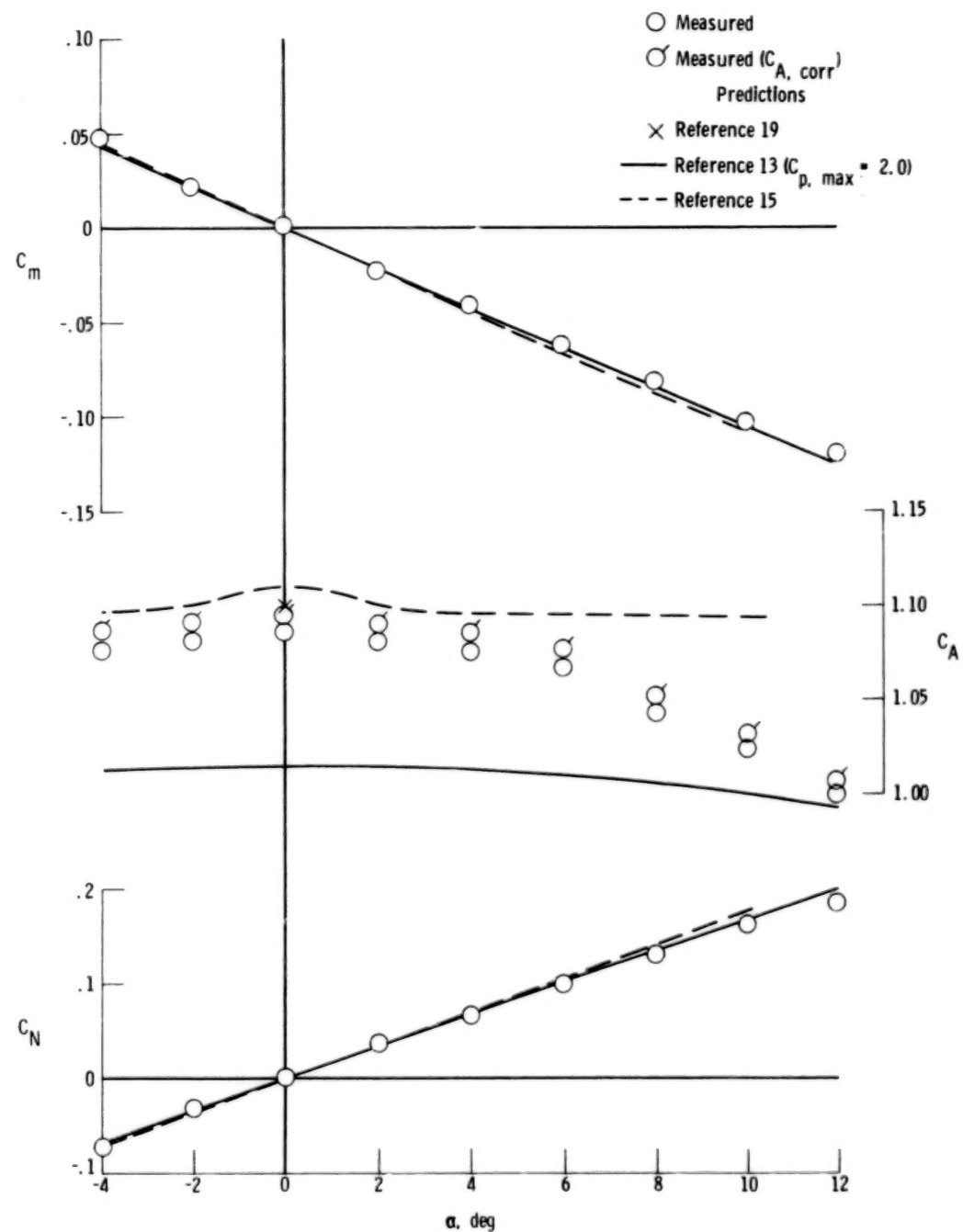
(a)  $\theta = 30^\circ$ ;  $r_n/r_b = 0.25$ .

Figure 14.- Measured and predicted static aerodynamic coefficients for spherically blunted cones.



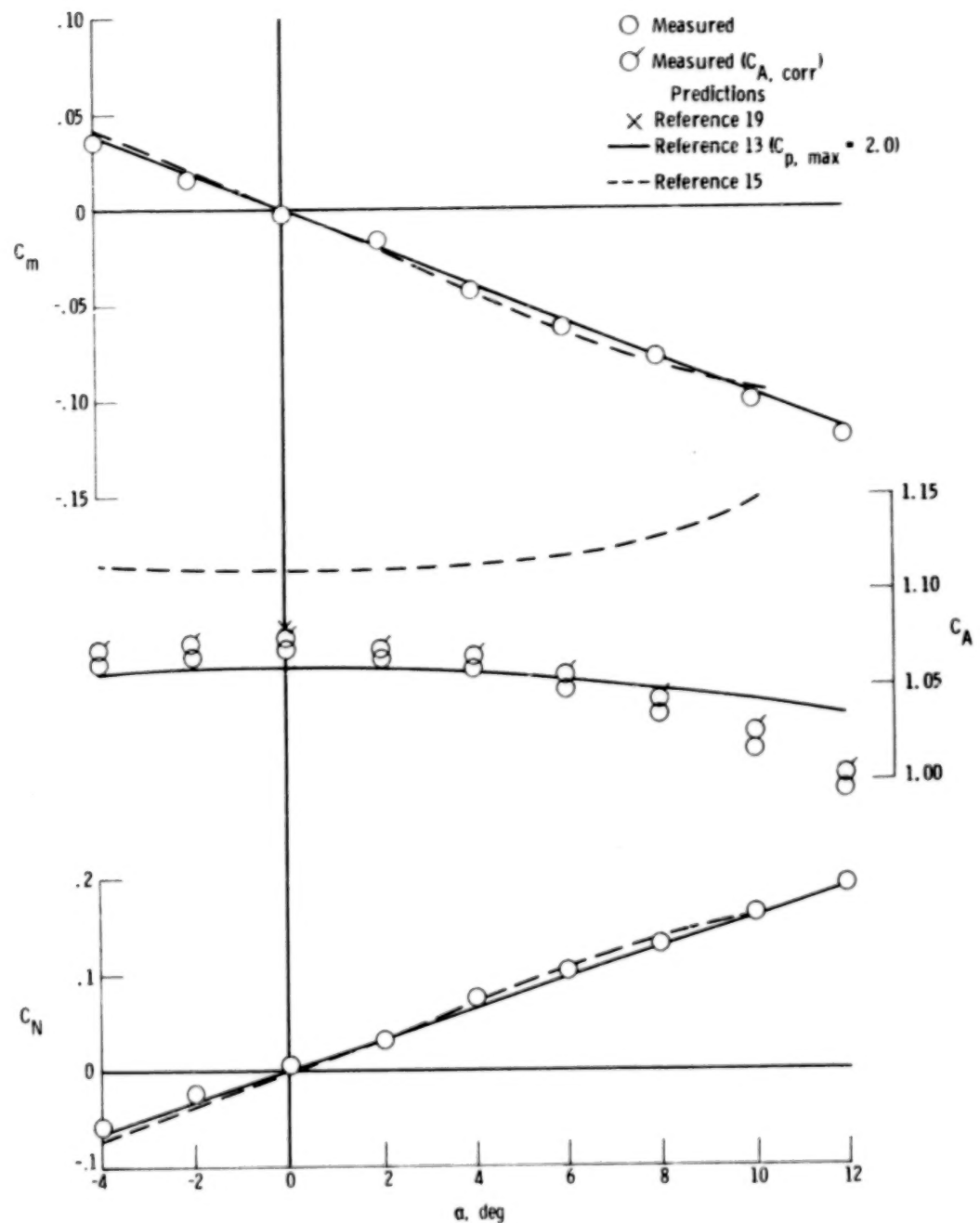
(b)  $\theta = 30^\circ$ ;  $r_n/r_b = 0.50$ .

Figure 14.- Continued.



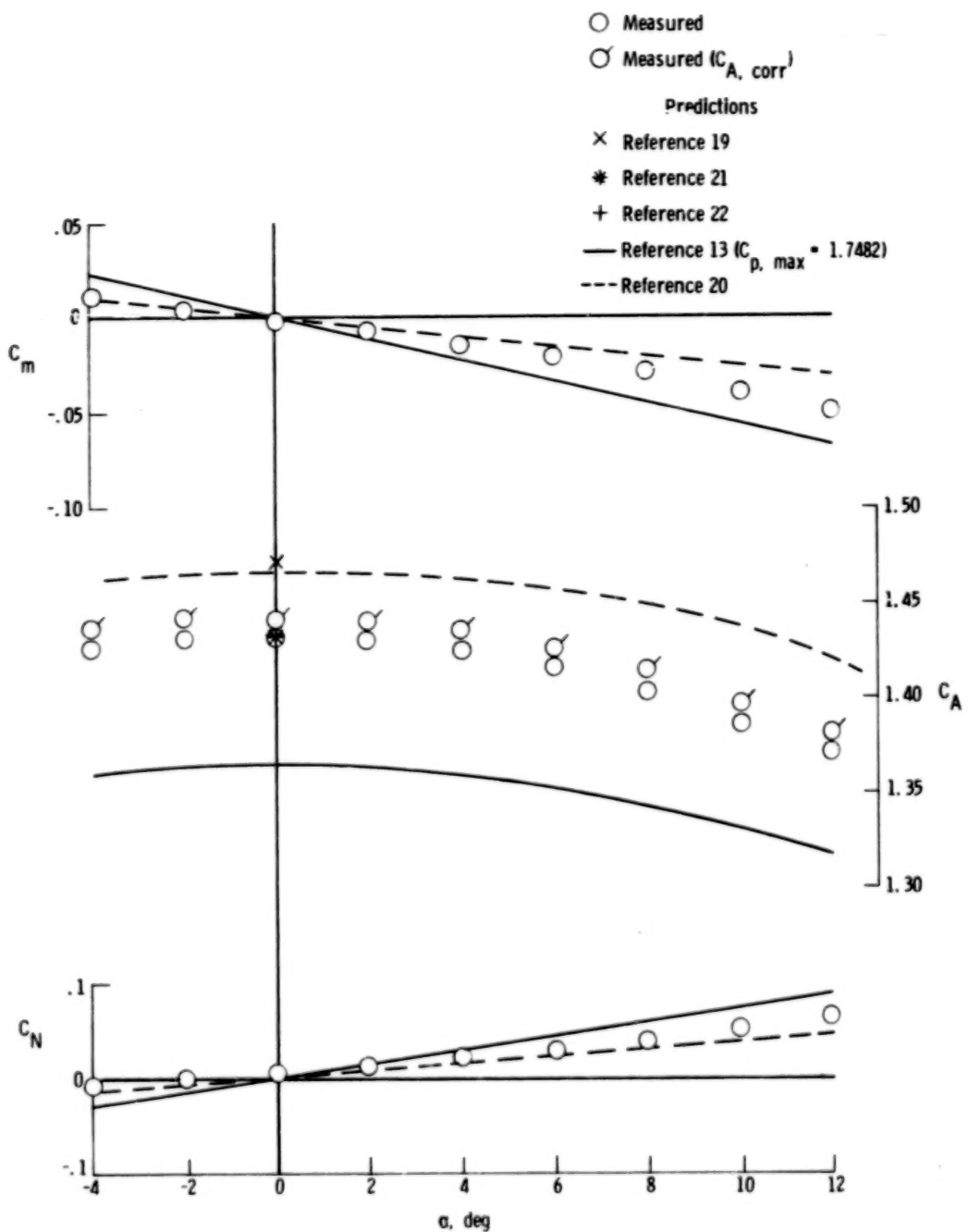
(c)  $\theta = 45^\circ$ ;  $r_n/r_b = 0.25$ .

Figure 14.- Continued.



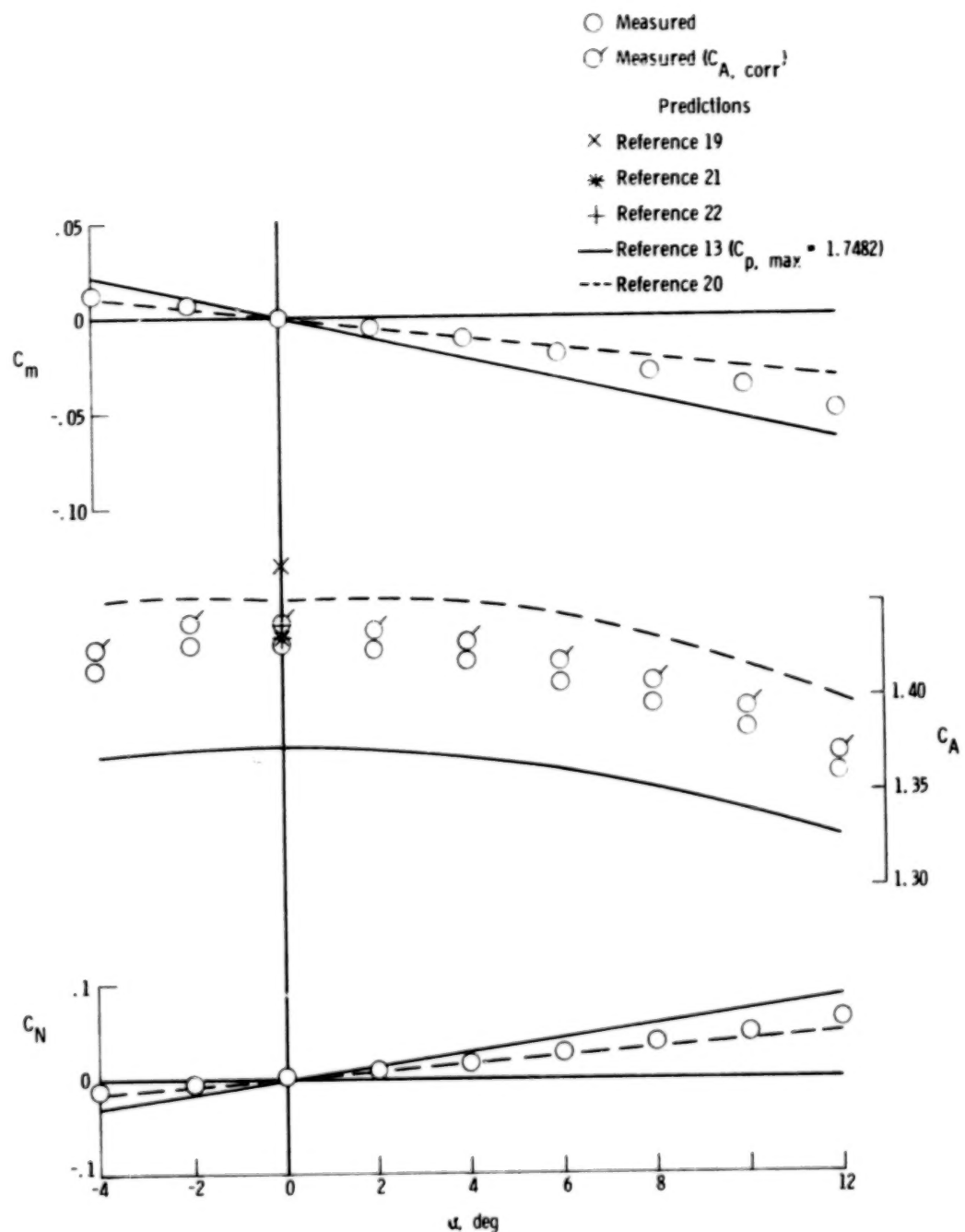
(d)  $\theta = 45^\circ$ ;  $r_n/r_b = 0.50$ .

Figure 14.- Continued.



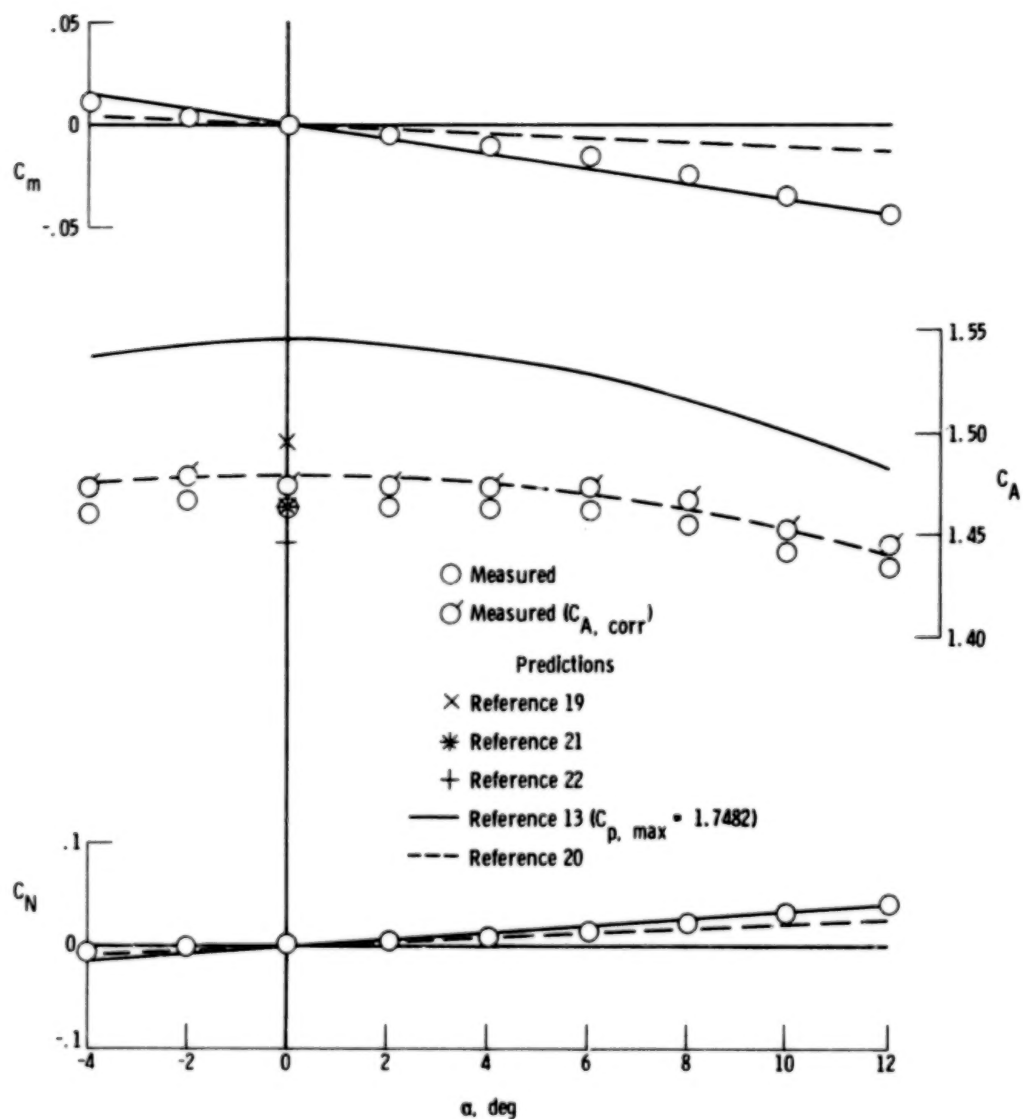
(e)  $\theta = 60^\circ$ ;  $r_n/r_b = 0.25$ .

Figure 14.- Continued.



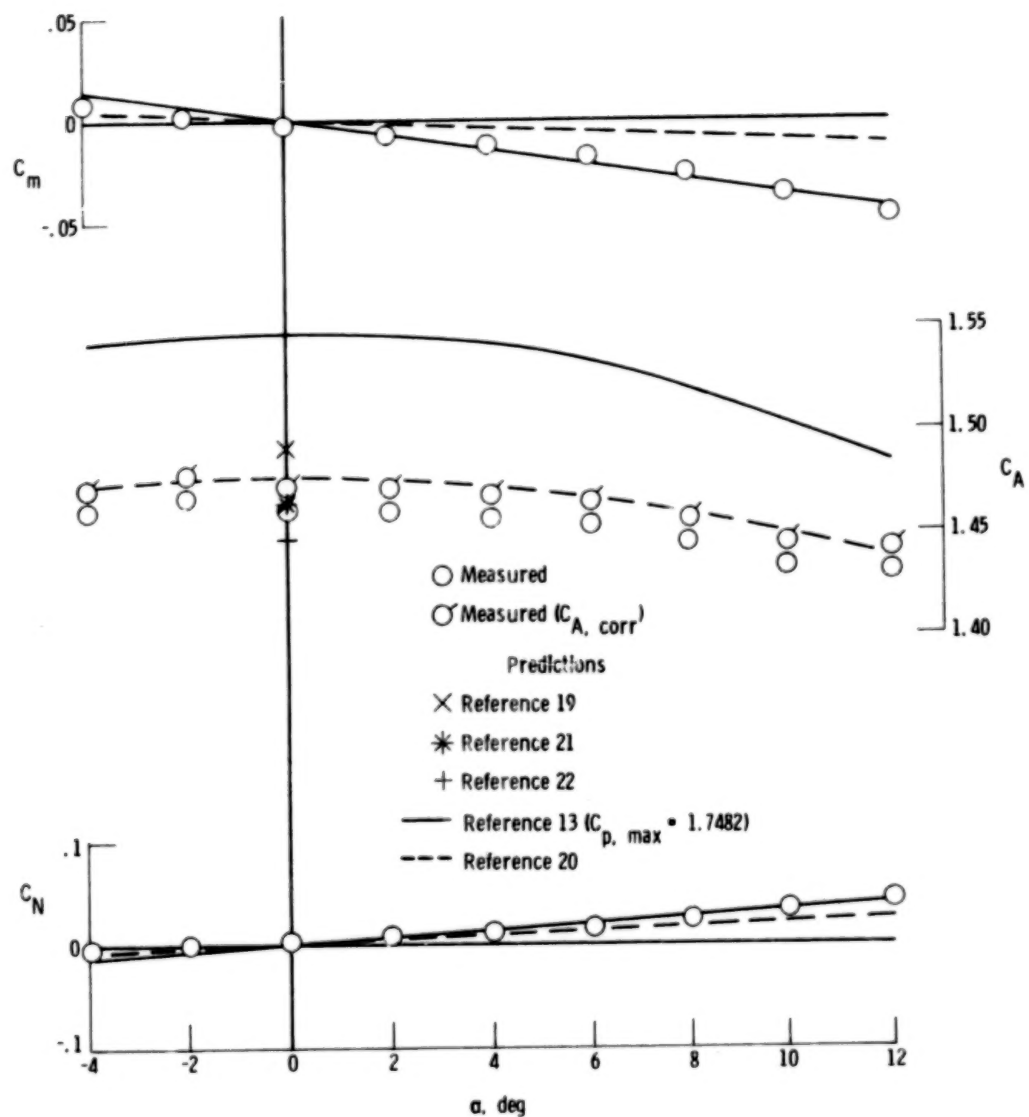
(f)  $\theta = 60^\circ; r_n/r_b = 0.50.$

Figure 14.- Continued.



(g)  $\theta = 70^\circ$ ;  $r_n/r_b = 0.25$ .

Figure 14.- Continued.



(h)  $\theta = 70^\circ$ ;  $r_n/r_b = 0.50$ .

Figure 14.- Concluded.

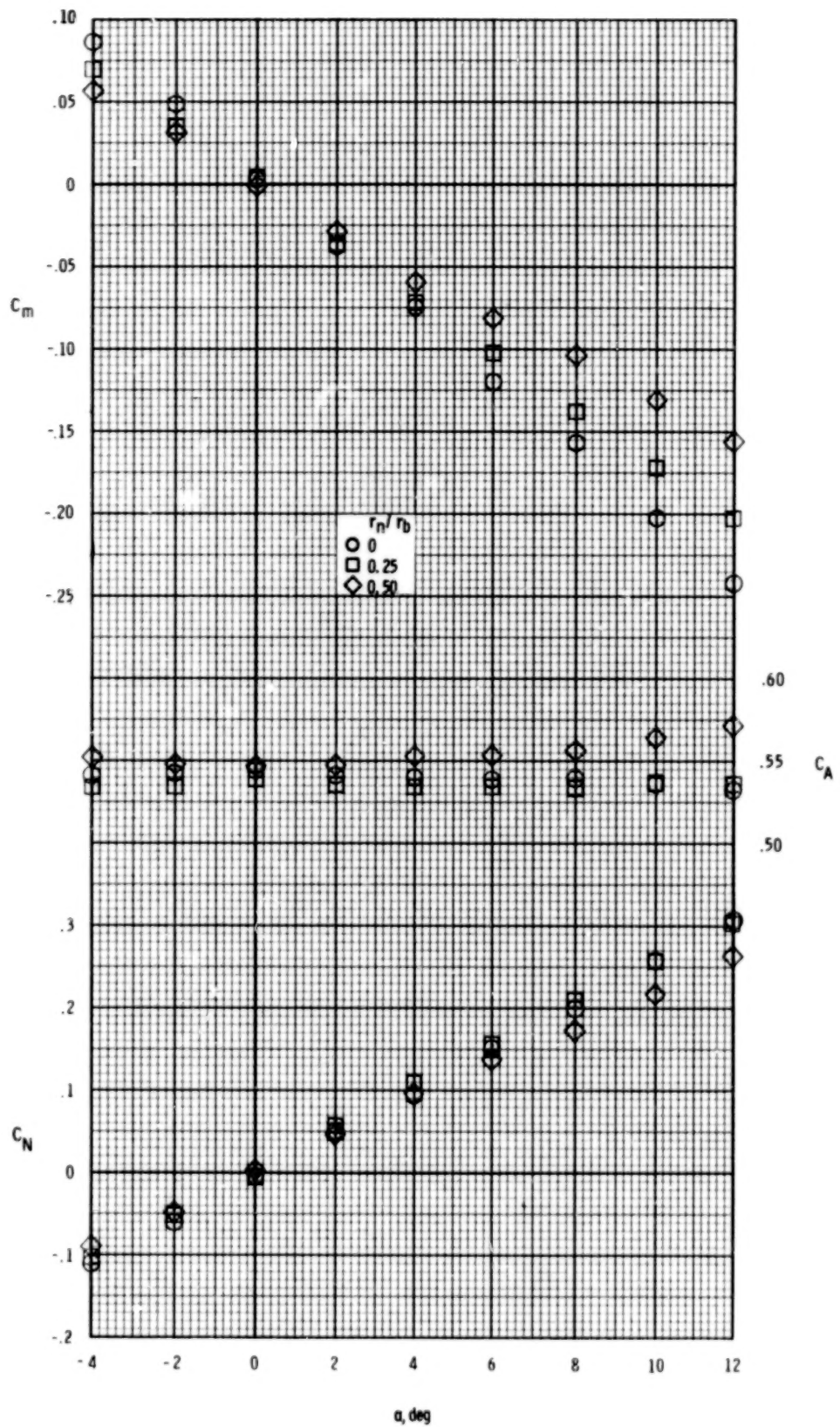


Figure 15.- Effect of nose bluntness on static aerodynamic coefficients of a  $30^\circ$  cone.

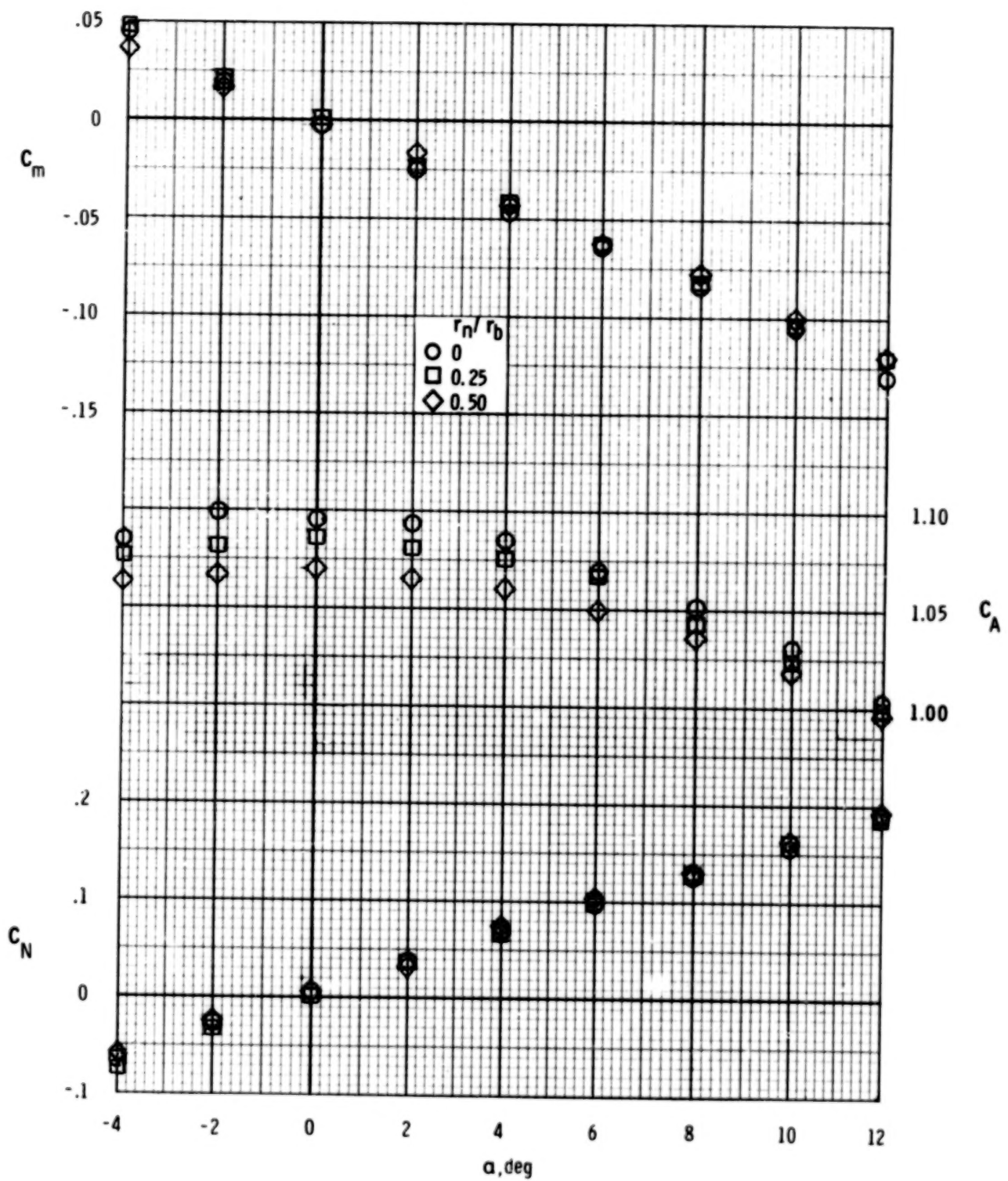


Figure 16.- Effect of nose bluntness on static aerodynamic coefficients of a  $45^\circ$  cone.

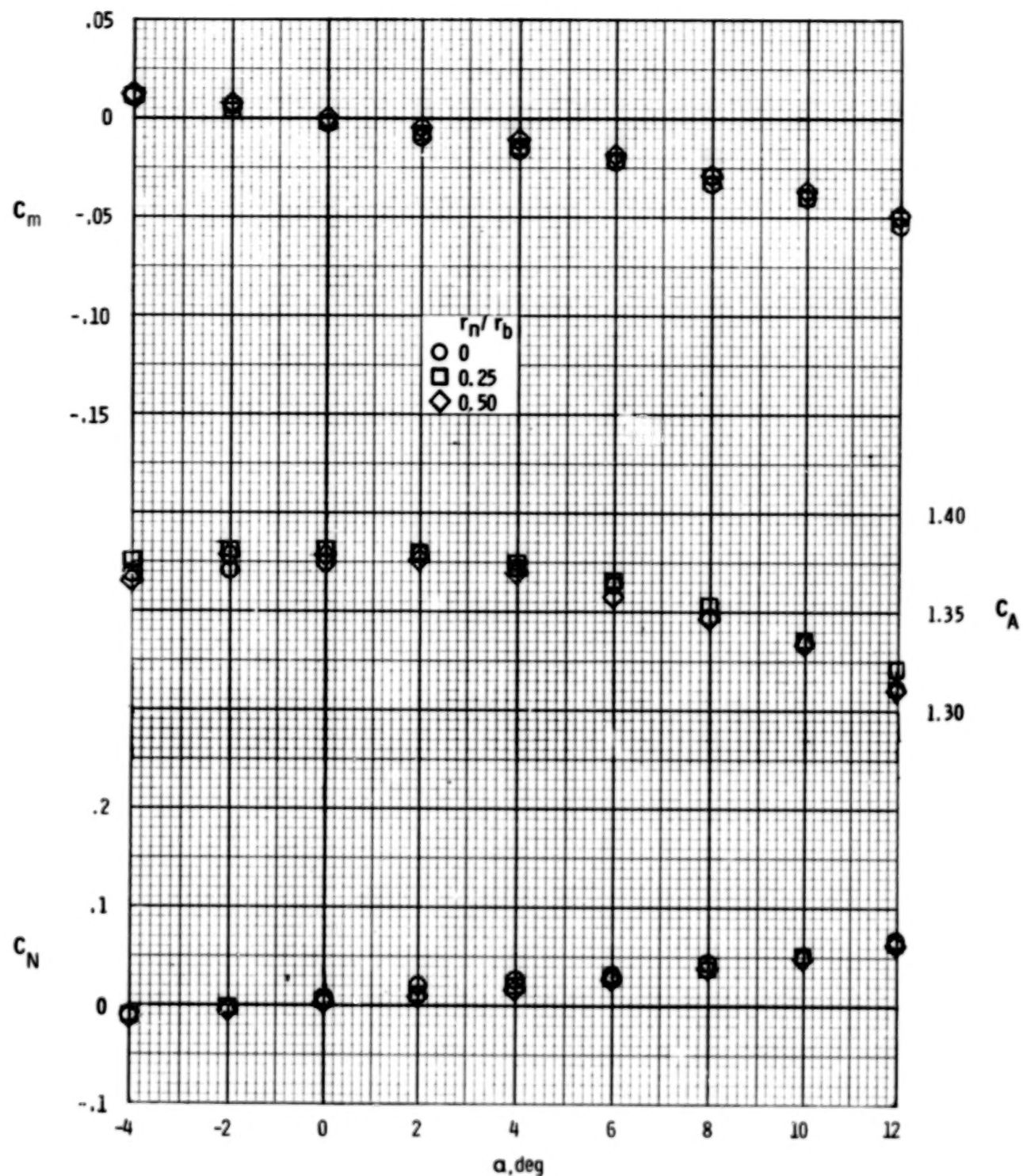


Figure 17.- Effect of nose bluntness on static aerodynamic coefficients of a  $60^\circ$  cone.

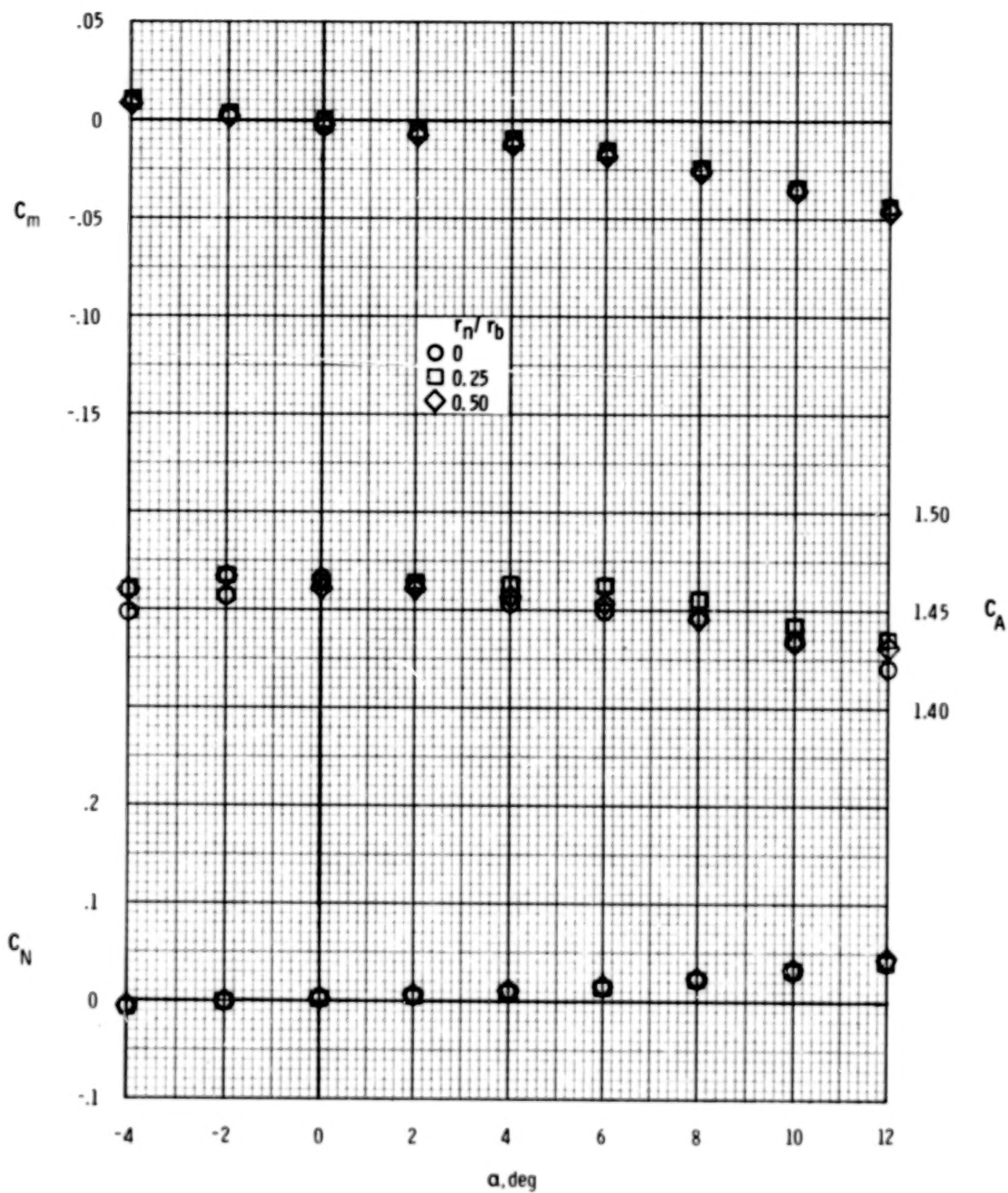


Figure 18.- Effect of nose bluntness on static aerodynamic coefficients of a  $70^\circ$  cone.

1. Report No. NASA TP-1395	2. Government Accession No.	3. Recipient's Catalog No.	
4. Title and Subtitle MEASURED AND PREDICTED SHOCK SHAPES AND AERODYNAMIC COEFFICIENTS FOR BLUNTED CONES AT INCIDENCE IN HELIUM AT MACH 20.3		5. Report Date March 1979	
7. Author(s) Robert L. Calloway and Nancy H. White		6. Performing Organization Code	
9. Performing Organization Name and Address NASA Langley Research Center Hampton, VA 23665		8. Performing Organization Report No. L-12058	
12. Sponsoring Agency Name and Address National Aeronautics and Space Administration Washington, DC 20546		10. Work Unit No. 506-26-13-02	
15. Supplementary Notes		11. Contract or Grant No.	
16. Abstract  Experimental values of shock shapes ( $\alpha = 0^\circ$ and $10^\circ$ ) and static aerodynamic coefficients ( $\alpha = -4^\circ$ to $12^\circ$ ) for sharp and spherically blunted cones having cone half-angles of $30^\circ$ , $45^\circ$ , $60^\circ$ , and $70^\circ$ and nose bluntness ratios of 0, 0.25, and 0.50 are presented. Shock shapes were also measured at $0^\circ$ angle of attack by using a flat-faced cylinder ( $90^\circ$ cone) and a hemispherically blunted cylinder (sphere). All tests were conducted in helium ( $\gamma = 5/3$ ) at a free-stream Mach number of 20.3 and a unit free-stream Reynolds number of $22.4 \times 10^6$ per meter. Comparisons between measured values and predicted values were made by using several numerical and simple engineering methods.		13. Type of Report and Period Covered Technical Paper	
17. Key Words (Suggested by Author(s)) Cones Helium Hypersonic Shock shapes		14. Sponsoring Agency Code	
18. Distribution Statement Unclassified - Unlimited		Subject Category 34	
19. Security Classif. (of this report) Unclassified	20. Security Classif. (of this page) Unclassified	21. No. of Pages 71	22. Price* \$5.25

\* For sale by the National Technical Information Service, Springfield, Virginia 22161

NASA-Langley, 1979

90

**I C A N D**

**APR 30 1979**